

UNIVERSITÉ DU QUÉBEC À MONTRÉAL

LES ISOTOPES DES FAMILLES U & Th :
UN REGARD SUR LA DYNAMIQUE SÉDIMENTAIRE DE LA BAIE DE
BAFFIN ET DU NORD-OUEST DE LA MER DU LABRADOR
AU COURS DU DERNIER CYCLE GLACIAIRE

THÈSE
PRÉSENTÉE
COMME EXIGENCE PARTIELLE
DU DOCTORAT EN SCIENCES DE LA TERRE ET DE L'ATMOSPHÈRE

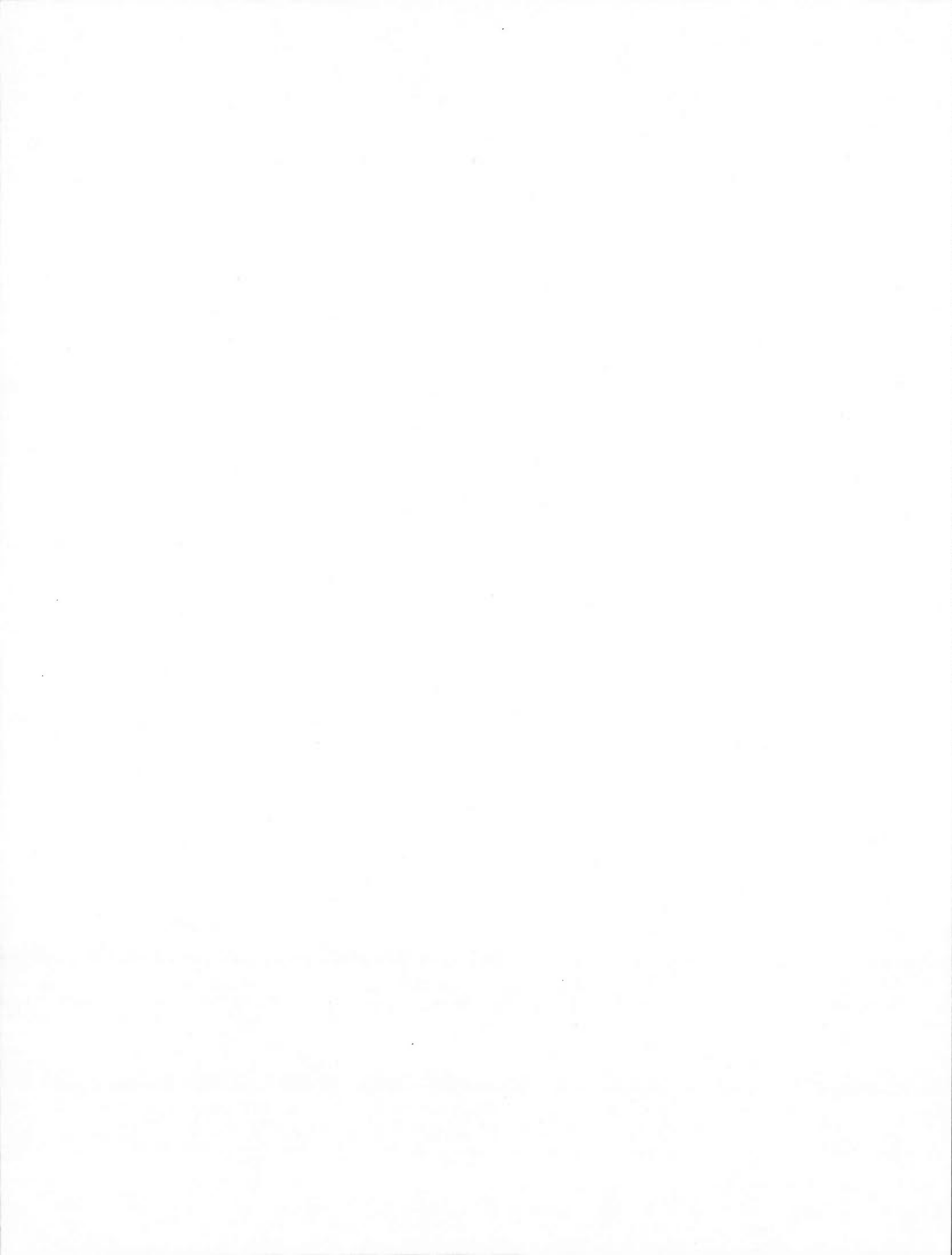
PAR
LAURENCE NUTTIN

MAI 2014

UNIVERSITÉ DU QUÉBEC À MONTRÉAL
Service des bibliothèques

Avertissement

La diffusion de cette thèse se fait dans le respect des droits de son auteur, qui a signé le formulaire *Autorisation de reproduire et de diffuser un travail de recherche de cycles supérieurs* (SDU-522 – Rév.01-2006). Cette autorisation stipule que «conformément à l'article 11 du Règlement no 8 des études de cycles supérieurs, [l'auteur] concède à l'Université du Québec à Montréal une licence non exclusive d'utilisation et de publication de la totalité ou d'une partie importante de [son] travail de recherche pour des fins pédagogiques et non commerciales. Plus précisément, [l'auteur] autorise l'Université du Québec à Montréal à reproduire, diffuser, prêter, distribuer ou vendre des copies de [son] travail de recherche à des fins non commerciales sur quelque support que ce soit, y compris l'Internet. Cette licence et cette autorisation n'entraînent pas une renonciation de [la] part [de l'auteur] à [ses] droits moraux ni à [ses] droits de propriété intellectuelle. Sauf entente contraire, [l'auteur] conserve la liberté de diffuser et de commercialiser ou non ce travail dont [il] possède un exemplaire.»



AVANT-PROPOS

La thèse présentée dans ce document est intitulée « *Les isotopes des familles U & Th: un regard sur la dynamique sédimentaire de la baie de Baffin et du nord-ouest de la mer du Labrador au cours du dernier cycle glaciaire* ». Elle a été rédigée sous la forme de deux chapitres majeurs, en langue anglaise, chacun correspondant à un article à soumettre dans une revue scientifique pour publication. Les chapitres sont encadrés par une introduction et une conclusion générale, en accord avec les directives de l'Université du Québec à Montréal. Le choix du sujet est directement issu d'un des thèmes d'étude du centre de recherche du GEOTOP sur les variabilités passées de l'océan et du climat.

Les deux chapitres traitent des résultats de l'analyse de sédiments marins profonds provenant de deux zones spécifiques : la mer du Labrador et la baie de Baffin, deux bassins océaniques de l'Atlantique du Nord-Ouest. Les deux projets se concentrent plus spécifiquement sur les isotopes de l'uranium (U), du thorium (Th) et du protactinium (Pa), et intègrent ceux-ci dans une approche multi-paramètres, i.e. alliant les données isotopiques recueillies à d'autres propriétés sédimentologiques (physiques, minéralogiques, géochimiques). L'entièreté des manipulations et des mesures analytiques présentées dans ce document (à l'exception des mesures d'âges radiocarbone) ont été réalisées dans les différents laboratoires du GEOTOP, et sous l'encadrement des chercheurs qui en sont responsables. L'analyse statistique de l'ensemble des données, la composition des figures, l'interprétation des résultats et la rédaction des articles furent réalisées sous la supervision et les conseils du Professeur Claude Hillaire-Marcel, directeur de cette thèse de doctorat.

Le premier chapitre correspond à un article qui a été soumis dans la revue *Marine Geology*, ayant pour titre “*U- and Th-series isotopes in deep Baffin Bay*

sediments: tracers of detrital sources and of contrasted glacial/interglacial sedimentary processes", avec Claude Hillaire-Marcel comme co-auteur. Cet article traite de la distribution des isotopes de l'U et du Th dans une séquence sédimentaire provenant de la plaine abyssale centrale de la baie de Baffin et s'étalant temporellement sur les derniers ~115 ka (i.e., le dernier cycle glaciaire), afin de retracer les processus et flux géochimiques et sédimentaires de la zone étudiée. Les inventaires de ^{230}Th en excès permettent d'étudier la dynamique particulière en relation avec la dynamique des calottes de glace de la région, la circulation océanique dans la baie et les conditions climatiques associées.

Le deuxième chapitre, intitulé "*U, Th and Pa insights into sedimentological and paleoceanographic changes off Hudson Strait (Labrador Sea) during the last ~37 ka with special attention to methodological issues*", correspond à un article qui a été soumis dans la revue *Quaternary Science Reviews* et inclut Jenny Maccali et Claude Hillaire-Marcel comme co-auteurs. Le sujet concerne l'étude d'une séquence sédimentaire provenant d'un site localisé à proximité de l'embouchure du détroit d'Hudson et enregistrant deux événements de Heinrich récents (H2 et H1). La dynamique particulière depuis le glaciaire tardif (i.e., les ~37 derniers ka) est essentiellement évaluée à travers l'étude des variations du ^{230}Th et du ^{231}Pa en excès enregistrées dans la colonne sédimentaire. Elle est mise en relation avec les épisodes de fonte de la calotte glaciaire des Laurentides, la circulation méridienne de renversement de l'océan Atlantique et les variations abruptes du climat associées. Une attention particulière est portée aux processus et flux géochimiques et sédimentaires, pour notamment en déduire les incertitudes potentielles sur l'estimation de ces traceurs.

Enfin, un article intitulé "*Authigenic, detrital and diagenetic minerals in the Laguna Potrok Aike sediment sequence*" a également été réalisé pendant la durée du doctorat (voir Annexe A). Celui-ci a été publié dans la revue *Quaternary Science Reviews* en

2013, avec comme co-auteurs Pierre Francus, Michel Preda, Bassam Ghaleb et Claude Hillaire-Marcel. Bien que sa rédaction ait permis d'acquérir les bases géochimiques fondamentales à la bonne complétion de cette thèse, il n'est pas repris comme chapitre à part entière pour assurer l'homogénéité du document final.

REMERCIEMENTS

A l'issue de ces années de recherche, je tiens tout d'abord à remercier mon directeur de thèse, Claude Hillaire-Marcel. Je le remercie de m'avoir accordé sa confiance, d'avoir partagé son expérience de par ses différentes interventions, de son soutien et de m'avoir offert l'opportunité d'être son auxiliaire d'enseignement à deux reprises dans son cours de géochimie isotopique.

Cette thèse n'aurait jamais pu être réalisée sans l'aide de Bassam Ghaleb, chercheur au GEOTOP en géochimie isotopique, et éminent spécialiste des isotopes radioactifs. Je le remercie chaleureusement pour m'avoir patiemment enseigné tout ce qu'il fallait savoir sur les analyses chimiques nécessaires à l'isolement de l'uranium et du thorium, et sur l'utilisation des instruments de mesure. Merci pour ta patience, tes échanges stimulants, ton aide en tout temps, ta gentillesse, tes conseils, ton soutien, ton écoute, et ton amitié.

Je voudrais également remercier l'ensemble de l'équipe PASADO pour les recherches que j'ai réalisées avec eux sur le lac Potrok Aike. Je remercie en particulier et chaleureusement mon co-directeur sur ce projet, Pierre Francus, pour son soutien et son encadrement scientifique. Bien que ce projet ne fasse plus partie intégrante de ma thèse, il restera le sujet de mon tout premier article scientifique publié.

Je remercie tous les étudiants et le personnel du GEOTOP que j'ai côtoyés pendant toutes ces années au centre de recherche. Je remercie Elisabeth Lindsay, Nicole Turcot et Josée Savard pour leur aide précieuse dans les tâches administratives, ainsi que Sandrine Solignac, André Poirier, Jean-François Hélie, Julien Gogot, Agnieszka Adamowicz, Maryse Henri et Michel Preda pour leur aide dans les analyses de laboratoire et leur disponibilité pour développer et valider mes connaissances

scientifiques. Merci également à Christelle Not et François De Vleeschouwer pour leurs conseils et relectures.

Je tiens à consacrer quelques modestes lignes de cette section pour d'énormes remerciements à Jenny Maccali, véritable mentor dans la dernière ligne droite. Merci mille fois pour ton gros coup de main dans les périlleuses analyses de protactinium. Merci d'avoir supporté mon stress, le planning ambitieux que je t'ai imposé l'été dernier, merci de m'avoir guidée, soutenue, écoutée et parfois réconfortée aussi. Merci à Olivia Gibb pour sa joie de vivre et à Jean-Baptiste Plouhinec pour ses longues soirées à disserter sur la science. Merci à Quentin Simon pour son humour (ou pas...), son écoute, ses discussions scientifiques, sa visite du CEREGE. J'aurai mis le temps à réaliser ton départ mais ta présence m'aura bien manqué dans les derniers mois. Merci à Nicolas Van Nieuwenhove pour son expérience et à Audrey Limoges, avec qui j'ai pu notamment partager l'expérience d'organiser les congrès étudiants du GEOTOP, et la conférence Goldschmidt de juillet 2012. Enfin, merci à tous pour votre amitié.

Merci à Nathalie Fagel, ma directrice de maîtrise, pour m'avoir introduite dans la recherche en paléo et sur le projet PASADO qui m'a fait entrer au GEOTOP.

Merci à Méli et ses parents pour m'avoir si chaleureusement accueillie au Québec.

Puis, une petite note pour mes amis belges rencontrés à Montréal. Sans vous, les années passées ici n'auraient pas été aussi géniales. Les expériences vécues ensemble icitte là nous souderont pour longtemps encore. Merci à Céline & Renaud (the first team; merci Céline pour tous tes conseils de lointaine collègue Ph.D.), à Cécile, Raph, Cath & Loïc, les disparus Isa & Fx, Sandra, l'assimilée, Thylla & Gauthier.

Merci à mes amis en Belgique (avec un spécial à Pauline) pour leur soutien, la décompression à chacun de mes retours, leurs petites attentions, leurs vacances passées chez nous, et pour leur fidélité!

Je remercie chaleureusement tous les membres de ma famille. Merci d'avoir supporté mon absence, de m'avoir changé les idées en me rendant visite et de m'avoir conseillée lorsque j'en avais besoin.

Et finalement « *last but not least* », je remercie Dimitri... en commençant par sa famille, qui l'a laissé partir avec moi. En soulignant également son adaptation exemplaire aux conditions climatiques impitoyables du Québec. Merci Dimitri, fort que tu es même si tu l'es un peu moins, de m'avoir accompagnée (endurée?) pendant ces années à Montréal, de m'avoir soutenue de manière inconditionnelle, écoutée, consolée, encouragée, et d'avoir partagé cette fantastique expérience avec moi. Merci d'avoir tenu le coup aussi bien durant les longs hivers *de tempêtes de neige et pluies verglaçantes*, que durant les étés ensoleillés *de chaleur accablante* (je sais à quel point les nimbostratus de notre beau ciel belge t'ont manqué, merci d'avoir tenu le coup!). Enfin, merci d'avoir fait une croix sur nos merveilleuses frites belges et le reste!

Finalement, la thèse c'est comme une boîte de chocolats, on ne sait jamais sur quoi on va tomber...

TABLE DES MATIÈRES

AVANT-PROPOS	iii
REMERCIEMENTS	vi
TABLE DES MATIÈRES	ix
LISTE DES FIGURES.....	xiii
LISTE DES TABLEAUX.....	xvi
RÉSUMÉ	xvi
INTRODUCTION	1
0.1 PROBLÉMATIQUE.....	1
0.2 OBJECTIFS.....	2
0.3 RÉGION D'ÉTUDE	3
0.4 MATÉRIEL	5
0.5 APPROCHE MÉTHODOLOGIQUE.....	7
0.6 CONTENU DU MANUSCRIT	12
CHAPITRE I U- AND Th-SERIES ISOTOPES IN DEEP BAFFIN BAY SEDIMENTS: TRACERS OF DETRITAL SOURCES AND OF CONTRASTED GLACIAL/INTERGLACIAL SEDIMENTARY PROCESSES	19
ABSTRACT.....	20
1.1 INTRODUCTION.....	21
1.2 REGIONAL SETTINGS.....	24
1.3 MATERIALS AND METHODS	26
1.4 RESULTS	29
1.4.1 Sedimentological features	29
1.4.2 U and Th isotopic data	30
1.5 DISCUSSION	31
1.5.1 Uranium flux and sedimentary processes	31
1.5.2 Oxygenation conditions	33

1.5.3 Terrigenous supply.....	34
1.5.4 $^{230}\text{Th}_{\text{xs}}$ flux and evolution in deep-water circulation.....	35
1.6 CONCLUSION.....	38
ACKNOWLEDGMENTS.....	39
SUPPLEMENTARY INFORMATION	40
REFERENCES	43
FIGURES	50
 CHAPITRE II	
U, Th AND PA INSIGHTS INTO SEDIMENTOLOGICAL AND PALEOCEANOGRAPHIC CHANGES OFF HUDSON STRAIT (LABRADOR SEA) DURING THE LAST ~37 KA WITH SPECIAL ATTENTION TO METHODOLOGICAL ISSUES.....	
ABSTRACT.....	59
2.1 INTRODUCTION.....	60
2.2 MATERIALS AND METHODS	62
2.2.1. Sedimentological parameters	62
2.2.2. Radionuclide analyses.....	64
2.3 RESULTS	67
2.3.1 Sedimentological features	67
2.3.2 Radionuclide data.....	71
2.4 DISCUSSION	72
2.4.1 Late vs early diagenetic evolution of U-contents and activity ratios	72
2.4.2 Terrigenous detrital supply	75
2.4.3 Constraints from $(^{230}\text{Th}_{\text{xs}})_0$ and $(^{231}\text{Pa}_{\text{xs}})_0$	75
2.4.4 $(^{230}\text{Th}_{\text{xs}})_0$ durations of H2 and H1	77
2.4.5 $(^{231}\text{Pa}_{\text{xs}}/^{230}\text{Th}_{\text{xs}})_0$ and paleoceanographic implications.....	79
2.5 CONCLUSION.....	81
ACKNOWLEDGMENTS.....	82
REFERENCES	83

FIGURES	88
CONCLUSION GÉNÉRALE.....	97
ANNEXE A	
AUTHIGENIC, DETRITAL AND DIAGENETIC MINERALS IN THE	
LAGUNA POTROK AIKE SEDIMENT SEQUENCE	102
ABSTRACT.....	103
A.1. INTRODUCTION.....	104
A.2. REGIONAL SETTINGS	106
A.3. MATERIALS AND METHODS	108
A.3.1. Materials.....	108
A.3.2. Analytical procedures.....	109
A.4. RESULTS	112
A.4.1. Mineralogical assemblages	112
A.4.2. U and Th data.....	113
A.5. DISCUSSION	115
A.5.1. Paleoenvironmental changes.....	115
A.5.2. U-Th "dating" of vivianite	118
A.6. CONCLUSION.....	121
ACKNOWLEDGMENTS.....	122
REFERENCES	123
FIGURES	127
ANNEXE B	
TABLEAUX DES DONNÉES	139
TABLEAU 1 – DONNÉES ISOTOPIQUES DES ANALYSES DE LA SÉQUENCE SÉDIMENTAIRE HU08-029-016PC, OBTENUES PAR COMPTAGE ALPHA (CONCENTRATIONS EN U ET EN TH, ET RAPPORTS D'ACTIVITÉ)	139
TABLEAU 2 – DONNÉES ISOTOPIQUES DES ANALYSES DE LA SÉQUENCE SÉDIMENTAIRE HU08-029-004PC, OBTENUES PAR TIMS (POUR LES 40 PREMIERS CM) ET PAR COMPTAGE ALPHA (CONCENTRATIONS EN U ET EN TH, ET RAPPORTS D'ACTIVITÉ)	142

TABLEAU 3 – DONNÉES ISOTOPIQUES DES ANALYSES DE LA SÉQUENCE SÉDIMENTAIRE HU08-029-004PC, OBTENUES AU MC-ICP-MS.....	146
TABLEAU 4 – DONNÉES DE MINÉRALOGIE DE LA SÉQUENCE SÉDIMENTAIRE HU08-029-004PC, OBTENUES PAR LA TECHNIQUE DE DIFFRACTION AUX RAYONS X (ABONDANCES RELATIVES EN %).....	148
TABLEAU 5 – DONNÉES DE CARBONE (CARBONE TOTAL -C-, CARBONE ORGANIQUE -C _{ORG} -, CARBONE INORGANIQUE -C _{INORG} -) DE LA SÉQUENCE SÉDIMENTAIRE HU08-029-004PC (EN % DU POIDS SEC DU SÉDIMENT TOTAL).	157
BIBLIOGRAPHIE	165

LISTE DES FIGURES

Figure	Page
0.1 Carte de localisation des sites de prélèvement des séquences sédimentaires HU08-029-004PC et HU08-029-016PC en mer du Labrador et en baie de Baffin	14
0.2 Images CAT-scan et photographies des carottes de la séquence HU08-029-016PC et profil sismique de la zone d'échantillonnage	15
0.3 Images CAT-scan et photographies des carottes de la séquence HU08-029-004PC et profil sismique de la zone d'échantillonnage.	16
0.4 Carte générale de la région de la baie de Baffin et de la mer du Labrador- bathymétrie, circulation océanique et géologie	17
0.5 Les trois chaînes de désintégration radioactive naturelles.....	18
1.1 Location map of core HU2008-029-016PC in Baffin Bay	50
1.2 Age-depth model of core HU2008-029-016PC	51
1.3 Geochemical properties and isotopic ratios <i>vs</i> age	52
1.4 U and Th data in the study sequence <i>vs</i> age	53
1.5 Sedimentological, mineralogical and geochemical properties plotted <i>vs</i> age with initial excess of ^{230}Th	54
1.6 The inventory of $(\text{F}^{230}\text{Th}_{\text{xs}})_{\text{M}}$ in the sediment column	55
1.S1 $(^{230}\text{Th}_{\text{xs}})_0$ activity ($\text{dpm.g}^{-1}; \pm 1\sigma$) plotted <i>vs</i> age	56
1.S2 Fraction in dry weight bulk sediment (dw%) of total carbon and organic carbon	57
2.1 Location map of core HU08-029-004PC in the Labrador Sea	88
2.2 Age depth model of core HU08-029-004PC	89
2.3 Mineralogical abundance <i>vs</i> core depth and age	90
2.4 Sedimentological parameters <i>vs</i> age	91
2.5 U-, Th- and Pa-concentrations, mass and activity ratios <i>vs</i> age	92
2.6 ^{230}Th - and ^{231}Pa -concentrations and activity ratios, and $(^{230}\text{Th}_{\text{xs}})_0$ inventory <i>vs</i> age	93

2.S1 Analytical uncertainties for ^{230}Th and ^{231}Pa	94
2.S2 Changes in $^{234}\text{U}/^{238}\text{U}$ activity ratios and sulfur content vs depth in the 90-013-013 sediment sequence (Greenland continental slope).	95
2.S3 Fraction in dry weight bulk sediment (dw%) of total carbon and organic carbon	96
A.1 Location, bathymetry and description of Laguna Potrok Aike.....	127
A.2 Photographs of vivianite samples	128
A.3 Evolution of the mineralogy according to X-ray patterns of the <63 μm fraction in 10 m steps for the Laguna Potrok Aike sediment sequence.....	129
A.4 Semi-quantitative mineral abundances vs. age and composite depth for major minerals with lithostratigraphy.....	130
A.5 Results from PCA on the five main mineralogical assemblages (fraction <63 μm).	131
A.6 Scores of PC1 (left) and PC2 (right) of the five main mineralogical assemblages (fraction <63 μm) plotted vs ages.....	132
A.7 Mineralogical data for the fraction <2 μm	133
A.8 XRD spectra obtained from the four vivianite samples V1 to V4.....	134
A.9 One of the SEM-EDS spectra from a vivianite-rich region of concretion V5.....	135

LISTE DES TABLEAUX

Tableau	Page
A.1 Mean ($\pm 1\sigma$) of the semi-quantitative relative abundance (%) and measured d-spacing (Å) reflection intensity for bulk (<63 µm) and clay (<2 µm) fraction minerals over the entire sequence.....	136
A.2 U-Th concentrations and activity ratios of vivianite samples	137
A.3 Estimates of authigenic vs. detrital U-fractions in the studied samples.	138
B.1 Données isotopiques des analyses de la séquence sédimentaire HU08-029-016PC, obtenues par comptage alpha.....	139
B.2 Données isotopiques des analyses de la séquence sédimentaire HU08-029-004PC, obtenues par TIMS (pour les 40 premiers cm) et par comptage alpha.	142
B.3 Données isotopiques des analyses de la séquence sédimentaire HU08-029-004PC, obtenues au MC-ICP-MS.	146
B.4 Données de minéralogie de la séquence sédimentaire HU08-029-004PC, obtenues par la technique de diffraction aux rayons X (abondances relatives en %).	148
B.5 Données de carbone (carbone total -C-, carbone organique -C _{org} -, carbone inorganique -C _{inorg} -) de la séquence sédimentaire HU08-029-004PC (en % du poids sec du sédiment total).	157

RÉSUMÉ

L'océan Atlantique Nord joue un rôle essentiel au niveau du climat et de la circulation océanique globale. Dans cette perspective, la baie de Baffin et la mer du Labrador comportent plusieurs caractéristiques intéressantes :

- (i) elles constituent des bassins de transition de masses d'eau entre l'océan Arctique et l'Atlantique Nord,
- (ii) elles participent à la circulation méridienne de renversement atlantique en contribuant à la formation des eaux profondes froides, et,
- (iii) leur localisation, aux marges des anciennes calottes glaciaires nord-américaines et de la calotte groenlandaise, permet d'étudier l'impact de la dynamique des calottes de glace sur la circulation océanique et, indirectement, sur le climat.

Les sédiments de ces bassins sont donc susceptibles d'avoir enregistré des informations pertinentes pour l'étude de l'évolution paléoclimatique/paléocéanographique de la région.

Cette thèse porte sur l'application des isotopes de trois éléments chimiques de la famille des actinides, l'uranium (U), le thorium (Th) et le protactinium (Pa), à l'étude de deux séquences sédimentaires provenant de bassins océaniques de l'Atlantique du Nord-Ouest et couvrant le dernier cycle glaciaire. L'approche multi-paramètres appliquée associe ce volet isotopique à des informations sédimentologiques complémentaires (i.e., données physiques, minéralogiques et géochimiques). La première carotte sédimentaire provient de la plaine abyssale centrale de la baie de Baffin. La seconde a été prélevée en mer du Labrador, à environ 180 km à l'est de l'embouchure du détroit d'Hudson. La thèse est donc divisée en deux chapitres majeurs portant chacun sur une de ces régions. Les données relatives aux isotopes des actinides U, Th et Pa sont utilisées comme traceurs des processus et flux géochimiques dans le sédiment, et de la dynamique particulière propre aux sites étudiés. Les deux sujets abordés contribuent dès lors à l'effort de recherche visant à mieux comprendre le comportement, l'évolution et l'interaction des systèmes océan, atmosphère, cryosphère dans l'Hémisphère Nord au cours du Quaternaire récent.

Le premier chapitre porte sur l'analyse de la séquence sédimentaire provenant de la baie de Baffin. Les 7.41 m de sédiment récupérés s'étendent temporellement sur l'entièreté du dernier cycle glaciaire, depuis le stade isotopique 5d jusqu'à aujourd'hui (les derniers ~115 ka). La baie de Baffin constitue une zone de transition des masses d'eau atlantiques et arctiques, en plus d'avoir été fortement influencée par

la dynamique des grandes calottes de glace de l'Amérique du Nord et du Groenland durant les glaciations du Quaternaire. Réalisées à intervalles de ~1.6 ka, les mesures de concentrations et de rapports isotopiques en U et en Th combinées à d'autres paramètres sédimentologiques mettent en évidence les processus et flux géochimiques et sédimentaires complexes relatifs au site étudié. De plus, les profils de ^{230}Th en excès permettent de retracer l'évolution de la dynamique particulaire dans le bassin. Les résultats mettent en évidence deux conditions océanographiques différentes comprenant une nette transition entre la dernière période glaciaire et l'interglaciaire actuel. Une remobilisation importante des particules sur les pentes continentales, avec focalisation vers la plaine abyssale, semble avoir été active durant la dernière période glaciaire. En revanche, durant l'Holocène, un déficit en ^{230}Th par rapport à la production dans la colonne d'eau sus-jacente s'observe et semble démontrer un renforcement de la ventilation des masses d'eau en zone profonde, témoignant de la mise en place de la circulation océanique actuelle.

Le deuxième chapitre de cette thèse se concentre sur la séquence sédimentaire de 8.95 m de long prélevée dans le nord-ouest de la mer du Labrador. Cette région océanique tient un rôle essentiel dans la formation des eaux intermédiaires et profondes froides participant à la boucle de circulation de renversement méridienne atlantique. Sa proximité avec le détroit d'Hudson en fait également une zone privilégiée pour étudier les épisodes de fonte de la calotte de glace des Laurentides. Les données isotopiques en U, Th et Pa sont intégrées dans une approche multi-paramètres et utilisées pour caractériser les processus et flux géochimiques et sédimentaires en relation avec les variations cryosphériques, océaniques et climatiques passées. La dynamique particulaire depuis le glaciaire tardif (i.e., les ~37 derniers ka) est évaluée à travers l'étude des variations des excès en ^{230}Th et ^{231}Pa enregistrés dans la colonne sédimentaire. Le mode et le temps de dépôt des décharges carbonatées identifiées comme se rapportant aux événements de Heinrich H2 et H1 sont évalués à l'aide d'inventaires du ^{230}Th en excès. Des processus géochimiques et flux particulaires variables et complexes sont par ailleurs observés pour ce site localisé en zone de marge continentale. Cette variabilité, associée aux limitations méthodologiques rencontrées, pose des incertitudes quant à l'estimation précise des excès en ^{231}Pa et en ^{230}Th dans ces conditions environnementales particulières. Certains intervalles, notamment la fin de la période glaciaire et de l'Holocène, montrent des valeurs de flux d'excès de ^{230}Th excédant la valeur théorique du flux provenant de la colonne d'eau sus-jacente, indiquant probablement une augmentation de l'advection ou des processus de redistribution sédimentaire. Enfin, les valeurs des rapports des excès initiaux de ^{231}Pa sur ^{230}Th généralement inférieures à la valeur de production verticale de la colonne d'eau suggèrent une exportation du ^{231}Pa vers le sud par advection.

Mots clés : Paléocéanographie; Quaternaire récent; Traceurs isotopiques; Sédimentation; Séries de l'U et du Th.

INTRODUCTION

0.1 Problématique

L'océan est un acteur majeur du climat. Il joue un rôle essentiel dans les mécanismes qui le gouvernent, en interagissant avec l'atmosphère par le biais d'échanges d'énergie et de matière. L'étude des changements dans la circulation océanique est donc fondamentale pour mieux comprendre la dynamique des fluctuations climatiques millénaires et glaciaires-interglaciaires du Quaternaire (Broecker et Denton, 1989). Une des composantes majeures de la circulation océanique actuelle et passée est la convection des masses d'eau intermédiaires et profondes aux hautes latitudes (Broecker, 1991). En Atlantique Nord, ces mouvements s'opèrent dans la mer du Groenland, de Norvège et du Labrador. Les masses d'eau engendrées participent ensuite à la ventilation de l'océan mondial (Broecker, 1987; Broecker, 1991). La baie de Baffin et la mer du Labrador font partie intégrante de ce système (Fig. 1). Elles sont le lieu de formation et de passage des masses d'eau qui contribuent de manière essentielle à la circulation méridienne de renversement en Atlantique (*Atlantic Meridional Overturning Circulation*, AMOC; Fig. 1; Broecker, 1987).

Ces deux bassins ont également constitué l'un des exutoires des eaux de fonte des grandes calottes glaciaires d'Amérique du Nord (calottes inuitienne, groenlandaise et laurentidienne), c'est-à-dire un lien entre ces calottes et l'océan Atlantique (Dyke *et al.*, 2002). Leurs sédiments sont donc susceptibles d'avoir enregistré les épisodes de fonte de ces masses de glace et leur étude a notamment déjà permis d'acquérir de l'information sur les évènements qui y sont associés (e.g., évènements de Heinrich, Dryas récent, évènement 8.2 cal ka; e.g., Andrews et Tedesco, 1992; Andrews, 1998; Barber *et al.*, 1999; Broecker *et al.*, 2010; Lewis *et al.*, 2012). La découverte des évènements de Heinrich en Atlantique Nord (Heinrich, 1988) a par exemple mis en

évidence que la fonte de la calotte de glace des Laurentides aurait rapidement libéré de grandes quantités d'eau douce dans l'océan Atlantique, et ce essentiellement à travers le détroit d'Hudson (Andrews et Tedesco, 1992; Andrews et Maclean, 2003; Hemming *et al.*, 1998). Ces évènements ont depuis motivé de nombreuses recherches sur leurs conséquences pour l'environnement, non seulement à une échelle régionale, mais également mondiale (voir Hemming, 2004 pour une revue de la littérature).

Les fluctuations climatiques abruptes de la fin du Pléistocène et de l'Holocène paraissent clairement liées aux variations dans la circulation océanique (e.g., Bond et Lotti, 1995; Bond *et al.*, 1993). Cependant, les mécanismes à l'origine de ces variations océaniques et climatiques ne font pas encore l'objet d'un consensus dans la communauté scientifique et de nombreuses questions subsistent encore quant aux conséquences de ces phénomènes. S'il est généralement établi que les déversements d'eau douce auraient affaibli l'AMOC (e.g., Clarke *et al.*, 2009), la compréhension de l'ensemble des processus par lesquels ces événements ont mené à cette perturbation demeure partielle (e.g., Hillaire-Marcel *et al.*, 2001; Lynch-Stieglitz *et al.*, 2007; McManus *et al.*, 2004). Connaître davantage les mécanismes de transport et les types de dépôts sédimentaires associés à ces épisodes, ainsi que leurs durées précises respectives, permettrait de mieux cerner les processus impliqués.

0.2 Objectifs

Étudier précisément la dynamique océanique passée des bassins de l'Atlantique du Nord-Ouest durant le Quaternaire récent est essentiel pour la compréhension de l'océanographie de la région. Cela permet d'interpréter davantage son influence sur la circulation globale et de mieux cerner les fluctuations climatiques millénaires et glaciaires-interglaciaires du Quaternaire, leurs causes et leurs conséquences. Dès lors, les principaux objectifs de cette thèse sont les suivants :

- (i) Évaluer les sources, les flux et les processus géochimiques et sédimentaires des sites étudiés;
- (ii) Obtenir de l'information sur les variations dans le débit des masses d'eau intermédiaires et profondes au cours de la dernière glaciation et de l'interglaciaire actuel, et mieux cerner les fluctuations dans le schéma de circulation de l'AMOC;
- (iii) Examiner la réponse sédimentaire à la dynamique des grandes calottes de glace de la région pour la dernière période glaciaire;
- (iv) Améliorer la compréhension des épisodes sédimentologiques brefs (i.e., échelles centenaires à millénaires) tels que les événements de Heinrich, et évaluer leurs conséquences sur l'océanographie et le climat de la région.

0.3 Région d'étude

Les deux bassins océaniques de l'Atlantique du Nord-Ouest que sont la baie de Baffin et la mer du Labrador se sont formés il y a environ 62 à 34 Ma avant notre ère, suite à l'écartement progressif du plancher océanique (Blinova *et al.*, 2009). Les cratons précambriens se sont alors écartés progressivement pour atteindre leur position actuelle.

La baie de Baffin est un bassin océanique subarctique semi-fermé de ~1400 km de long, ~550 km de large et ~2300 m de profondeur au niveau de sa plaine centrale (Tang *et al.*, 2004). Elle est bordée par l'île de Baffin à l'ouest, l'archipel Arctique canadien au nord et le Groenland à l'est (Figs. 1, 4). La bathymétrie de la baie est asymétrique, avec un plateau continental de largeur supérieure à 150 km au niveau de la côte du Groenland et de largeur inférieure à 35 km au niveau de l'île de Baffin. Ces

deux régions sont également caractérisées par des pentes abruptes (Fig. 1, 4; Aksu, 1983a; voir Simon, 2013 pour plus de détails sur la région d'étude).

Au sud, le bassin de la mer du Labrador est situé entre la côte du Labrador et le Groenland. Sa profondeur d'eau maximale atteint ~3400 m et sa largeur ~1000 km. Au niveau du détroit de Davis, sa profondeur est de ~650 m (Tang *et al.*, 2004). La mer du Labrador est en partie jalonnée par le chenal médio-océanique de l'Atlantique du Nord-Ouest (*Northwest Atlantic Mid-Ocean Channel*, NAMOC), qui est constitué de chenaux et canyons sous-marins encaissés de 100 à 200 m dans la topographie du bassin et d'une largeur de 2 à 5 km. Le NAMOC suit l'axe NO-SE de la mer du Labrador sur une distance d'environ 3800 km à partir de l'embouchure du détroit d'Hudson avant de rejoindre l'Atlantique Nord (Hesse *et al.*, 1997; Hesse et Rakofsky, 1992).

La baie de Baffin et la mer du Labrador constituent, avec le détroit de Fram, une des zones de transition et de mélange des masses d'eau arctiques et atlantiques. Les eaux de surface froides et relativement peu salées de l'océan Arctique traversent l'archipel Arctique canadien et aboutissent dans la baie de Baffin. Cette masse d'eau arctique (*Arctic Water*, AW) se situe du côté ouest de la baie, en surface (~0-300 m). Deux autres masses d'eau sont également présentes : la masse d'eau intermédiaire ouest-groenlandaise (~300-800 m; *West Greenland Intermediate Water*, WGIW) et la masse d'eau profonde (*Baffin Bay Deep Water*, BBDW), localisée dans la région centrale de la baie (Tang *et al.*, 2004). La circulation y est dominée par un mouvement cyclonique et est caractérisée par deux composantes principales (Tang *et al.*, 2004; Fig. 1). A l'est, le courant ouest-groenlandais (*West Greenland Current*, WGC) est principalement alimenté par une masse d'eau issue du courant est-groenlandais (*East Greenland Current*, EGC) qui entre en baie de Baffin à travers le détroit de Davis (Fig. 1). A l'ouest, les masses d'eau sont entraînées par le courant de

l'île de Baffin (*Baffin Island Current*, BIC) s'écoulant vers le sud, et transitant ensuite dans la mer du Labrador via le détroit de Davis (*Davis Strait Overflow*, DSO; Tang *et al.*, 2004).

Comme mentionné plus haut, la mer du Labrador constitue actuellement l'un des trois bassins de convection des masses d'eau en Atlantique Nord. Sous l'effet du refroidissement hivernal, les eaux de surface plongent et forment la masse d'eau intermédiaire de la mer du Labrador (*Labrador Sea Water*, LSW; Lazier, 1973). La masse d'eau de fond ($\leq \sim 3300$ m) est occupée par les eaux de débordement du détroit du Danemark (*Denmark Strait Overflow Water*, DSOW), générées dans la mer du Groenland. Entre les deux (~ 2300 - 3300 m de profondeur) on retrouve les masses d'eau intermédiaires et profondes de l'Atlantique du Nord-Est provenant des bassins d'Irminger et d'Islande (*North East Atlantic Deep Water*, NEADW) et issues de la mer de Norvège (Lazier *et al.*, 2002). Elles sont toutes entraînées par le sous-courant côtier de l'ouest (*Western Boundary Undercurrent*, WBUC) en mer du Labrador (Fig. 1), et l'ensemble de ces masses d'eau et leur interaction concourent à la formation des eaux profondes de l'Atlantique Nord (*North Atlantic Deep Water*, NADW), qui entament ensuite leur lente descente vers le sud (e.g., Dickson et Brown, 1994; Marshall et Schott, 1999).

0.4 Matériel

Deux séquences sédimentaires, HU08-029-016PC et HU08-029-004PC, sont étudiées en détail dans le cadre de cette thèse. Elles ont été récoltées à l'aide d'un système de carottage à piston lors de l'expédition 2008-029 qui s'est déroulée en baie de Baffin et ses régions adjacentes à bord du *CCGS Hudson* en 2008 (Campbell et de Vernal, 2009).

La carotte HU08-029-016PC mesure 741 cm de long et a été prélevée dans la plaine abyssale du centre de la baie de Baffin ($70^{\circ}27'N$; $64^{\circ}39'O$), à une profondeur de 2063 m (Figs. 1, 2, 4). La sédimentation de la baie a été fortement influencée par la dynamique des calottes glaciaires de la région, comme en témoigne l'abondance des débris de vêlage d'icebergs qu'on y retrouve. A contrario, une sédimentation hémipelagique semble dominer dans le fond du bassin durant l'interglaciaire actuel, avec de très faibles taux de sédimentation (Simon, 2013; Simon *et al.*, 2012; Simon *et al.*, 2014). Par ailleurs, l'interprétation des signaux enregistrés dans le sédiment de ce bassin fût longtemps limitée par l'impossibilité de mettre en place des chronologies fiables. Le manque de marqueurs chronostratigraphiques et de microfossiles rend difficile l'établissement des stratigraphies $\delta^{18}O$ et les datations radiocarbonées. En effet, durant les ères glaciaires, le bassin devait être recouvert de manière quasiment permanente par de la glace de mer limitant la pénétration du flux d'énergie solaire dans la couche d'eau superficielle (de Vernal *et al.*, 1987). Par ailleurs, les eaux sous-saturées en ions (e.g., Azetsu-Scott *et al.*, 2010) auraient entraîné la dissolution des carbonates dans les sédiments de surface du bassin profond durant l'interglaciaire actuel (de Vernal *et al.*, 1992). De plus, les facteurs de correction de l'effet réservoir des paléo-masses d'eau de ce bassin ne sont pas encore établis avec précision, augmentant l'incertitude sur les âges radiocarbonées. Enfin, les rares mesures $\delta^{18}O$ obtenues étaient par ailleurs difficiles à interpréter suite aux perturbations locales (aussi bien les déversements massifs d'eaux douces continentales que la distillation des saumures produite lors la formation de la glace de mer) des signaux $\delta^{18}O$.

Les études paléocéanographiques et paléoclimatiques ont dès lors été rares et parfois peu concluantes d'un point de vue chronostratigraphique (e.g., Aksu, 1983a; b; Aksu et Piper, 1979; de Vernal *et al.*, 1987). Cependant, Simon *et al.* (2012) ont récemment réussi à établir un modèle d'âge pour la séquence 016PC, principalement à partir de

données paléomagnétiques. Ils ont déduit un âge basal de ~115 ka et une vitesse de sédimentation moyenne d'environ 6.5 cm.ka⁻¹.

La carotte de sédiment HU08-029-004PC mesure 895 cm de long et a été prélevée à 2674 m de profondeur en mer du Labrador (61°27'N; 58°2'O) à ~180 km de l'embouchure du détroit d'Hudson (Figs. 1, 3). Les sédiments sont généralement constitués d'un mélange d'argiles et de limons gris foncés incorporant occasionnellement des débris plus grossiers provenant de délestages par les icebergs. Cette matrice sédimentaire alterne avec des horizons bruns relativement épais (jusqu'à 100 cm) laminés et sableux typiques d'événements sédimentologiques brefs associés aux événements de Heinrich (e.g., Broecker *et al.*, 1992; Heinrich, 1988). La chronologie de la séquence, réalisée à partir de dates radiocarbonées, a été construite par Gibb *et al.* (2014). Elle a livré un âge basal de ~36.6 cal ka BP et un taux de sédimentation moyen de ~24.4 cm.ka⁻¹, bien que ce dernier soit très variable dans la séquence.

0.5 Approche méthodologique

Cette thèse traite plus spécifiquement de l'utilisation des isotopes de trois éléments chimiques de la famille des actinides (i.e., uranium (U), thorium (Th) et protactinium (Pa)) dans l'étude des séquences sédimentaires marines précitées. Les isotopes de l'U, du Th et du Pa présentent diverses possibilités d'application et sont utilisés ici comme traceurs de la dynamique géochimique et sédimentaire en milieu océanique.

Les déséquilibres des séries de désintégration de l'U et du Th font référence au fractionnement des isotopes de ces séries ayant lieu dans la nature au cours des différents processus géologiques (Fig. 5; e.g., Bourdon *et al.*, 2003; Cochran, 1992). Ils sont dus aux différences de propriétés physico-chimiques de ces isotopes : un

fractionnement peut se produire en fonction de leurs valences et affinités chimiques respectives (cf. Cheng *et al.*, 1998). Dans l'environnement aquatique, le fractionnement des isotopes des séries de l'U et du Th est principalement dû aux différences de solubilité (e.g., Cochran et Masqué, 2003; Henderson et Anderson, 2003). Les différents nucléides peuvent donc être classés en deux groupes : ceux qui restent dissous de manière stable dans l'eau (e.g., isotopes de l'U, du radium -Ra-), et ceux qui s'associent avec des particules et qui sont par conséquent soustraits de la colonne d'eau par adsorption ou co-précipitation (e.g., isotopes du Th, du Pa, du plomb -Pb-; Cochran, 1992). Ces comportements physico-chimiques différents mènent à des déséquilibres radioactifs dans les différentes phases de l'environnement océanique. Enfin, grâce à leur désintégration radioactive ils peuvent servir d'outils géochronologiques et fournir des informations sur les rendements et les échelles de temps de processus dynamiques induisant un fractionnement (e.g., circulation des masses d'eau, productivité, sédimentation; e.g., Henderson et Anderson, 2003).

L'U parvient à l'océan principalement par les rivières, l'eau de ruissellement et les eaux souterraines. Son temps de séjour océanique est estimé à ~500 ka (Faure et Mensing, 2005). La concentration en uranium peut être raisonnablement considérée comme uniforme et constante dans l'océan ($3,123 \pm 0,107 \text{ ng.g}^{-1}$ pour une salinité de 35; e.g., Not *et al.*, 2012) au cours de la période étudiée (~115 ka), et en négligeant les ~3 % de variation de concentration liées aux fluctuations glaciaires-interglaciaires de la masse océanique. Le comportement de l'U dans le milieu océanique est régi principalement par les conditions d'oxydoréduction, le processus de recul alpha engendrant par surcroît un déséquilibre entre ^{234}U et son descendant ^{238}U . Dans la colonne d'eau en condition oxydante, l'U est en solution sous la forme d'ions uranyles (UO_2^{2+}) en un état hexavalent (+VI). La soustraction de l'U de la colonne d'eau s'effectue principalement par :

- (i) précipitation dans les sédiments lors de sa réduction en sa forme tétravalente (+IV) sous l'effet de conditions réductrices (e.g., Gariepy *et al.*, 1994),
- (ii) inclusion dans les minéraux authigènes (e.g., transformation des ions uranyles UO_2^{2+} en complexes carbonatés $\text{UO}_2(\text{CO}_3)_3^{4-}$ et co-précipitation avec les carbonates de calcium biogéniques) ou,
- (iii) lors de la formation d'oxydes (i.e., oxydes de fer ou de manganèse -Mn-; e.g., Cochran, 1992; Faure et Mensing, 2005; Henderson et Anderson, 2003).

La désintégration radioactive des isotopes de l'uranium (i.e., ^{234}U et ^{235}U respectivement) présents sous forme dissoute dans la colonne d'eau produit les radionucléides ^{230}Th et ^{231}Pa . Les périodes radioactives ($t_{1/2}$) correspondantes sont les suivantes :

- $t_{1/2}(^{230}\text{Th}) = 75690 \pm 230$ ans; Cheng *et al.*, 2000;
- $t_{1/2}(^{231}\text{Pa}) = 32760 \pm 220$ ans; Cheng *et al.*, 1998;
- $t_{1/2}(^{234}\text{U}) = 245250 \pm 490$ ans; Cheng *et al.*, 2000;
- $t_{1/2}(^{235}\text{U}) = 7.0381 \pm 0.0096 \cdot 10^8$ ans; Begemann *et al.*, 2001.

Comme le ^{230}Th et le ^{231}Pa sont produits de manière uniforme, les flux de ces radionucléides produits dans la colonne d'eau sont sensiblement constants (François, 2007) :

$$\beta_{230\text{Th}} = \lambda_{230\text{Th}} A_{234\text{U}} \approx 9,2 \cdot 10^{-6} \cdot 2910 \approx 2,67 \cdot 10^{-2} \text{ dpm m}^{-3} \text{ an}^{-1}$$

$$\beta_{231\text{Pa}} = \lambda_{231\text{Pa}} A_{235\text{U}} \approx 2,12 \cdot 10^{-5} \cdot 116 \approx 2,46 \cdot 10^{-3} \text{ dpm m}^{-3} \text{ an}^{-1}$$

où le symbole β correspond au taux de production, λ est la constante de désintégration et A l'activité de l'élément considéré.

Contrairement aux isotopes de l'uranium, ceux du Pa et du Th sont très réactifs. Ils ont tendance à s'adsorber à la surface des particules organiques ou minérales présentes dans la colonne d'eau et sont par conséquent enfouis avec celles-ci dans le sédiment. Il s'agit du processus décrit sous le nom de "scavenging" (Anderson *et al.*, 1983b). Dès lors, en supposant que toute la quantité de radio-isotopes produits dans la colonne d'eau se trouve enfouie dans le site sous-jacent, les sédiments marins présentent une activité ^{230}Th et ^{231}Pa des sédiments récents en excès (i.e., activités non soutenues par la désintégration de l'uranium du sédiment) avec un rapport théorique de l'excès de ^{231}Pa sur celui du ^{230}Th de ~0.092, avant décroissance radioactive de ces excès.

Au-delà de ces propriétés assez voisines, des différences peuvent s'observer entre le Pa et le Th qu'il est possible d'exploiter. Tout d'abord, le thorium est un peu plus réactif que le protactinium. L'extrême réactivité du ^{230}Th avec les particules permet de l'utiliser comme outil de normalisation des flux particulaires (e.g., François *et al.*, 2004) et géochimiques (e.g., ^{231}Pa ; François, 2007; Hoffmann *et al.*, 2013) et comme traceur des flux sédimentaires comme le "focusing" et le "winnowing", i.e. processus syn- ou post-sédimentaires de redistribution particulière par les courants profonds (e.g., François *et al.*, 1993; François *et al.*, 2004). Le temps de séjour du ^{230}Th dans les masses d'eau profondes est de l'ordre de 30 ans alors que celui du ^{231}Pa est de ~200 ans (Yu *et al.*, 1996). Ensuite, la distribution de ces radionucléides est notamment influencée par leurs différentes affinités chimiques en fonction de la composition des particules qui sédimentent (Chase *et al.*, 2002). Le Pa a davantage d'affinité avec l'opale et les oxydes de Mn que le Th qui a plus d'affinité avec les carbonates.

Etant donné son temps de séjour plus élevé, le ^{231}Pa produit a plus de chance que le ^{230}Th d'être exporté latéralement vers des régions de "scavenging" plus intense, i.e. où le flux en particules et/ou l'affinité avec les particules augmentent sa soustraction de la colonne d'eau. Le processus de transport par diffusion suivi d'un "scavenging" plus important dans des régions de plus faibles concentration en ^{231}Pa est connu sous le nom de "*boundary scavenging*" (Anderson *et al.*, 1983a). Dès lors, des rapports d'excès de ^{231}Pa sur ^{230}Th plus élevés s'observent généralement dans les sédiments des marges continentales, tandis que de plus faibles valeurs se retrouvent dans les sédiments de l'océan ouvert (e.g., Chase *et al.*, 2003; Kumar *et al.*, 1993). Ces effets s'observent par exemple clairement dans les sédiments du bassin du Pacifique, de l'Atlantique équatorial et des latitudes tropicales pour lesquels la productivité est plus abondante (e.g., Chase *et al.*, 2003; Yu *et al.*, 2001; Kumar *et al.*, 1993). Cependant, dans l'océan Atlantique, il a été montré que cet effet n'est pas le processus dominant contrôlant la répartition des radio-isotopes de ^{230}Th et de ^{231}Pa . En effet, les études de modélisation et paléocéanographiques (e.g., Marchal *et al.*, 2000; Yu *et al.*, 1996) semblent indiquer que les rapports $(^{231}\text{Pa}_{\text{xs}}/^{230}\text{Th}_{\text{xs}})_0$ enregistrés dans les sédiments de l'océan Atlantique pourraient plutôt refléter les changements passés dans le débit de la circulation intermédiaire et profonde. Le ^{231}Pa serait exporté latéralement par advection plutôt que par diffusion car le temps moyen de séjour du ^{231}Pa dans les masses d'eau profondes est équivalent au temps de séjour des masses d'eau intermédiaires et profondes dans l'Atlantique avant leur transit vers l'océan Austral (i.e., ~200 ans). Normalisé au $^{230}\text{Th}_{\text{xs}}$, les mesures de $^{231}\text{Pa}_{\text{xs}}$ dans les séquences sédimentaires peuvent donc donner des informations sur le processus de "scavenging", le flux de particules et le transport régional par les masses d'eau.

0.6 Contenu du manuscrit

La thèse se décline en deux chapitres majeurs écrits en langue anglaise, chacun correspondant à un article en voie de soumission dans une revue scientifique pour publication. Ils portent tous deux sur l'analyse d'une séquence sédimentaire et la méthodologie appliquée dans les deux cas est similaire.

Le *chapitre I* concerne la séquence sédimentaire de la baie de Baffin, s'étalant sur la quasi entièreté du dernier cycle glaciaire. À travers une analyse multi-paramètres basée principalement sur les isotopes de l'U et du Th le long de cette séquence, nous déterminons les processus et les flux géochimiques et sédimentaires du sédiment profond du bassin. De plus, à l'aide des données sur le ^{230}Th en excès nous en caractérisons la dynamique particulière des derniers ~115 ka, afin de dépeindre la dynamique océanique et climatique de la région. Les résultats obtenus aident à mieux cerner les processus sédimentaires internes au bassin et le rôle de la baie dans le schéma de circulation océanique régionale en regard de son lien avec la mer du Labrador à travers le détroit de Davis.

Le *chapitre II* porte sur la séquence sédimentaire de la mer du Labrador, s'étalant sur les derniers ~37 cal ka BP. Les isotopes de l'U, du Th et du Pa ont été mesurés régulièrement dans cette séquence et les données ont été combinées à d'autres données physiques, minéralogiques et géochimiques. Les informations recueillies permettent d'évaluer les processus et flux géochimiques et sédimentaires au site étudié. Les vitesses de dépôts des apports massifs en carbonates détritiques recensés (H2 et H1) sont estimées à l'aide des inventaires de ^{230}Th en excès selon la même procédure que celle appliquée par Veiga-Pires et Hillaire-Marcel (1999). Proche du détroit d'Hudson, ces informations deviennent cruciales car elles permettent de retracer avec précision la dynamique de la calotte de glace des Laurentides. De plus,

les budgets des isotopes radiogéniques ^{231}Pa sur ^{230}Th en excès dans les sédiments sont évalués et permettent d'obtenir de l'information sur la dynamique particulaire du bassin, ainsi que sur les fluctuations des courants de la région depuis la fin de la période glaciaire, en lien avec les épisodes de fonte de la calotte des Laurentides. Enfin, nous dressons les limitations méthodologiques quant à l'estimation de ces excès pour un site localisé en zone de marges continentales.

Finalement, nous achevons ce manuscrit par une conclusion générale dans laquelle sont présentés un résumé des retombées de nos recherches, ainsi que les perspectives scientifiques qui en découlent.

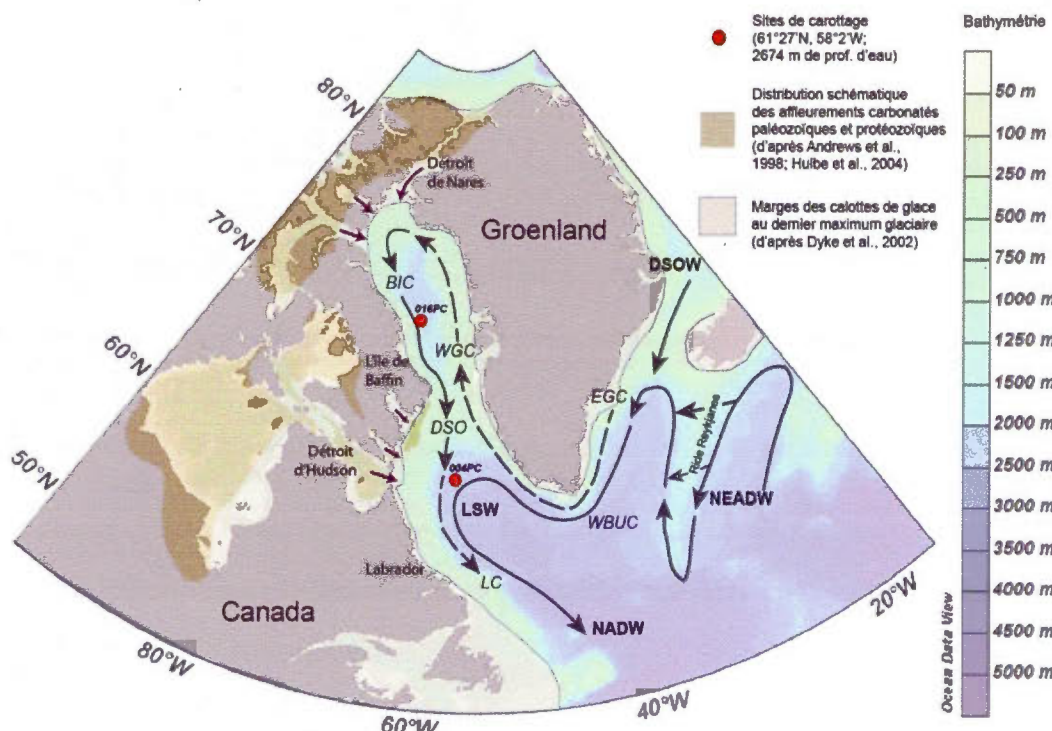


Figure 1 – Carte de localisation des sites de prélèvement des séquences sédimentaires HU08-029-004PC et HU08-029-016PC en mer du Labrador et en baie de Baffin, et représentant : la bathymétrie de la région, l'extension des calottes de glace au dernier maximum glaciaire, les zones d'affleurement des carbonates détritiques ainsi que leurs principales zones de sortie vers l'océan Atlantique, et enfin, une illustration schématique des composantes de la circulation de renversement méridienne Atlantique avec les courants profonds (traits continus) et intermédiaires (traits pointillés) et les acronymes des principales masses d'eau concernées (WGC – Western Greenland Current; BIC – Baffin Island Current; DSO – Davis Strait Overflow; LC – Labrador Current; EGC – East Greenland Current; WBUC – Western Boundary Undercurrent; NEADW – Northeast Atlantic Deep Water; LSW – Labrador Sea Water; DSOW – Denmark Strait Overflow Water; NADW – North Atlantic Deep Water).

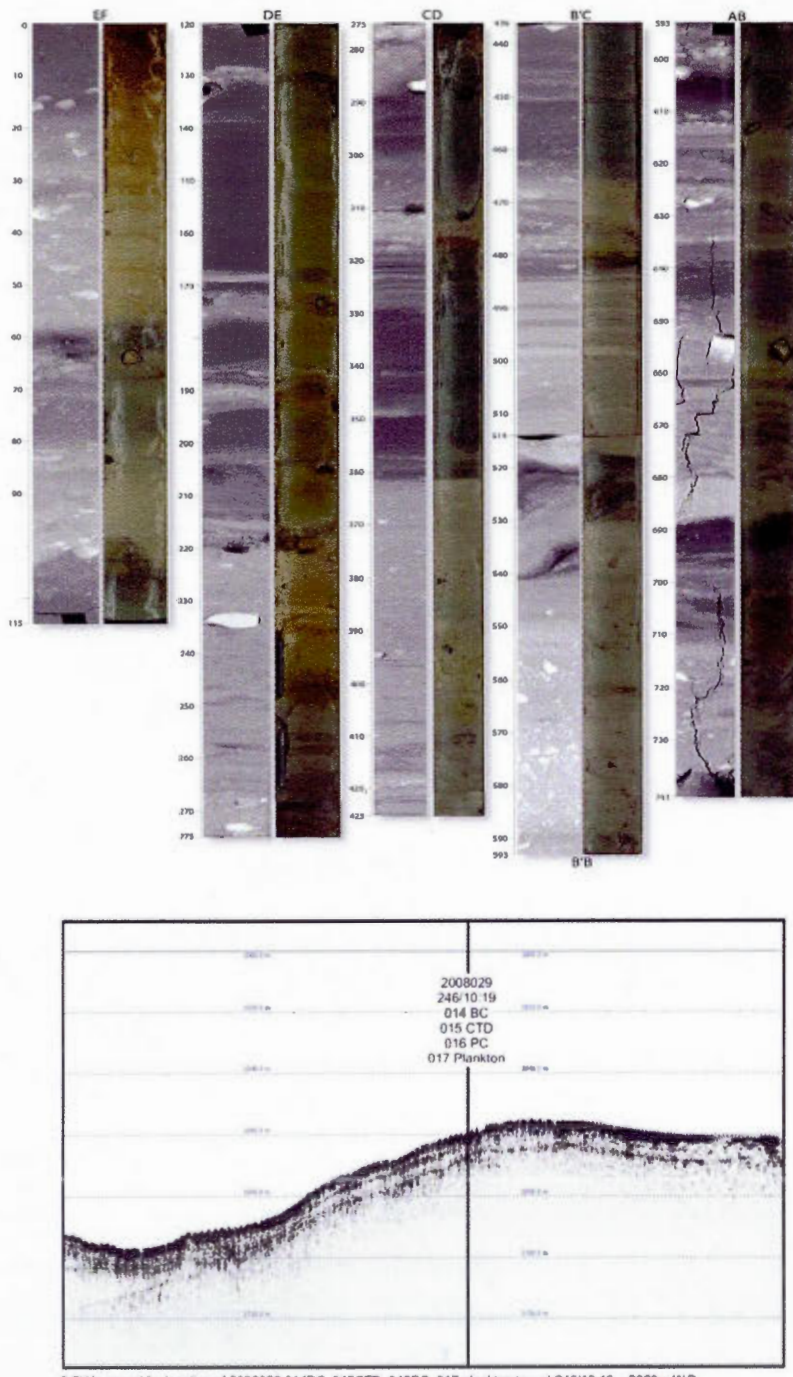


Figure 2 – Images CAT-scan et photographies des carottes de la séquence HU08 029-016PC et profil sismique de la zone d'échantillonnage

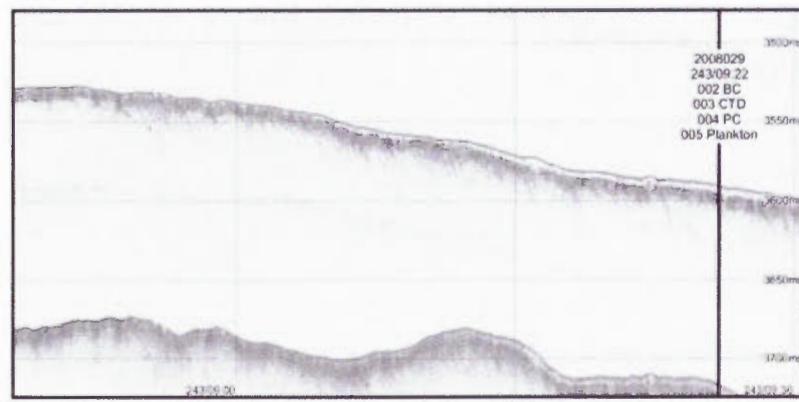
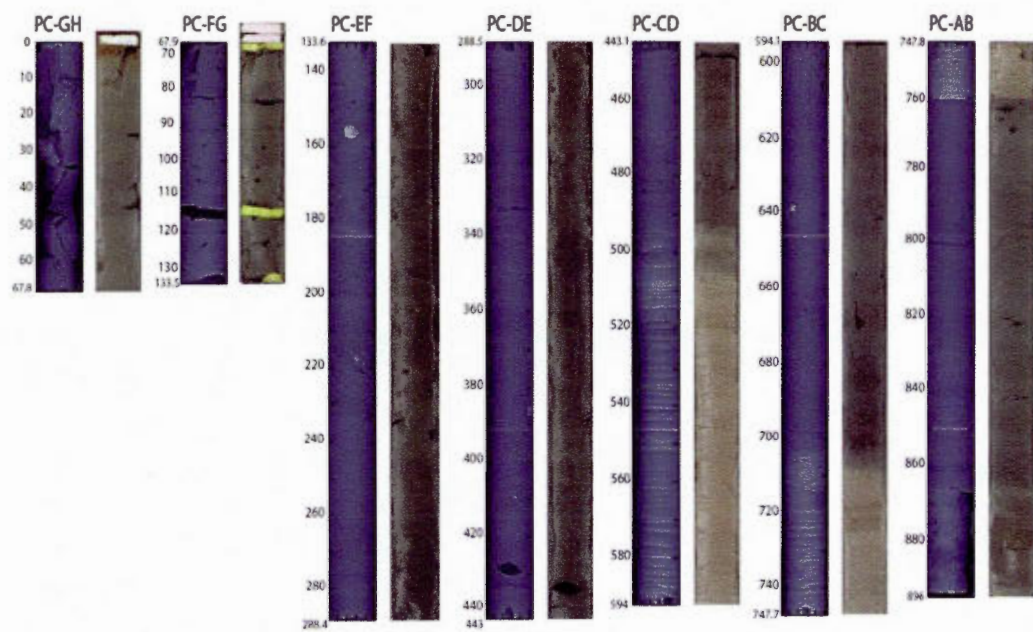


Figure 3 – Images CAT-scan et photographies des carottes de la séquence HU08-029-004PC et profil sismique de la zone d'échantillonnage.

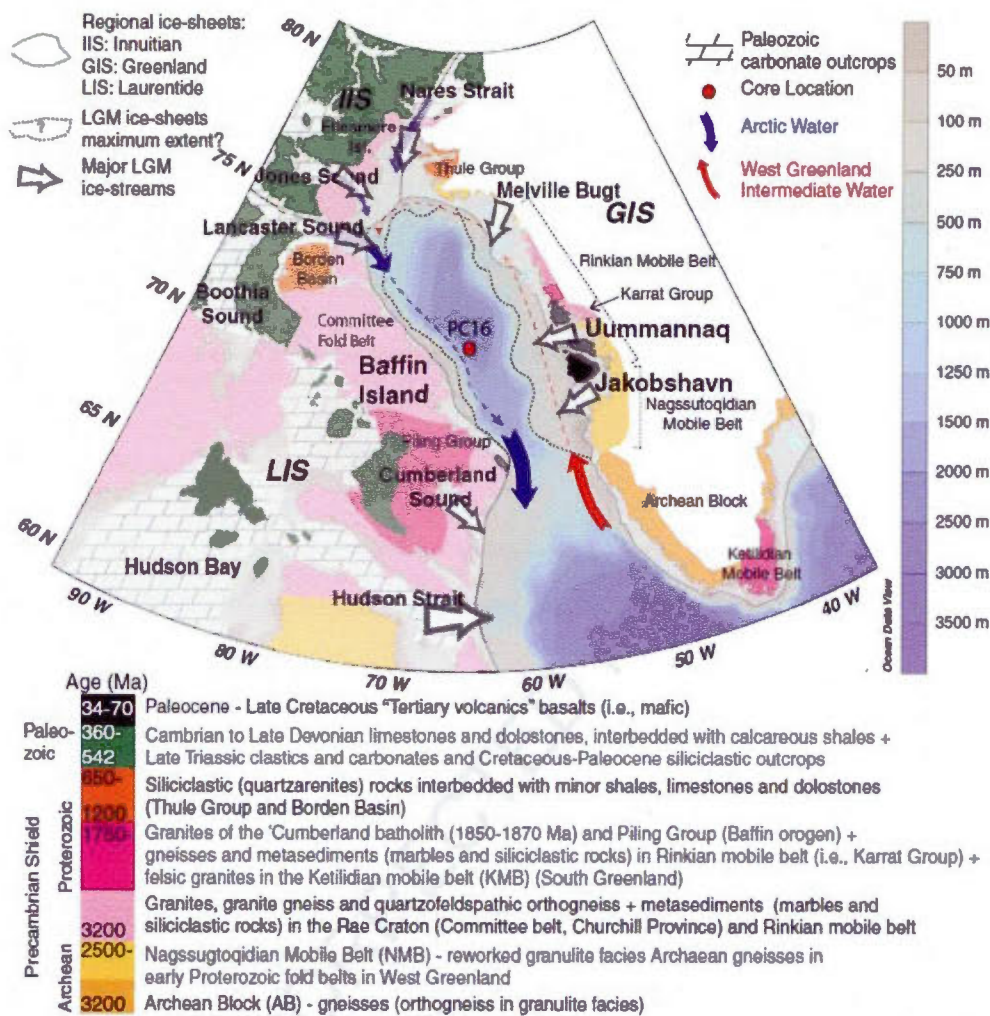


Figure 4 – Carte générale de la région de la baie de Baffin et de la mer du Labrador. La bathymétrie, la circulation océanique et la géologie y sont représentées de manière simplifiée (Simon *et al.*, 2014).

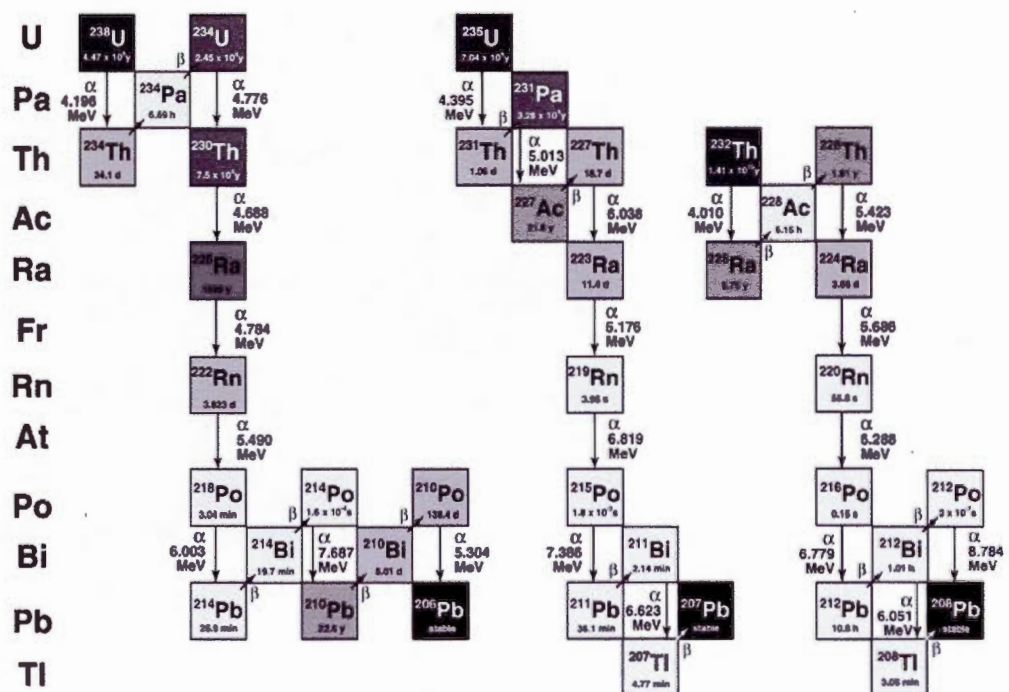


Figure 5 – Les trois chaînes de désintégration radioactive naturelles : ^{238}U , ^{235}U et ^{232}Th (Bourdon *et al.*, 2003).

CHAPITRE I

U- AND Th-SERIES ISOTOPES IN DEEP BAFFIN BAY SEDIMENTS: TRACERS OF DETRITAL SOURCES AND OF CONTRASTED GLACIAL/INTERGLACIAL SEDIMENTARY PROCESSES

Laurence Nuttin¹ and Claude Hillaire-Marcel¹

¹GEOTOP, Université du Québec à Montréal,
C.P. 8888, Succ. Centre-Ville, Montréal, QC, H3C 3P8, Canada

Keywords: Baffin Bay, marine sediments, U- and Th-series isotopes, ^{230}Th -excess, late Quaternary, last glacial cycle, detrital sources, sedimentary processes

Article soumis dans la revue scientifique Marine Geology.

Abstract

Uranium- (U) and thorium- (Th) series have been used to document the sedimentary sources, processes and fluxes of the last ~115 ka in central Baffin Bay, a major gateway between the Arctic Ocean and the North Atlantic Ocean, which has been fed throughout the last ice age by sediments and meltwaters from the northeastern Laurentide Ice Sheet, the Innuitian Ice Sheet and the western Greenland Ice Sheet. Measurements have been made with a ~1.6 ka time resolution in sedimentary core HU2008-029-016PC (70°27'N, 64°39'W; 2063 m water depth). The lack of correlation between U-concentration, $^{234}\text{U}/^{238}\text{U}$ activity ratio ($(^{234}\text{U}/^{238}\text{U})_{\text{AR}}$), organic carbon and redox sensitive elements suggests minimum early diagenetic U-uptake if any, likely due to very low organic matter sedimentary fluxes. Throughout the last glaciation, U- and Th-concentrations and mass ratio, as well as $(^{234}\text{U}/^{238}\text{U})_{\text{AR}}$, do not show either any unequivocal linkage with detrital dolomitic carbonate and/or detrital silicate fluxes. Data rather suggest sedimentary supplies with singular U- and Th-series signatures linked to specific glacial margin/ice streaming events. Large initial excesses in ^{230}Th ($(^{230}\text{Th}_{\text{xs}})_0$), well above the production from dissolved-U decay in the overlying water column, are observed throughout the last glacial interval in response to sediment focusing and high-sedimentation rates in the deepest part of the Bay. During this interval, high-frequency fluctuations in $(^{230}\text{Th}_{\text{xs}})_0$ indicate either a similar variability in sedimentation rates, not captured by the age model used, and/or grain size or mineralogical-dependent $^{230}\text{Th}_{\text{xs}}$ -scavenging rates. In the much lower sedimentation rate Holocene core-top section, the $(^{230}\text{Th}_{\text{xs}})_0$ -inventory falls below production in the overlying water column, despite evidence for some primary productivity revival as suggested by the higher organic carbon content. $^{230}\text{Th}_{\text{xs}}$ -losses through lateral advection via Baffin Bay water-masses overflowing through Davis Strait might account for this pattern, pointing to ocean circulation drastically differing from that of the glacial interval.

1.1 Introduction

Freshwater and sea ice exports from the Arctic Ocean have a strong impact on the North Atlantic oceanic circulation hence on the climatic system. Baffin Bay is one of the main communication pathways between the Arctic and the North Atlantic, notably through the Labrador Sea where water mass convections occur, contributing to the global oceanic circulation. During glacial periods, Baffin Bay constituted one of the major outlets of surrounding ice-sheets (the northeastern Laurentide Ice-Sheet, the Innuitian Ice-Sheet and the Greenland Ice-Sheet; Fig. 1). Glacial-time sedimentation rates in Baffin Bay have always been seen as highly-variable (Aksu and Piper, 1979; 1987; Aksu and Hiscott, 1989; Hiscott *et al.*, 1989). Sources, transport, depositional mechanisms and supply-rates of sedimentary particles were considerably shaped by instabilities along ice-sheet margins (Aksu and Piper, 1987; Parnell *et al.*, 2007; Simon *et al.*, 2014). The sediments from the glacial intervals encompass debris flow deposits and turbidites linked to meltwater pulses and surges along these glacier margins. In opposition, interglacial sediments consist of thin layers of hemipelagic material (Aksu and Piper, 1979; 1987).

Earlier paleoceanographic investigations in Baffin Bay (e.g., Aksu and Hiscott, 1989; Arthur *et al.*, 1989) were limited due to weakly-constrained chronological stratigraphic interpretations of late Pleistocene sequences. Firstly, the low primary productivity that prevailed during glacial intervals with a permanent sea ice cover (de Vernal *et al.*, 1987) resulted in scarce biogenic carbonates usable for the setting of ^{18}O -stratigraphies and unconstrained apparent ^{14}C -ages of carbonate ions in Baffin Bay paleo-waters. Secondly, low calcite saturation levels, at least during the present interglacial (e.g., Azetsu-Scott *et al.*, 2010), are responsible for the dissolution of biogenic carbonates (see also de Vernal *et al.*, 1992). Thirdly, local changes in sea ice/brine distillation processes in combination with variable fluxes and isotopic

compositions of continental meltwater (Hillaire-Marcel and de Vernal, 2008) hampered any stratigraphic interpretation of the very few $\delta^{18}\text{O}$ values obtained on scarce planktic foraminifers from deep Baffin Bay cores (Hillaire-Marcel *et al.*, 1989).

More recently, Simon *et al.* (2012) proposed a new chronostratigraphic framework covering the late Pleistocene based on magnetic paleointensity measurements in the very core used in this study (i.e., HU2008-029-016PC; ~7.4 m long; Figs. 1, 2). The core chronology (Fig. 2) was constructed through correlation of the relative paleointensity (RPI) profile with regional and global RPI reference curves. Average time incertitude for the ~22-75 ka interval is ~1.4 ka ($\pm 2\sigma$) while a larger incertitude of ~2.2 ka ($\pm 2\sigma$) has been proposed for the ~75-115 ka interval. Two geomagnetic excursions (i.e., the Laschamp and the Norwegian-Greenland Sea excursions) support the correlations. Moreover, measurements of ^{210}Pb performed on the trigger core (Steinhauer, 2012), the relative calcite percentages correlated to a nearby well-dated box core from Baffin Bay (core JCR175-BC06; from Andrews and Eberl, 2011) and three radiocarbon ages from the deglacial section (see Simon *et al.*, 2012 for details) complete the age model. Their study also indicated a mean sedimentation rate of ~6.5 cm.ka⁻¹ for the last ~115 ka but varying from less than ~3 cm.ka⁻¹ in the Holocene section up to ~67 cm.ka⁻¹ during the deglacial.

Here, we use the above chronostratigraphy to document U- and Th-series isotope behavior in the sediment, and confront sedimentary processes and sedimentation rates inferred from sedimentological and paleomagnetic data to information from these isotopes, especially from the excess- ^{230}Th ($^{230}\text{Th}_{\text{xs}}$; i.e., the ^{230}Th produced from the decay of ^{234}U in the water column). Ultimately, our objective is to retrieve information on sedimentary processes, particle sources (from U and Th data), and

their fluxes (from $^{230}\text{Th}_{\text{xs}}$ values), with inferences on ice-sheet and water mass instabilities relating to the last ~115 ka climatic fluctuations.

U- and Th-concentrations and isotopic ratios were determined at 16 to 8 cm intervals on bulk sediment samples, i.e., with a mean resolution of ~1 to 2 ka, based on the age-model of Simon *et al.* (2012; Fig. 2). Other data including grain size measurements, calcite *vs.* dolomite abundances, a few redox-sensitive element measurements (sulfur, manganese and iron), and organic carbon (C_{org}) contents, are used to complement information on particle sources, their transport mechanisms, and on geochemical and sedimentary processes of importance for the documenting of U- and Th-geochemistry in the sedimentary sequence (e.g., Henderson and Anderson, 2003). Further information on sedimentological features, paleomagnetic data and mineralogical abundances of the study sequence can be found in Simon *et al.* (2012; 2014) and in Simon (2013).

1.2 Regional Settings

Baffin Bay is a small subarctic ocean basin (~1400 km long, ~550 km wide and ~2300 m deep in its central plain) bordered by Baffin Island, the Canadian Arctic Archipelago and Greenland (Fig. 1; Tang *et al.*, 2004). The bathymetry of the bay is asymmetric, with a continental shelf exceeding 150 km off the western Greenland coast, and of less than 35 km off the eastern Baffin Island; the slopes from both parts are steep (Fig. 1; Aksu, 1983). Baffin Bay is connected to the Arctic Ocean through channels of the Canadian Arctic Archipelago, and to Labrador Sea through Davis Strait. Since around 9 cal ka BP, when Nares Strait opened (Fig. 1; England, 1999; England *et al.*, 2006; Jennings *et al.*, 2011), the retreat of continental ice in the Canadian Arctic permitted Arctic waters to be evacuated through the archipelago and the bay. This Arctic-North Atlantic connection through Baffin Bay radically impacted oceanographic conditions in the bay itself, as well as in the Labrador Sea, thus contributing to the progressive inception of the modern circulation system. Today the circulation in the bay is predominantly cyclonic. It is dominated by the northward-flowing Western Greenland Current, which is supplied by an inflow from the East Greenland Current, and by the southward-flowing Baffin Current, a large contributor to the Labrador Current (Tang *et al.*, 2004).

A particular feature of Baffin Bay sedimentary records is the abundance of detrital carbonate-rich layers. Quaternary glaciations led to the erosion of Paleozoic carbonates along northern Baffin Bay ice-margins (Fig. 1; Andrews *et al.*, 1998; Dyke *et al.*, 2002; Hulbe *et al.*, 2004). There, ice streaming and melting events led to the discharge of glacially-eroded detrital carbonates into the bay (Andrews *et al.*, 1998). They represent an important part of the total accumulated sediment. They contain more dolomite than calcite, in contrast with the carbonate layers observed in the Labrador Sea and the North Atlantic (Andrews, 1993; Andrews *et al.*, 1998). Ice

streaming was particularly active in Lancaster, Jones and Smith sounds, located at the northern part of the bay (Dyke *et al.*, 2002). Ice rafting, currents and slope sedimentological processes then spread these detrital carbonates throughout the central and eastern areas of the bay (Andrews and Eberl, 2011).

1.3 Materials and methods

The 741 cm-long sediment sequence HU2008-029-016PC (hereafter 016PC) was retrieved from a water depth of 2063 m in the abyssal plain of the central part of Baffin Bay (70°27'N, 64°39'W; Fig. 1; Campbell and de Vernal, 2009).

Wet bulk-density profiles were measured onboard by gamma ray attenuation using a GEOTEK™ Multisensor Core Logger with a cm-scale downcore resolution. Once split lengthwise, the sections were visually described for structure, texture and color (Campbell and de Vernal, 2009), then scanned at high resolution (~0.1-1 mm) using a computerized coaxial tomography (CAT-scan) technique to acquire 3D X-ray images (St-Onge and Long, 2009).

Grain size analyses were performed on ~1 g of bulk-sediment using a Beckman Coulter™ LS13320 laser diffraction grain size analyzer (see Simon *et al.*, 2012). Grain size distribution and statistical parameters were then calculated using the Gradistat™ software (Blott and Pye, 2001). Microgeochemical variations of iron (Fe), sulfur (S) and manganese (Mn) (in counts per second; cps) were determined by micro X-ray fluorescence (μ XRF) spectrometry on the u-channels sampled for magnetic property measurements, using an ITRAX™ core scanner equipped with a Mo-tube (Croudace *et al.*, 2006; Simon *et al.*, 2014). For each element, the number of counts acquired for a given depth interval was normalized by the total number of counts (in thousand counts per second; kcps). Qualitative and semi-quantitative ($\pm 1\sigma \approx 5\%$) analyses of mineralogical assemblages were made by Simon *et al.* (2014) through X-ray diffraction (XRD) following procedures described in Last (2001), Moore and Reynolds (1997) and Thorez (2003).

Total carbon- (C) content, inorganic carbon (C_{inorg}) and organic carbon (C_{org}) were analyzed on the bulk-fraction at 8 cm-intervals and reported in percentage vs dry sediment weight (dw%). Aliquots of ~9 mg were analyzed for their total C-content using an NC 2500TM elemental analyzer (Carlo-ErbaTM). Aliquots were then fumigated for ~24 hours with vapors of 12M HCl to dissolve the C_{inorg} and measure the residual C_{org} -content (Hélie, 2009). Values of C_{inorg} were finally estimated by subtracting the C_{org} values from the total C values. However, this dissolution procedure may have not removed all the fraction of the C_{inorg} (dolomite can be refractory to leaching) or might be slightly biased by the dissolution of other HCl-leachable compounds, both resulting in minor anomalies in C_{org} -estimations. An internal precision of 0.1% ($\pm 1\sigma$) was nonetheless estimated based on several analyses of Labrador Sea sediment samples from the analogue coulometer technique (see Fig. S2). Assuming that the C_{inorg} content are representative of calcite and dolomite abundances, estimates of their respective dry weight percentages within the sediment were calculated based on X-ray diffraction scans (Last, 2001; Moore and Reynolds, 1997; Thorez, 2003).

U and Th separation and extraction were performed following analytical procedures described in Lally (1992). Sampling was made at 8 cm intervals in the upper 424 cm of the sequence (i.e., the first ~65 cal ka BP; Simon *et al.*, 2012) and at 16 cm below (i.e., from ~65 to ~115 cal ka BP). Bulk-sediment sub-samples of about 1 g were heated at ~550°C for ~2 hours to eliminate organic matter and facilitate further treatments. A ^{232}U - ^{228}Th spike was added to the samples prior to a HCl/HNO₃/HF acid digestion. U and Th were isolated from other elements by ion exchange chromatography. A DowexTM AG1 X8 anion exchange resin was then used in combination with ultra-pure H₂O and 8M HCl, to separate U and Th respectively. Th was purified to remove any residual constituents, and U was separated from Fe, with a U/TEVA resin. Finally, U and Th were electrodeposited in monoatomic layers on

silver disks from which their activity was measured using an Ortec™ alpha counter (see Vallières, 1997 or Veiga-Pires, 1998 for a detailed description of the methodology). Analytical uncertainty based on counting statistics is better than 3% ($\pm 1\sigma$) for all isotopes. Note that all absolute concentrations, activity values, activity ratios and statistical compilations are reported hereafter with a $\pm 1\sigma$ standard deviation.

1.4 Results

1.4.1 Sedimentological features

As described by Simon *et al.* (2014), the sediment of 016PC is mostly composed of fine particles (Fig. 5). Silt (2 µm–63 µm) is the most important fraction and amounts to 48 ± 11 dw% (dry sediment weight percent; $\pm 1\sigma$) on an average, followed by the clay fraction (<2 µm) with a mean content of 29 ± 9 dw%, then by sand (63 µm–2 mm; 19 ± 12 dw%) and gravel (>2 mm; 3 $\pm 7\%$). The coarser fraction profiles, strongly influenced in such a setting by ice-rafting history, show relatively large variations (standard deviation $\approx 70\%$).

The C_{org}-content is low throughout the core with values varying between 0.1 and 0.7 dw% (Fig. 3). Moreover, values in the upper half of the sequence are slightly higher than in the bottom half. Three intervals dated respectively at ~37.9-34.9, ~11.9-10.85 and ≤ 0.6 cal ka BP, depict relatively higher C_{org} values. However, if the value from the core top sediment dated ≤ 0.6 cal ka BP likely represents true C_{org} concentrations relating to enhanced late Holocene biogenic production or to C_{org} preservation, those observed deeper downcore might be an analytical artifact due to incomplete dissolution of dolomite during sample treatment for C_{org} estimations (cf. material and methods; Figs. 3, 5). Carbonate contents (Fig. 5) indicate highly variable amounts of detrital dolomite in the glacial sediment (~0.5 to ~29 dw%), with a mean content of 14 ± 9 dw%, vs 5 ± 4 dw% of detrital calcite. The similarity of the dolomite and calcite abundance profiles indicates that the calcite essentially originates from terrigenous supplies (Fig. 5), i.e., it was also linked to the erosion of carbonate-rich bedrocks by glaciers, rather to synsedimentary biogenic production.

As illustrated (Fig. 3), Fe- and S-contents (in cps.kcps⁻¹; cf. material and methods) display nearly identical profiles, but differ from the Mn-content profile. Mn-contents do not vary much below the Holocene section, but then, increases abruptly.

1.4.2 U and Th isotopic data

Uranium concentration varies quite importantly downcore, between 0.93 ±0.02 and 2.61 ±0.04 µg.g⁻¹ (Fig. 4), with a major peak at ~44.2 cal ka BP. Thorium concentrations are relatively high throughout the sequence ($\geq 4.33 \pm 0.07 \mu\text{g.g}^{-1}$; Fig. 4). Three intervals yielded remarkably high Th-contents: 50.95 ±0.48 µg.g⁻¹ at ~71 cal ka BP, 31.28 ±0.28 µg.g⁻¹ at ~51.1 cal ka BP, and 35.74 ±0.33 µg.g⁻¹ at ~46.2 cal ka BP (U and Th measurements from these samples were duplicated). The (U/Th) mass ratio depicts relatively low values (compared to the mean crustal mass ratio equal to ~0.3) and large variations with respective minimum and maximum values of 0.03 ±0.001 and 0.25 ±0.01. Throughout the sequence, the sediment generally depicts a slight deficit in ^{234}U vs ^{238}U with a mean $^{234}\text{U}/^{238}\text{U}$ activity ratio ($(^{234}\text{U}/^{238}\text{U})_{\text{AR}}$) of 0.96 ±0.05. However, this activity ratio is relatively variable throughout the glacial section, varying between 0.83 ±0.02 and 1.11 ±0.03, values respectively observed at ~109 and ~71 cal ka BP (Fig. 3).

Estimated initial $^{230}\text{Th}_{\text{xs}}$ activities (see the *Supplementary information* section for details on calculations) are extremely variable (0.95 dpm.g⁻¹ on an average with a standard deviation of 0.94; Fig. 5). A few samples yielded relatively high values, especially in the Holocene section (up to 4.55 ±0.22 dpm.g⁻¹), and at ~71 cal ka BP (5.50 ±0.18 dpm.g⁻¹).

1.5 Discussion

1.5.1 Uranium flux and sedimentary processes

In marine sediments, uranium can have several origins. It is present in the terrigenous minerals, possibly in authigenic particles, and is also taken up through early diagenetic processes driving the diffusion of dissolved seawater U into the sediment. This diffusion is governed by redox gradients at the water/sediment interface (Gariépy *et al.*, 1994). The ($^{234}\text{U}/^{238}\text{U}$) activity ratio in seawater is 1.146 ± 0.002 (Cheng *et al.*, 2000). In the study core, U-concentration, ($^{234}\text{U}/^{238}\text{U}$)_{AR}, and concentrations of other redox-sensitive or redox-driven elements (Mn, S, and Fe) as well as those of organic carbon, are not correlated (Fig. 3). The lack of any robust correlation between these parameters points to negligible authigenic U-fluxes and minimum early diagenetic U-uptake, if any. The organic carbon content (0.3 ± 0.1 dw% on average; Fig. 3) observed in this core compares with that from glacial sequences of similar sedimentation rates in subarctic seas such as the Labrador Sea (e.g., Hillaire-Marcel *et al.*, 1994). They suggest low organic matter fluxes to the seafloor throughout the last glacial interval. A dense and long-lasting sea ice cover might have reduced biological productivity in subarctic basins, thus leading to low organic carbon and biogenic mineral fluxes to the seafloor (de Vernal *et al.*, 1987). Therefore, redox conditions did not permit significant secondary uranium uptake. Only a few intervals of the glacial section show slightly higher C_{org} (Fig. 3), but the peaks are not correlated with any of the geochemical parameters mentioned above. Even in the Holocene interval (<10.8 cal ka BP) while the organic carbon-content increases up to 0.6 ± 0.1 dw%, there is no clear evidence of secondary U-uptake (see Fig. 3). As a matter of fact, this section is represented by brown to dark brown silty-muds indicating oxidizing conditions (Fig. 2; Simon *et al.*, 2012). Uranium appears therefore to be essentially carried here by the detrital fraction of the sediment.

In layers where $(^{234}\text{U}/^{238}\text{U})_{\text{AR}}$ is lower than 1 (secular equilibrium), the sediment has undergone U losses with preferential departure of ^{234}U within the ~1 Ma time range of this disequilibrium. Similar deficits were also observed from an adjacent site (Ocean Drilling Program Leg 105, site 645; Causse and Hillaire-Marcel, 1989). Preferential mobilization of ^{234}U results from damages to mineral lattices induced by recoil during ^{238}U alpha-decay (Ku, 1966). The U losses may have occurred through (i) continental erosion, (ii) particle transport and/or (iii) late post-depositional diagenetic processes. Now, in such a sub-polar continental environment, minimum chemical erosion should produce particles with minimum alpha-recoil effects. The loss of U with preferential departure of ^{234}U during their subsequent transport and sedimentation is not documented in the literature. It was likely fast enough here to produce insignificant isotopic changes (adding to the relative coarseness of glacial sediments). Therefore, we hypothesize that late diagenetic processes are the most likely mechanism explaining such deficits in ^{234}U . Discrete redox gradients throughout the sediment sequence might have induced some post-depositional U-relocation with preferential ^{234}U -losses (e.g., Colley and Thomson, 1992; Colley *et al.*, 1989; Vallières, 1997). Such diagenetic processes would then explain the large excesses in ^{234}U observed at some intervals and the adjacent deficits. The maximum $\delta^{234}\text{U}$ offsets from secular equilibrium through such boundaries reach respectively -113 and +166‰ (Fig. 3). Relocation of fractionated U likely took place at the boundaries between oxidized layers and interbedded lower redox potential sediments (Fig. 3). Unfortunately, redox potential measurements needed to confirm this hypothesis are missing. Finally, we failed observing any systematic linkage between $(^{234}\text{U}/^{238}\text{U})_{\text{AR}}$ and the interstadial *vs* glacial marine isotopic stage intervals, neither any significant increase in the disequilibrium with time, in contrast to Vallières' observations (1997) in a core retrieved from the Greenland Rise, off Cape Farewell, in the of Labrador Sea. Nonetheless, one could not completely exclude others isotopic fractionation processes since fractionated uranium has been reported in Canadian

Arctic continental waters, peats and permafrost systems (e.g., Schirrmeister *et al.*, 2002), as well as in subglacial calcite concretions (e.g., Refsnider *et al.*, 2012).

1.5.2 Oxygenation conditions

As noted above, low organic matter fluxes to the seafloor prevailed during the past ~115 ka in Baffin Bay and even the core-top Holocene sediment indicates oxidized conditions. Worth of mention here is the Mn abundance profile that shows a low abundance flat pattern throughout the ~114.7-10.8 cal ka BP interval, followed by a sharp increase in the Holocene surficial sediment (Fig. 3). This particular trend highlights the existence of Mn-oxide minerals in this interval thus confirming an oxidized surficial sediment layer, as observed in the Arctic Ocean (e.g., Gobeil *et al.*, 2001; Löwemark *et al.*, in press). The layer dated within the ~10.8-9.97 cal ka BP interval (i.e., at about 20 cm below seafloor; Simon, 2013) has been seen as the Holocene boundary. It might mark the location of the oxic-suboxic modern boundary ($\text{MnO}_2/\text{Mn}^{2+}$ redox potential $\approx +500$ mV; Maynard, 2003). The well-defined peak in solid-phase Mn occurring near the sediment surface could result from two different processes. First, the Mn-rich horizon might result from the combination of surface oxic conditions with a diffusion of Mn^{2+} ions from a suboxic last glacial section (e.g., Maynard, 2003). Second, it could also indicate a higher Mn supply from enhanced fluxes from the circum Baffin Bay when sea level rose over continental shelves. Indeed, studies about Mn budgets in the Arctic Ocean (e.g., Macdonald and Gobeil, 2012; Löwemark *et al.*, in press; Jakobsson *et al.*, 2000) suggest that deglacial rises in sea level with shelf-submergence and glaciers melting might have controlled the Mn enrichments of interglacial Arctic Ocean sediments. By contrast, during glacial times, back-to-freezing conditions and sea level fall would have reduced Mn inputs (reduced riverine contributions and reduced shelf areas available for coastal erosion). However, in the Baffin Bay core, the Holocene sedimentation rates are by far the

lowest observed throughout the whole sequence ($<3.6 \text{ cm.ka}^{-1}$; Fig. 2; Simon *et al.*, 2012). The Mn profile is therefore possibly consistent with a mechanism of reductive dissolution, upward Mn^{2+} migration, and oxidative re-precipitation in the sediment surface layer. The specific Mn pattern observed here could thus point to some downward diffusion of oxygen into the sedimentary column.

1.5.3 Terrigenous supply

Previous authors (e.g., Aksu and Piper, 1987; Aksu and Hiscott, 1989; Andrews and Eberl, 2011; Hiscott *et al.*, 1989; Simon *et al.*, 2012; Simon *et al.*, 2014) have highlighted the exceptional high variability of detrital sediment supplies in Baffin Bay during the late Pleistocene. In such a low biogenic productivity environment, settling particles are mostly linked to erosion, transport and release of detrital particles by surrounding ice-sheets and the associated ice streams and ice margin melting processes. The coarser detrital dolomite-rich layers are linked to surges of northern Baffin Bay ice streams (e.g., Andrews and Eberl, 2011). Simon *et al.* (2013) attribute the high silty-clay interbedded layers to sedimentary supplies from the Greenland and/or Baffin Island ice margins. We assume that such layers were deprived of any significant early-diagenetic U (see discussion above). The U-Th data are thus mostly representative of changes in detrital sources throughout the $\sim 115 \text{ ka}$ interval. As already highlighted, U- and Th-concentrations (and their mass ratios) do not show any unequivocal linkages with detrital dolomitic carbonate fluxes *vs* detrital silicate material (Figs. 4, 5). Results hence suggest specific glacial margin events in the circum Baffin Bay, releasing sediment of singular U-Th signatures. Variations in U-Th data thus suggest variable and distinct mixings of terrigenous supplies. However, U-concentrations and ($^{238}\text{U}/^{232}\text{Th}$) mass ratios are also likely modified by late the diagenetic U-relocation processes evoked above.

The three peaks that depicted much higher ^{232}Th -concentration ($<31 \mu\text{g.g}^{-1}$; Fig. 4) match similarly peaking values reported in sediments from the nearby ODP site 645 (Causse and Hillaire-Marcel, 1989). Such high concentrations might have been carried by clays inherited from paleosoils and/or shales from surrounding lands (e.g., paleosoils developed over Precambrian metamorphic rocks outcropping in Greenland and Baffin Island; MacLean, 1985).

1.5.4 $^{230}\text{Th}_{\text{xs}}$ flux and evolution in deep-water circulation

The production rate of $^{230}\text{Th}_{\text{xs}}$ in the water column is nearly constant but for the ~3% change in U-concentration and salinity between glacials and interglacials (e.g., Schmidt and Spero, 2008; see also Not *et al.*, 2012). In the modern ocean, it amounts to $\sim 2.67 \cdot 10^{-5} \text{ dpm.cm}^{-3}.\text{ka}^{-1}$ (Suman and Bacon, 1989). Using this value, the theoretical $^{230}\text{Th}_{\text{xs}}$ vertical accumulation flux ($(F^{230}\text{Th}_{\text{xs}})_V$) calculated for the 2063 m water depth of 016PC site is $\sim 5.5 \text{ dpm.cm}^{-2}.\text{ka}^{-1}$ (see the *Supplementary information* section; Fig. 5). Within the above 3% uncertainty range and neglecting glacial/interglacial changes in sea level thus variations in the water depth at the site, this value thus represents the $^{230}\text{Th}_{\text{xs}}$ flux at the seafloor strictly linked to U-decay in the overlying water column. It has been used to estimate deviations of measured $(^{230}\text{Th}_{\text{xs}})_0$ fluxes in the sediment samples, i.e., $(F^{230}\text{Th}_{\text{xs}})_M$, and to compare the cumulative inventory of measured $(^{230}\text{Th}_{\text{xs}})_0$ in the sedimentary column, i.e., $\sum[(F^{230}\text{Th}_{\text{xs}})_M]$, to that of $(F^{230}\text{Th}_{\text{xs}})_V$, i.e., $\sum[(F^{230}\text{Th}_{\text{xs}})_V]$ (see the *Supplementary information* section for more details on calculations). Note that the overall uncertainty of initial $^{230}\text{Th}_{\text{xs}}$ estimates is better than $\pm 10\%$ as documented in the supplementary material section.

The large variations in the $(^{230}\text{Th}_{\text{xs}})_0$ are possibly linked to short-term, large amplitude changes in the sedimentation rate, which would not be captured in the age model,

and/or to grain size or mineralogical-dependent $^{230}\text{Th}_{\text{xs}}$ -scavenging rates. During the last glacial period, sediment focusing toward the central abyssal plain is evidenced by the sedimentary $^{230}\text{Th}_{\text{xs}}$ -values, well above the vertical production of this isotope in the overlying water column (i.e., $\sim 5.5 \text{ dpm.cm}^{-2}.\text{ka}^{-1}$; Figs. 5, 6). Only rare layers of this interval show fluxes below this vertical " $^{230}\text{Th}_{\text{xs}}$ -rain" component. The $^{230}\text{Th}_{\text{xs}}$ -inventory illustrated Fig. 6 suggests a $\sim 30\%$ excess over vertical $^{230}\text{Th}_{\text{xs}}$ production, on an average, for the $\sim 114.7\text{-}15$ cal ka BP time interval, thus indicating a net lateral input of sediment from the basin margins (Fig. 6). This area has been characterized by frequent turbidites and debris flows (Aksu and Piper, 1979; 1987; Aksu and Hiscott, 1989; Simon *et al.*, 2012). The subsequent settling of particles in the deep basin is likely to increase the $^{230}\text{Th}_{\text{xs}}$ -sediment inventory above the vertical $^{230}\text{Th}_{\text{xs}}$ production (e.g., François *et al.*, 2004). A detailed examination allows differentiating several intervals: $\sim 114.7\text{-}71$ and $\sim 40.1\text{-}15$ cal ka BP, which depict a very high excess in $^{230}\text{Th}_{\text{xs}}$ (with a ratio between the estimated $^{230}\text{Th}_{\text{xs}}$ flux and the vertical production exceeding 1.3), vs the $\sim 71\text{-}40.1$ cal ka BP interval, where it is slightly lower (Fig. 6). Higher ratios suggest enhanced sediment focusing whereas, the lower one points to reduced instabilities along Baffin Bay slopes. The interval between ~ 31.6 and ~ 15 cal ka BP yielded initial $^{230}\text{Th}_{\text{xs}}$ activities exceeding the last glacial mean value ($1.45 \pm 0.44 \text{ dpm.g}^{-1}$ vs $0.94 \pm 0.93 \text{ dpm.g}^{-1}$; Fig. 5). This corresponding layer is rich in clay-size lithogenic particles, which were related to the maximum extend and/or activity of the Uummannaq ice stream and margin (Fig. 2; Simon *et al.*, 2014). Assuming a relatively constant sedimentation rate throughout this interval (Simon *et al.*, 2012), a higher ^{230}Th scavenging efficiency of these clay-size particles might be evoked (Figs. 2, 5; Chase *et al.*, 2002). Above this layer, the $^{230}\text{Th}_{\text{xs}}$ inventory ratio decreases suggesting a progressive diminution in sediment focusing and/or grain-size coarsening (Fig. 6). Note that near the late glacial maximum stricto sensu, a layer of lower inventory ratio, thus of reduced sediment focusing (at ~ 21.7 cal ka BP; Fig. 6).

Very low initial $^{230}\text{Th}_{\text{xs}}$ activities, close to zero, are observed in the overlying section, from ~ 15 to ~ 10.8 cal ka BP, during the deglacial interval (Fig. 5). This episode is also associated with the coarser-grain particles and the highest sedimentation rates of the sequence (Figs. 2, 5; Simon *et al.*, 2014). Dilution of the $^{230}\text{Th}_{\text{xs}}$ signal by greater amounts of sinking material and/or coarser grain size, during ice retreat over surrounding lands (e.g., England, 1999; Jennings *et al.*, 2011; Knutz *et al.*, 2011; Ó Cofaigh *et al.*, 2013), might be seen as responsible for these low initial $^{230}\text{Th}_{\text{xs}}$. Significant amounts of terrigenous supplies of this interval consist of detrital dolomitic carbonates, presumably linked to iceberg calving from the ice streams of the northeastern Laurentide and southeastern Innuitian ice sheet margins (Andrews and Eberl, 2011; Simon, 2013). A $^{230}\text{Th}_{\text{xs}}$ -inventory ratio of ~ 1 , as illustrated Fig. 6, then marks the transition towards the Holocene interval.

The $(^{230}\text{Th}_{\text{xs}})_0$ of the Holocene core-top section (< 10.8 cal ka BP here) suggests a drastically distinct oceanographic regime (Figs. 5, 6). The low accumulation-rate Holocene sediments recorded sedimentary $^{230}\text{Th}_{\text{xs}}$ -fluxes below the vertical " ^{230}Th -rain". The inventory ratio of ~ 0.6 of this interval is consistent with a complete stop of sediment focusing in the deep central Baffin Bay seafloor (Figs. 5, 6). On the contrary, $^{230}\text{Th}_{\text{xs}}$ -advection outside the deep Baffin Bay through Davis Strait, likely occurred, as suggested by high $^{230}\text{Th}_{\text{xs}}$ values observed in the Holocene section of a cored raised SW of Davis Strait, in the western Labrador Sea (Nuttin *et al.*, in prep.). Nonetheless, the high $^{230}\text{Th}_{\text{xs}}$ absolute values of this interval, in a context of low but finer particle fluxes, might also relate to high Mn-oxide precipitation rates (Roy-Barman *et al.*, 2005).

1.6 Conclusion

Baffin Bay is an oceanic basin where sedimentation has been largely controlled by detrital inputs from surrounding glaciers during most of its recent geological past. Here, U and Th data spanning the last ~115 ka gave some insights into the uneven sedimentation rates and complex detrital inputs from the Innuitian, Greenland and Laurentide ice sheets, of the interval, until the inception of interglacial conditions some ~10.8 cal ka BP, led to much distinct sedimentary processes and currents.

The lack of correlation between U-concentration, $(^{234}\text{U}/^{238}\text{U})_{\text{AR}}$, organic carbon content and concentrations of redox-sensitive elements has been seen as an indication for reduced authigenic and early diagenetic U-fluxes, probably relating to low organic matter fluxes from a low productivity environment. Anomalies in $(^{234}\text{U}/^{238}\text{U})_{\text{AR}}$ led us to consider the occurrence of some late diagenetic U-mobility along discrete redox gradients in the sedimentary sequence. Moreover, U- and Th-concentrations and mass ratio are highly variable and, together with $(^{234}\text{U}/^{238}\text{U})_{\text{AR}}$, do not show any unequivocal linkage with detrital dolomitic carbonate fluxes or silicate material as one might have expected. Results thus suggested linkage with glacial margin events releasing material of singular U-Th signatures.

During the glacial period, surplus of supported ^{230}Th fluxes point toward sediment focusing in the deep Baffin Bay, in contrast with the Holocene interval, when it has been exported toward the Labrador Sea, through Davis Strait.

Acknowledgments

This study is part of the Canadian contribution to the Past4Future project. Funding from Ministère du Développement Économique, de l’Innovation et de l’Exportation (MDEIE), the Natural Sciences and Engineering Research Council of Canada (NSERC), The Fonds de la Recherche du Québec sur la Nature et les Technologies (FRQNT) and the Canadian Fondation for Innovation (CFI) is acknowledged. We owe special thanks to GEOTOP members, and especially to Bassam Ghaleb, for their help for U- and Th-series analyses and complementary measurements.

Supplementary information

The excess of ^{230}Th ($^{230}\text{Th}_{\text{xs}}$) generally relates to the fraction of ^{230}Th scavenged in the overlying water column (i.e., not supported by ^{234}U -decay in sediment). Assuming in first approximation that the sediment is deprived of any significant early-diagenetic uranium and that the $(^{234}\text{U}/^{238}\text{U})_{\text{AR}}$ of detrital particles are near secular equilibrium, the initial $^{230}\text{Th}_{\text{xs}}$ activities may be estimated using the following equation (Ivanovich *et al.*, 1992; Hillaire-Marcel, 2009):

$$(^{230}\text{Th})_0 = [^{230}\text{Th} - ^{234}\text{U}.((1-e^{(-\lambda_{230}).t})/(^{234}\text{U}/^{238}\text{U})) - (1-(^{234}\text{U}/^{238}\text{U}).(\lambda_{230}/(\lambda_{230}-\lambda_{234}))).(1-e^{(-\lambda_{230}-\lambda_{234}).t})]/e^{(-\lambda_{230}.t)}$$

where $(^{230}\text{Th})_0$ represents the initial ^{230}Th (dpm.g^{-1}), λ stands for the disintegration constants (time unit^{-1}), t is the time spanned since the deposition of the sediment (ka) estimated from the age model of Simon *et al.* (2012), and $(^{234}\text{U}/^{238}\text{U})$ represent the mean activity ratio measured on bulk-sediment (see Fig. S1). Assuming a low rate late diagenetic U-mobility (estimated here $\leq 6\%$ on an average for the glacial interval), the overall uncertainty on the estimated initial excesses in ^{230}Th should be better than 10%.

At the time scale of the processes investigated here, the loss in ^{238}U by decay is negligible. Therefore, one may postulate that $(^{238}\text{U})_0 \approx (^{238}\text{U})_t$. The ^{230}Th linked to detrital minerals is then estimated form the following equation (Ivanovich *et al.*, 1992):

$$(^{230}\text{Th}_{\text{detrital}})_0 \approx (^{234}\text{U}_{\text{detrital}})_0 = [(^{234}\text{U}/^{238}\text{U} - 1).e(\lambda_{234}.t)] + 1].(^{238}\text{U})_0$$

The $(^{230}\text{Th}_{\text{xs}})_0$, thus the ^{230}Th ensuing in principle from the decay of dissolved- ^{234}U , then scavenged in the water column by sinking particles, is then calculated by subtracting the ^{230}Th linked to detrital minerals from ^{230}Th -values (i.e., equations (1)-(2)). In this approach, ^{230}Th and ^{234}U in detrital minerals are considered in secular equilibrium with their parent isotopes. This assumption is acceptable when detrital sediments originate from physical erosion by glaciers, as generally observed in tills, but it is rarely valid when particles originate from chemical erosion in soils and more complex erosional processes (e.g., Vallières *et al.*, 1993).

The measured $(^{230}\text{Th}_{\text{xs}})_0$ fluxes in the sediment samples ($F^{230}\text{Th}_{\text{xs}})_M$, the inventory of measured $(^{230}\text{Th}_{\text{xs}})_0$ fluxes in the sediment column $\sum[(F^{230}\text{Th}_{\text{xs}})_M]$, and the inventory of vertical accumulation flux $\sum[(F^{230}\text{Th}_{\text{xs}})_V]$, might then evaluated as follows:

$$[(F^{230}\text{Th}_{\text{xs}})_M]_i = [(^{230}\text{Th}_{\text{xs}})_0]_i * \rho_i * SR_i$$

$$\sum[(F^{230}\text{Th}_{\text{xs}})_M] = \sum([(^{230}\text{Th}_{\text{xs}})_0]_i * \rho_i * SS_i)$$

$$(F^{230}\text{Th}_{\text{xs}})_V = 2063 * 0.00267 = 5.5 \text{ dpm.cm}^{-2}.\text{ka}^{-1}$$

$$\sum[(F^{230}\text{Th}_{\text{xs}})_M] = \sum([(F^{230}\text{Th}_{\text{xs}})_V] * t_i)$$

where SR is the sedimentation rate ($\text{cm}.\text{ka}^{-1}$), SS is the sediment sample thickness in cm, ρ_i is the density of the sediment (g of dry sediment. cm^{-3} of humid sediment), t is the age (ka), $\sum[(F^{230}\text{Th}_{\text{xs}})_M]$ and $\sum[(F^{230}\text{Th}_{\text{xs}})_V]$ the inventories of measured and theoretical initial excesses in $(^{230}\text{Th})_0$, respectively, for a given interval (i). Fluxes compared in this way allow to weight the $^{230}\text{Th}_{\text{xs}}$ vs variations in the sedimentation rate and, to a lesser extent, by changes in the bulk density of the sediment, whereas inventories provide immediate information on sedimentary processes responsible for

variations in $^{230}\text{Th}_{\text{xs}}$ accumulation rates (e.g., François *et al.*, 2004; Not and Hillaire-Marcel, 2010).

References

- Aksu, A. E. (1983), Short-period geomagnetic excursion recorded in Pleistocene sediments of Baffin Bay and Davis Strait., *Geological Society of America*, 11, 537-541.
- Aksu, A. E., and D. J. W. Piper (1979), Baffin Bay in the past 100,000 yr, *Geology*, 7, 245-248.
- Aksu, A. E., and D. J. W. Piper (1987), Late Quaternary sedimentation in Baffin Bay, *Canadian Journal of Earth Sciences*, 24, 1833-1846.
- Aksu, A. E., and R. N. Hiscott (1989), Slides and debris flows on the high-latitude continental slopes of Baffin Bay, *Geology*, 17, 885-888.
- Andrews, J. T. (1993), Changes in the silt- and clay-size mineralogy of sediments at Ocean Drilling Program site 645B, Baffin Bay, *Canadian Journal Earth Sciences*, 30, 2448-2452.
- Andrews, J. T., and D. D. Eberl (2011), Surface (sea floor) and near-surface (box cores) sediment mineralogy in Baffin Bay as a key to sediment provenance and ice sheet variations, *Canadian Journal Earth Sciences*, 48, 1307-1328.
- Andrews, J. T., M. E. Kirby, A. Aksu, D. C. Barber, and D. Meese (1998), Late Quaternary detrital carbonate (DC-) layers in Baffin Bay marine sediments (67°-74°N): correlation with Heinrich events in the North Atlantic?, *Quaternary Science Reviews*, 17, 1125-1137.
- Arthur, M. A., S. P. Srivastava, M. Kaminski, R. Jarrard, and J. Osier (1989), Seismic stratigraphy and history of deep circulation and sediment drift development in Baffin Bay and the Labrador Sea, in *Proceedings of the Ocean Drilling Program, Scientific Results*, 105: College Station, TX (Ocean Drilling Program), edited by S. P. Srivastava, M. Arthur and B. Clement, et al., pp. 957-988.
- Azetsu-Scott, K., A. Clarke, K. Falkner, J. Hamilton, P. Jones, C. Lee, B. Petrie, S. Prinsenberg, M. Starr, and P. Yeats (2010), Calcium carbonate saturation states in the waters of the Canadian Arctic Archipelago and the Labrador Sea, *Journal of Geophysical Research*, 115, C11021.

- Blott, S. J., and K. Pye (2001), GRADISTAT: a grain size distribution and statistics package for the analysis of unconsolidated sediments, *Earth Surf. Process. Landforms*, 26, 1237–1248.
- Campbell, D. C., and A. de Vernal (2009), Marine geology and paleoceanography of Baffin Bay and adjacent areas. Nain, NL to halifax, NS, August 28-September 23, 2008. Cruise report of CCGS Hudson Expedition 2008029, *Geological Survey of Canada*, Open File 5989, Natural Resources Canada, 2010 pages.
- Causse, C., and C. Hillaire-Marcel (1989), Thorium and uranium isotopes in upper Pleistocene sediments of ODP sites 645 (Baffin Bay), 646, and 647 (Labrador Sea), *Proceedings of the Ocean Drilling Program*, Scientific Results, 105, 551-560.
- Chase, Z., R. F. Anderson, M. Q. Fleisher, and K. P.W. (2002), The influence of particle composition and particle flux on scavenging of Th, Pa and Be in the ocean, *Earth and Planetary Science Letters*, 204, 215-229.
- Cheng, H., R. L. Edwards, J. Hoff, C. D. Gallup, D. A. Richards, and Y. Asmerom (2000), The half-lives of uranium-234 and thorium-230, *Chemical Geology*, 169, 17–33.
- Colley, S., and J. Thomson (1992), Behaviour and mobility of U series radionuclides in Madeira Abyssal Plain turbidites over the past 750,000 years, *Marine Geology*, 109, 141-158.
- Colley, S., J. Thomson, and J. Toole (1989), Uranium relocations and derivation of quasi-isochrons for a turbidite/pelagic sequence in the Northeast Atlantic, *Geochimica et Cosmochimica Acta*, 53, 1223-1234.
- Croudace, I. W., A. Rindby, and R. G. Rothwell (2006), ITRAX: description and evaluation of a new multi-function X-ray core scanner, *Geological Society*, 267(1), 51-63.
- de Vernal, A., C. Hillaire-Marcel, A. Aksu, and J. P. Mudie (1987), Palynostratigraphy and chronostratigraphy of Baffin Bay deep sea cores: Climatostratigraphic implications, *Palaeogeography, Palaeoclimatology, Palaeoecology*, 61, 97-105.
- de Vernal, A., G. Bilodeau, C. Hillaire-Marcel, and N. Kassou (1992), Quantitative assessment of carbonate dissolution in marine sediments from foraminifer linings vs. shell ratios: example from Davis Strait, NW North Atlantic, *Geology*, 20, 527–530.

- Dyke, A. S., J. T. Andrews, P. U. Clark, J. H. England, G. H. Miller, J. Shawe, and J. J. Veillette (2002), The Laurentide and Innuitian ice sheets during the Last Glacial Maximum, *Quaternary Science Reviews*, 21, 9-31.
- England, J. (1999), Coalescent Greenland and Innuitian ice during the Last Glacial Maximum: revising the Quaternary of the Canadian High Arctic, *Quaternary Science Reviews*, 18 421-456.
- England, J., N. Atkinson, J. Bednarski, A. S. Dyke, D. A. Hodgson, and C. Ó Cofaigh (2006), The Innuitian Ice Sheet: configuration, dynamics and chronology, *Quaternary Science Reviews*, 25, 689–703.
- François, R., M. Frank, M. M. Rutgers van der Loeff, and M. P. Bacon (2004), ^{230}Th normalisation: An essential tool for interpreting sedimentary fluxes during the late Quaternary, *Paleogeography*, 19(1).
- Gariépy, C., B. Ghaleb, C. Hillaire-Marcel, A. Mucci, and S. Vallières (1994), Early diagenetic processes in Labrador Sea sediments: uranium-isotope geochemistry, *Canadian Journal of Earth Sciences*, 31(1), 28-37.
- Gobeil, C., B. Sundby, R. W. MacDonald, and J. N. Smith (2001), Recent change in organic carbon flux to Arctic Ocean deep basins: Evidence from acid volatile sulfide, manganese and rhenium discord in sediments, *Geophysical Research Letters*, 28(9), 1743-1746.
- Hélie, J.-F. (2009), Elemental and stable isotopic approaches for studying the organic and 627 inorganic carbon components in natural samples. In Deep-Sea to Coastal Zones: Methods Techniques for Studying Paleoenvironments, *IOP Conference Series: Earth and Environmental Science*, 5, 012006.
- Henderson, G. M., and R. F. Anderson (2003), The U-series Toolbox for Paleoceanography, *Mineralogical Society of America*, 52(1), 493-531.
- Hillaire-Marcel, C. (2009), The U-series dating of (biogenic) carbonates, *IOP Conference Series: Earth and Environmental Science*, 5(1), 012008.
- Hillaire-Marcel, C., and A. de Vernal (2008), Stable isotope clue to episodic sea ice formation in the glacial North Atlantic, *Earth and Planetary Science Letters*, 268, 143-150.
- Hillaire-Marcel, C., A. de Vernal, A. E. Aksu, and S. Macko (1989), High-resolution isotopic and micropaleontological studies of upper Pleistocene sediments at ODP Site

645, Baffin Bay, *Proceedings of the Ocean Drilling Program, Scientific Results*, 105, 599–616.

Hillaire-Marcel, C., A. de Vernal, M. Lucotte, A. Mucci, G. Bilodeau, A. Rochon, S. Vallières, and G. Wu (1994), Productivité et flux de carbone dans la mer du Labrador au cours des derniers 40 000 ans, *Canadian Journal Earth Sciences*, 31(1), 139-158.

Hiscott, R. N., A. E. Aksu, and O. B. Nielsen (1989), Provenance and dispersal patterns, Pliocene-Pleistocene section at site 645, Baffin Bay, *Proceedings of the Ocean Drilling Program, Scientific Results*, 105, 31-52.

Hulbe, C. L., D. R. MacAyeal, G. H. Denton, J. Kleman, and T. V. Lowell (2004), Catastrophic ice shelf breakup as the source of Heinrich event icebergs, *Paleoceanography*, 19, PA1004.

Ivanovich, M., A. G. Latham, and T.-L. Ku (1992), Uranium-series disequilibrium applications in geochronology, in *Uranium-series Disequilibrium: applications to earth, marine and environmental sciences*, edited by M. Ivanovich and R. S. Harmon, Oxford science publications.

Jakobsson, M., R. Løvlie, H. Al-Hanbali, E. Arnold, J. Backman, and M. Mörté (2000), Manganese and color cycles in Arctic Ocean sediments constrain Pleisocene chronology, *Geology*, 28(1), 23-26.

Jennings, A. E., C. Sheldon, T. M. Cronin, P. Francus, J. Stoner, and J. T. Andrews (2011), The Holocene history of Nares Strait: Transition from glacial bay to Arctic-Atlantic throughflow, *Oceanography*, 24, 26-41.

Knutz, P. C., M.-A. Sicre, H. Ebbesen, S. Christiansen, and A. Kuijpers (2011), Multiple-stage deglacial retreat of the southern Greenland Ice Sheet linked with Irminger Current warm water transport, *Paleoceanography*, 26, 1-18.

Ku, T.-L. (1966), *Uranium-series disequilibrium in deep sea sediments*, 157 pp, Columbia University, New York.

Lally, A. E. (1992), Chemical procedures, in *Uranium series disequilibrium: Applications to Earth, Marine, and Environmental Sciences*, edited by M. Ivanovich and R. S. Harmon, pp. 95-126, Clarendon Press, Oxford.

Last, W. M. (2001), Mineralogy analysis of lake sediments, in *Tracking Environmental Change Using Lake Sediments*, edited by W. M. Last and J. P. Smol, pp. 143-187, Kluwer Academic Publishers, Dordrecht, The Netherlands.

Löwemark, I., C. März, M. O'regan, and R. Gyllenkreutz (in press), Arctic Ocean Mn-stratigraphy: synthesis and interbasin comparison, *Quaternary Science Reviews*.

Macdonald, R. W., and C. Gobeil (2012), Manganese sources and sinks in the Arctic Ocean with reference to periodic enrichments in basin sediments, *Aquatic Geochemistry*, 18, 565–591.

MacLean, B. (1985), Geology of the Baffin Island Shelf, in Quaternary Environments: Eastern Canadian Arctic, Baffin Bay and Western Greenland, edited by J. T. Andrews, pp. 154-177, Allen and Unwin, Boston.

Maynard, J. B. (2003), Manganiferous sediments, rocks, and ores, in Sediments, Diagenesis, and Sedimentary Rocks: Treatise on Geochemistry, edited by F. T. Mackenzie, pp. 289-308, Elsevier-Pergamon, Oxford.

Moore, D. M., and J. C. Reynolds (1997), X-Ray Diffraction and the Identification and Analysis of Clay Minerals, Oxford University Press, New York.

Not, C., and C. Hillaire-Marcel (2010), Time constraints from ^{230}Th and ^{231}Pa data in late Quaternary, low sedimentation rate sequences from the Arctic Ocean : an example from the northern Mendeleev Ridge, *Quaternary Science Reviews*, 29(25-26), 3665–3675.

Not, C., K. Brown, B. Ghaleb, and C. Hillaire-Marcel (2012), Conservative behavior of uranium vs. salinity in Arctic sea ice and brine, *Marine Chemistry*, 130-131, 33–39.

Nuttin, L., J. Maccali, and C. Hillaire-Marcel (in prep.), U, Th and Pa insights into sedimentological and paleoceanographic changes off Hudson Strait (Labrador Sea) during the last ~37 ka with special attention to methodological issues.

Ó Cofaigh, C., J. A. Dowdeswell, A. E. Jennings, K. A. Hogan, A. Kilfeather, J. F. Hiemstra, R. Noormets, J. Evans, D. J. McCarthy, J. T. Andrews, J. M. Lloyd, and M. Moros (2013), An extensive and dynamic ice sheet on the West Greenland shelf during the last glacial cycle, *Geology*, 41(2), 219–222.

Parnell, J., S. Bowden, J. T. Andrews, and C. Taylor (2007), Biomarker determination as a provenance tool for detrital carbonate events (Heinrich events?): Fingerprinting Quaternary glacial sources into Baffin Bay, *Earth and Planetary Science Letters*, 257 71–82.

Refsnider, K. A., G. H. Miller, C. Hillaire-Marcel, M. L. Fogel, B. Ghaleb, and R. Bowden (2012), Subglacial carbonates constrain basal conditions and oxygen isotopic

composition of the Laurentide Ice Sheet over Arctic Canada, *Geology*, 40(2), 135–138.

Roy-Barman, M., C. Jeandel, M. Souhaut, M. Rutgers van der Loeff, I. Voege, Leblond, N., and R. Freydier (2005), The influence of particle composition on thorium scavenging in the NE Atlantic ocean (POMME experiment), *Earth and Planetary Science Letters*, 240, 681–693.

Schmidt, M. W., and H. J. Spero (2008), North Altantic salinity oscillations linked to changes in atmospheric and ocean circulation over the last glacial cycle, *PAGES News*, 16(1), 23-25.

Simon, Q. (2013), Propriétés magnétiques, minéralogiques et sédimentologiques des sédiments profonds de la baie de Baffin: Chronologie et dynamique des glaciers ouest groenlandais, innuitiens et laurentidiens au cours de la dernière glaciation, 163 pp, Université du Québec à Montréal, Montréal (QC), Canada.

Simon, Q., G. St-Onge, and C. Hillaire-Marcel (2012), Late Quaternary chronostratigraphic framework of deep Baffin Bay glaciomarine sediments from high-resolution paleomagnetic data, *Geochemistry, Geophysics, Geosystems*, 13, 1–24.

Simon, Q., C. Hillaire-Marcel, G. St-Onge., and J. T. Andrews (2014), North-eastern Laurentide, western Greenland and southern Innuitian ice stream dynamics during the last glacial cycle, *Journal of Quaternary Science*, 29, 14-26.

St-Onge, G., and B. F. Long (2009), CAT-scan analysis of sedimentary sequences: an ultrahigh-resolution paleoclimatic tool, *Engineering Geology*, 103, 127–133.

Steinhauer, S. (2012), Postglacial paleoceanography of central Baffin Bay from palynological tracers, Université du Québec à Montréal, Montréal.

Suman, D. O., and M. P. Bacon (1989), Variations in Holocene sedimentation in the North American Basin determined from ^{230}Th measurements, *Deep Sea Research Part A. Oceanographic Research Papers*, 36, 869-878.

Tang, C. C. L., C. K. Ross, T. Yao, B. Petrie, B. M. DeTracey, and E. Dunlap (2004), The circulation, water masses and sea-ice of Baffin Bay, *Progress in Oceanography*, 63, 183–228.

Thorez, J. (2003), L'argile, minéral pluriel, *Bulletin de la Société Royale des Sciences de Liège*, 72, 19-70.

Vallières, S. (1997), Flux d'uranium et excès de 230Th dans les sédiments de la Mer du Labrador - Relation avec les conditions paléocéanographiques et la paléoproduction du bassin, 144 pp, Université du Québec à Montréal, Montréal (QC), Canada.

Vallières, S., C. Hillaire-Marcel, and B. Ghaleb (1993), Disequilibrium of U-Th in overburden deposits in the St. Lawrence Lowlands, Quebec, *Canadian Journal Earth Sciences*, 30(8), 1730-1740.

Veiga-Pires, C. C. (1998), Flux de thorium-230 et flux sédimentaires dans l'Atlantique du Nord Ouest au cours des derniers 40 ka en relation avec les variations du climat, environment sciences thesis, 169 pp, Université du Québec à Montréal, Montréal.

Figures

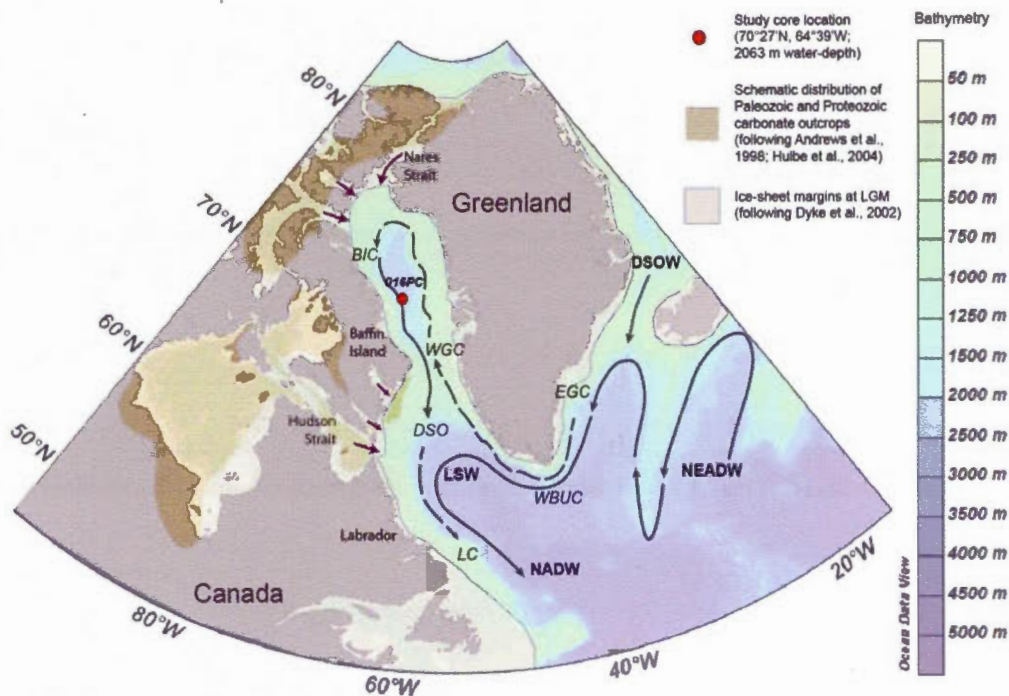


Figure 1 – Location map of core HU2008-029-016PC in Baffin Bay representing: bathymetry of the region, ice-sheets extension at Last Glacial Maximum, carbonate outcrops with their major outlets toward ocean (purple arrows) and a schematic illustration of the major components of the Atlantic Meridional Overturning Circulation (AMOC) in the region with present-day deep (solid lines) and intermediate (dashed lines) oceanic currents and water masses (WGC – Western Greenland Current; BIC – Baffin Island Current; DSO – Davis Strait Overflow; LC – Labrador Current; EGC – East Greenland Current; WBUC – Western Boundary Undercurrent; NEADW – Northeast Atlantic Deep Water; LSW – Labrador Sea Water; DSOW – Denmark Strait Overflow Water; NADW – North Atlantic Deep Water).

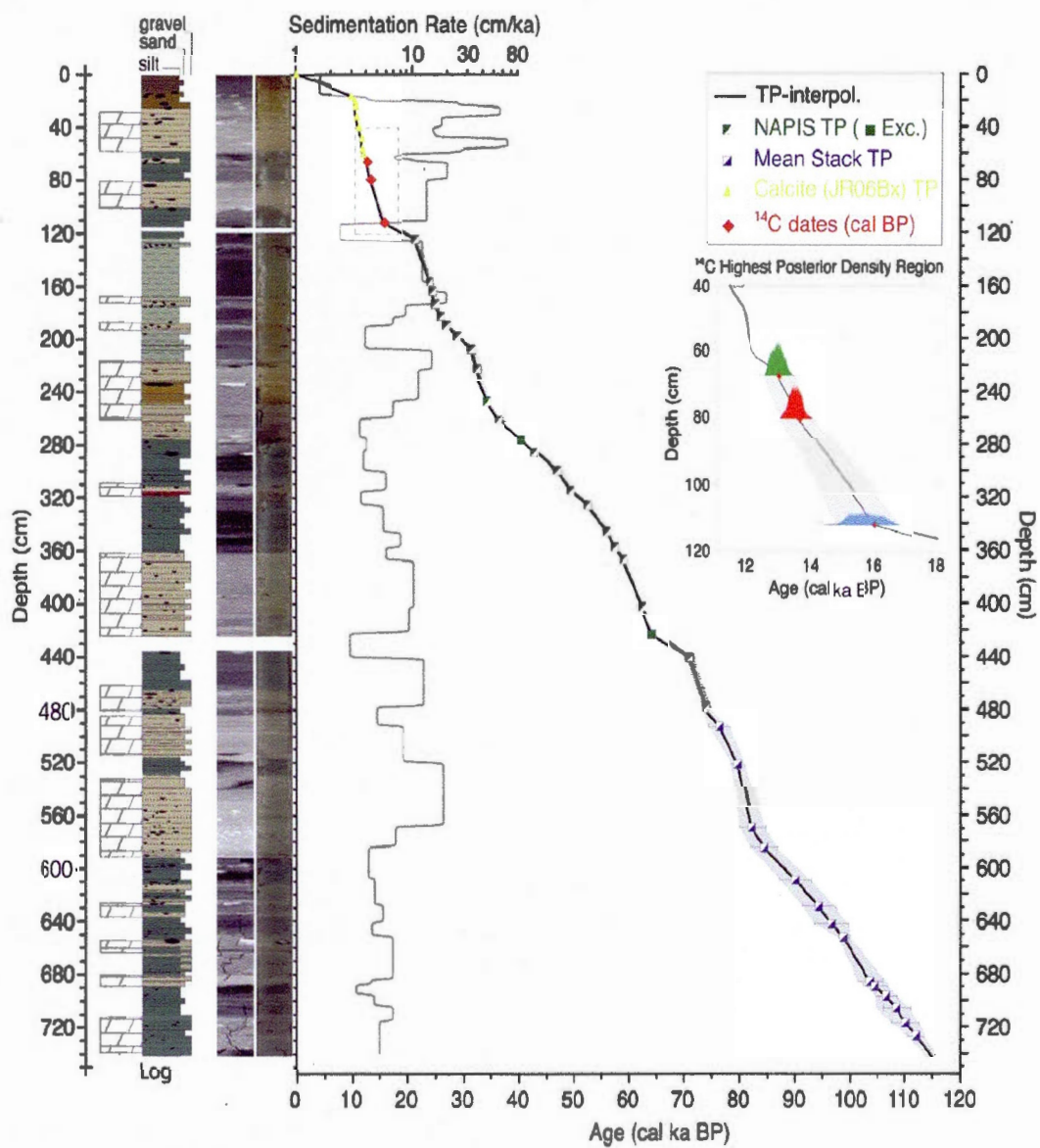


Figure 2 – Age-depth model of core HU2008-029-016PC based on magnetic paleointensity measurements and on calibrated radiocarbon data plotted with lithology log, CAT-scan image and photographs profile (from Simon *et al.*, 2012; see text for more explanations).

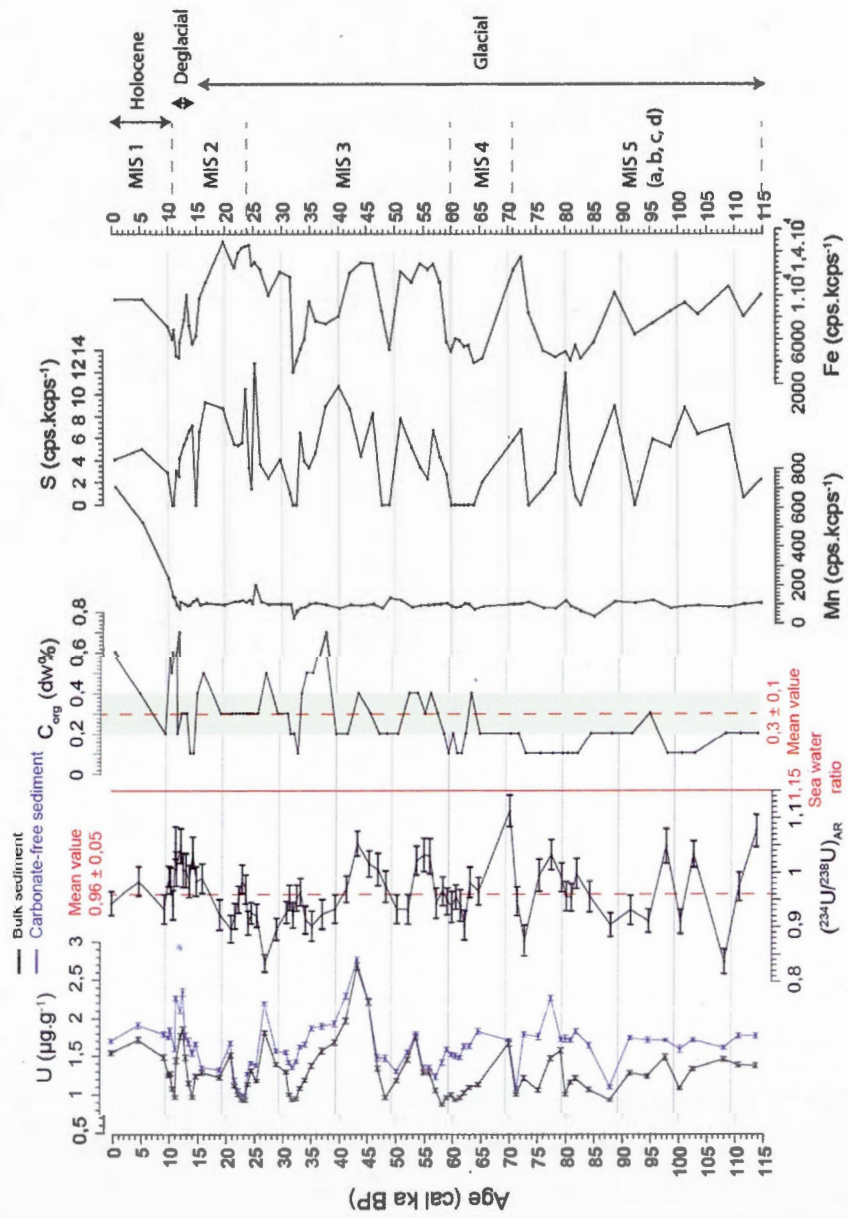


Figure 3 – Geochemical properties and isotopic ratios vs age. From left to right: U-concentration ($\mu\text{g}\cdot\text{g}^{-1}$); $^{234}\text{U}/^{238}\text{U}$ activity ratio; C_{org} (dry sediment weight %); redox-sensitive elements (Mn, S and Fe) from μXRF measurements. Data points are plotted with a $\pm 1\sigma$ analytical uncertainty.

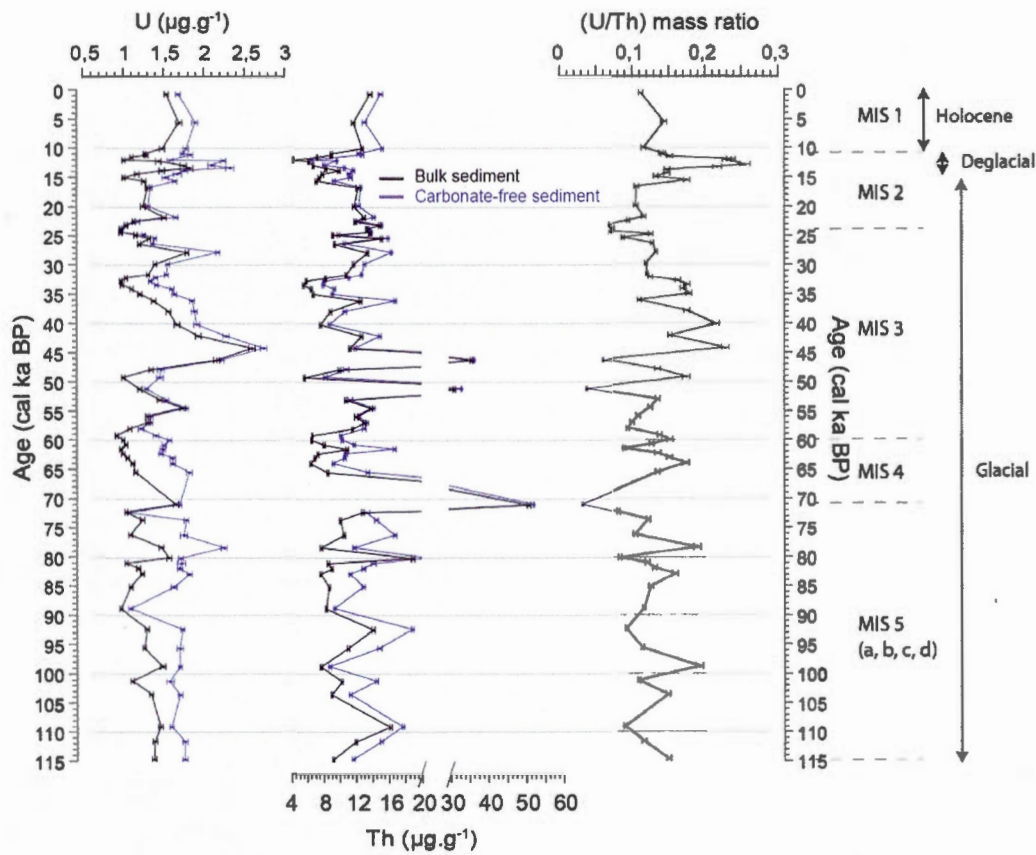


Figure 4 – U and Th data in the study sequence vs age. From left to right: U- and Th-concentrations of bulk and carbonate-free sediment ($\mu\text{g.g}^{-1}$); U/Th mass ratio. The dataset is plotted with a $\pm 1\sigma$ analytical uncertainty. As the carbonate content is highly variable in the sequence, the concentrations of U and Th were converted in carbonate-free sediment as follows:

$$U_{\text{carbonate-free sediment}} = (U * 100) / (100 - \text{dw\%CaCO}_3);$$

$$Th_{\text{carbonate-free sediment}} = (Th * 100) / (100 - \text{dw\%CaCO}_3)$$

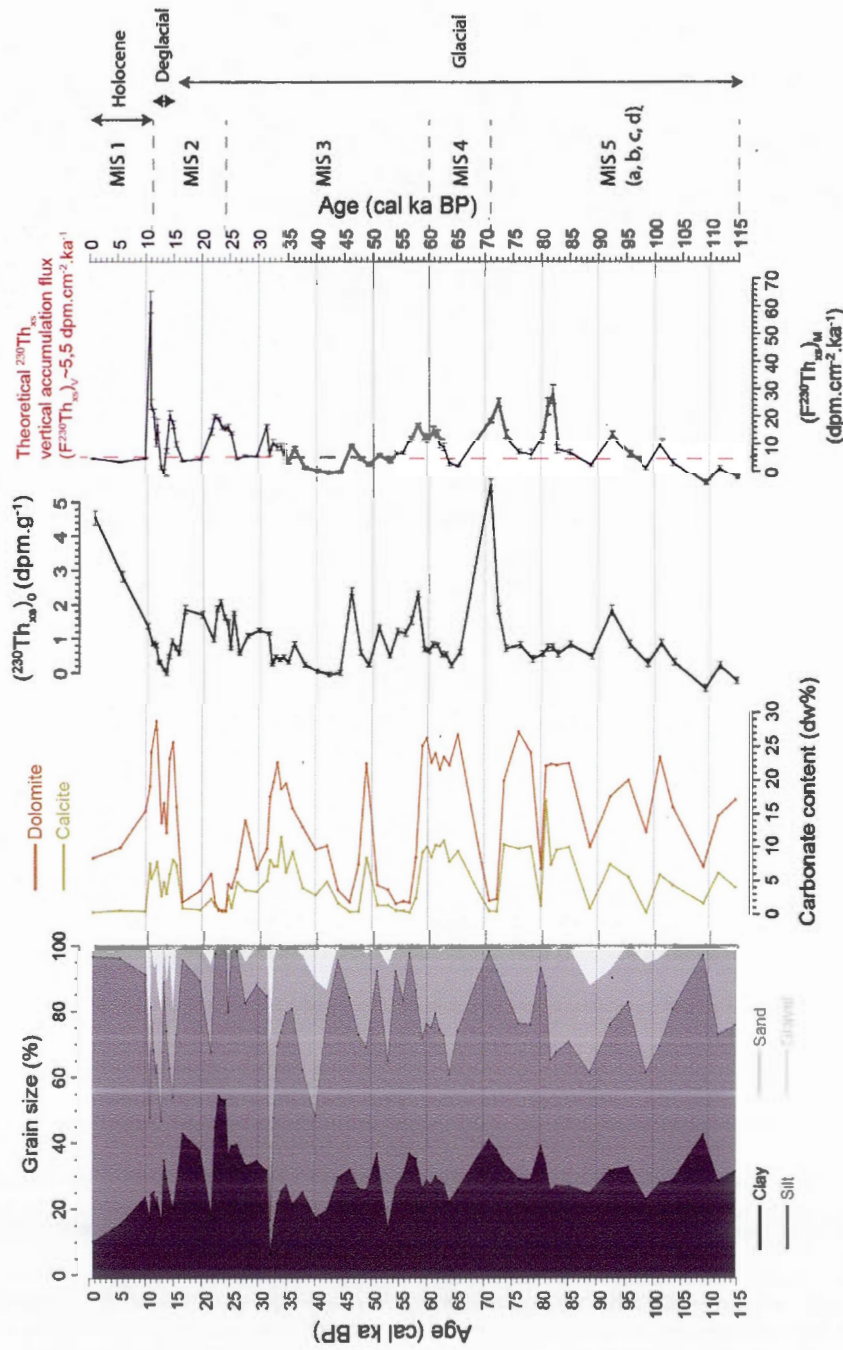


Figure 5 – Sedimentological, mineralogical and geochemical properties plotted vs age with initial excess of ^{230}Th ($(^{230}\text{Th}_{\text{xs}})_0$). From left to right: grain size (clay, silt, sand and gravel fractions in relative abundance) from Simon *et al.* (2012); calcite and dolomite contents (dry sediment weight %); $(^{230}\text{Th}_{\text{xs}})_0$ (dpm.g $^{-1}$); measured $(^{230}\text{Th}_{\text{xs}})_0$ flux ($(F^{230}\text{Th}_{\text{xs}})_0$) in $\text{dpm.cm}^{-2}\text{ka}^{-1}$ plotted against the vertical $^{230}\text{Th}_{\text{xs}}$ production rate from the overlying water column ($(F^{230}\text{Th}_{\text{xs}})_w$, dashed red line). Data points are plotted with a $\pm 1\sigma$ analytical uncertainty.

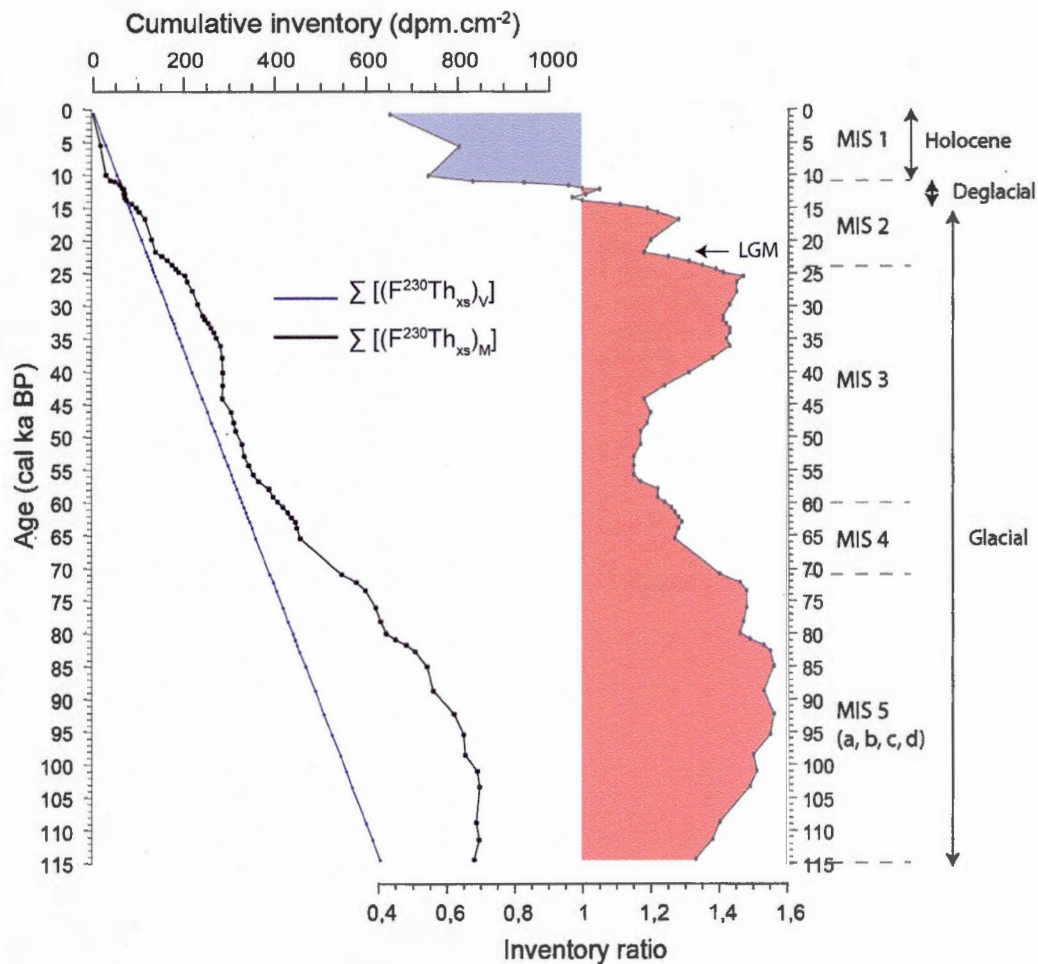


Figure 6 – The inventory of $(F^{230}\text{Th}_{xs})_M$ in the sediment column ($\sum[(F^{230}\text{Th}_{xs})_M]$; dpm.cm⁻²), and the inventory of vertical accumulation flux ($\sum[(F^{230}\text{Th}_{xs})_V]$; dpm.cm⁻²) vs age (on the left); inventory ratio (on the right) showing surplus (red) vs deficit (blue) of measured above expected supply of $^{230}\text{Th}_{xs}$.

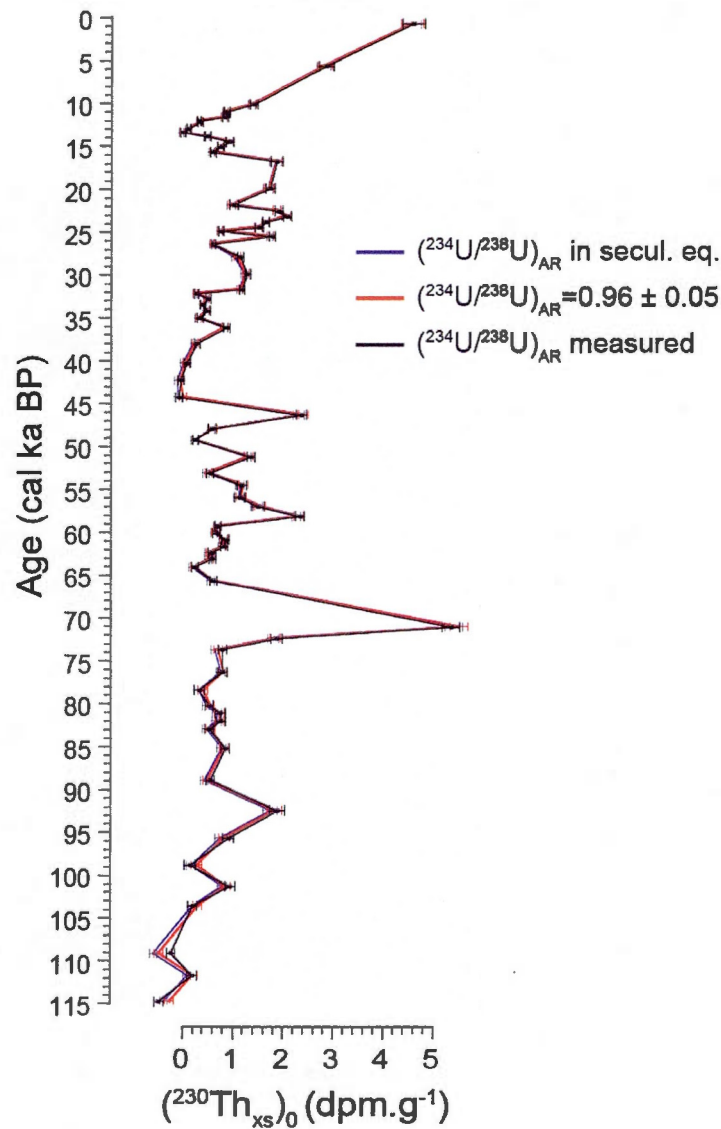


Figure 7 – $(^{230}\text{Th}_{\text{xs}})_0$ activity (dpm.g^{-1} ; $\pm 1\sigma$) plotted vs age following: (1) actual $(^{234}\text{U}/^{238}\text{U})_{\text{AR}}$ (black); (2) secular equilibrium (blue); (3) mean of $(^{234}\text{U}/^{238}\text{U})_{\text{AR}}$ obtained on the entire record (i.e., 0.96 ± 0.05) (red). The dataset is plotted with a $\pm 1\sigma$ analytical uncertainty.

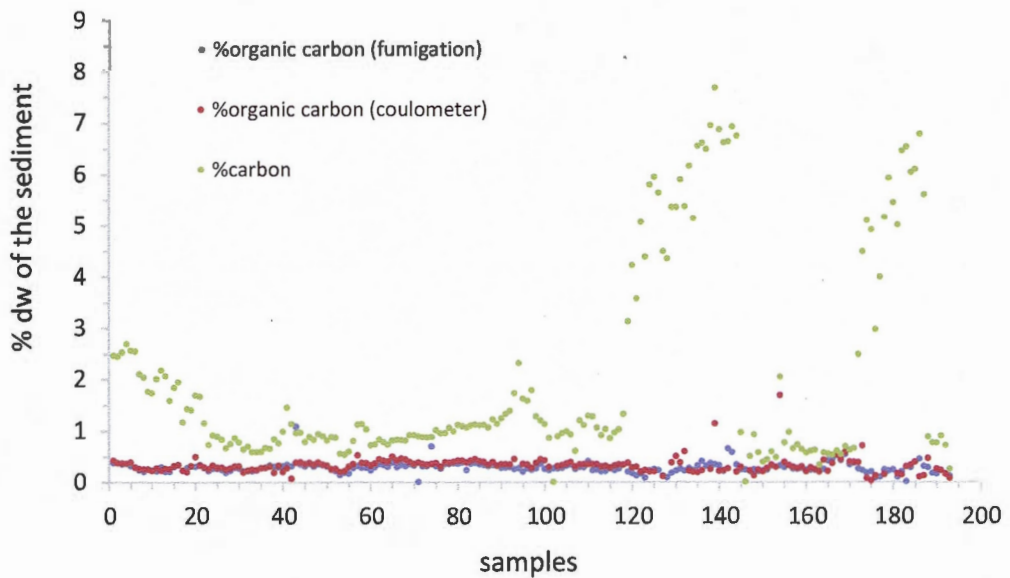


Figure 8 – Fraction in dry weight bulk sediment (dw%) of total carbon and organic carbon measured by both fumigation and coulometer techniques (see text for explanations).

CHAPITRE II

U, Th AND Pa INSIGHTS INTO SEDIMENTOLOGICAL AND PALEOCEANOGRAPHIC CHANGES OFF HUDSON STRAIT (LABRADOR SEA) DURING THE LAST ~37 KA WITH SPECIAL ATTENTION TO METHODOLOGICAL ISSUES

Laurence Nuttin¹, Jenny Maccali¹ and Claude Hillaire-Marcel¹

¹GEOTOP, Université du Québec à Montréal,
C.P. 8888, Succ. Centre-Ville, Montréal, QC, H3C 3P8, Canada

Keywords: Labrador Sea, marine sediments, U- and Th-series isotopes, paleoceanography, late Quaternary, Laurentide Ice Sheet, Hudson Strait, Heinrich events, sedimentary processes, ²³¹Pa and ²³⁰Th excess calculation

Article soumis dans la revue scientifique Quaternary Science Reviews.

Abstract

A ~9m-long sediment core spanning the last ~37 ka has been raised from the lower Labrador continental slope, off the Hudson Strait shelf edge. It has been analyzed for its U, Th and Pa isotope contents, along with current sedimentological parameters, as a means to retrieve information about sedimentological changes in response to northeastern Laurentide Ice Sheet (LIS) margin instabilities. The sequence yielded a high-resolution record of subglacial detrital carbonate pulses from Hudson Strait assigned to "Heinrich events" H2 and H1, whereas H0 was missing. Large variations in bulk sediment U- and Th-contents as well as in $^{234}\text{U}/^{238}\text{U}$ activity ratio are observed throughout the sequence, leading to large uncertainties when calculating excesses in ^{231}Pa and ^{230}Th ($^{231}\text{Pa}_{\text{xs}}$ and $^{230}\text{Th}_{\text{xs}}$) over their supported and in-growth fractions (i.e., inherited from detrital minerals and produced from authigenic and diagenetic U-uptake). In particular, ^{234}U excesses or deficits vs ^{238}U (-115‰ < $\delta^{234}\text{U}$ < +126‰) are observed throughout the sequence, suggesting occasional U-uptake from the water column and/or some late diagenetic mobility along discrete redox gradients, despite the overall low and little variable organic carbon content (0.3 ± 0.1%) observed. The above uncertainties in $^{231}\text{Pa}_{\text{xs}}$ and $^{230}\text{Th}_{\text{xs}}$ estimates and the large variability in geochemical and sedimentary fluxes off the northeastern LIS margin, lead us to downgrade the potential paleoceanographic information yielded by these isotopes in such a setting. Nonetheless, the H2 and H1 layers are highlighted by very low initial excesses in both $^{230}\text{Th}_{\text{xs}}$ and $^{231}\text{Pa}_{\text{xs}}$, indicating their extremely fast deposition. Throughout most of the sedimentary sequence, the calculated initial $^{230}\text{Th}_{\text{xs}}$ fluxes are nearly in balance with ^{230}Th production in the overlying water column. Exceptions are the H2 layer, an interval succeeding H1, and the post-glacial sediment. The estimated initial ($^{231}\text{Pa}_{\text{xs}}/^{230}\text{Th}_{\text{xs}}$) ratios are generally lower than their production rate in the water column (i.e., 0.092), indicating nearly continuous preferential export of $^{231}\text{Pa}_{\text{xs}}$ over the last ~37 cal ka BP, thus the persistence of some deep currents throughout the interval.

2.1 Introduction

Deep-water convection in subarctic seas is a key component of the North Atlantic climate system as it regulates ventilation and heat-exchange rates with the atmosphere (e.g., Broecker, 1991). In this respect, the Labrador Sea constitutes a transitional basin between the Arctic and the North Atlantic. Freshwater fluxes, either from the Arctic Ocean or from surrounding ice sheets, notably the Laurentide Ice Sheet (LIS), have tightly controlled convection in this basin (Labrador Sea Water - LSW; Lazier, 1973; Hillaire-Marcel *et al.*, 2001). Major melting events from the northeastern LIS margin have been associated with abrupt climate/ocean instabilities, in particular most of the millennial-scale Heinrich (H) events which resulted in the deposition of recognizable layers throughout the North Atlantic sea floor, based on their sedimentological and geochemical specific features (Hemming, 2004, Rashid *et al.*, 2012, and references herein). Sedimentary processes and fluxes in the Labrador Sea have accordingly undergone significant changes, essentially driven by the sporadic release of large amounts of terrigenous material from the LIS (e.g., Andrews *et al.*, 1994), and/or through changes in the oceanographic regime (e.g., Wu and Hillaire-Marcel, 1994), as well as due to variations in primary productivity (e.g., Hillaire-Marcel *et al.*, 1994b).

Here, based principally on measurement of isotopes of uranium (^{234}U , ^{238}U), thorium (^{230}Th , ^{232}Th) and protactinium (^{231}Pa) in a ~9 m-long core (HU08-029-004PC) raised from the lower continental slope off the Hudson Strait outlet, we intend to document changes in terrigenous fluxes and sedimentary dynamics off the northeastern LIS meltwater route during the last ~37 cal ka BP. Initial excesses in ^{230}Th and ^{231}Pa [$(^{230}\text{Th}_{\text{xs}})_0$ and $(^{231}\text{Pa}_{\text{xs}})_0$], i.e., the fractions of these isotopes unsupported by parent isotopes in the sediment at the time of their deposition, have been estimated using a calibrated ^{14}C -chronology of the sedimentary sequence (Gibb *et al.*, 2014) to carry back in time ^{230}Th and ^{231}Pa activities, and calculate their post-depositional in situ

production (e.g., Anderson *et al.*, 1990; Veiga-Pires and Hillaire-Marcel, 1999). U-, Th- and Pa-concentrations and activity ratios were measured with a centennial to millennial resolution due to the highly variable sedimentation rates at the site (Gibb *et al.*, 2014). In order to link U, Th and Pa isotopes and sediment properties, CAT-scan images have been used to document sedimentological features and complemented by measurements of the coarse fraction content (used as proxy for IRD abundance), of organic and inorganic carbon concentrations (C_{org} and C_{inorg}), and semi-quantitative mineralogical analyses of the bulk sediment. Based on micropaleontological data and transfer function reconstruction of paleo-sea surface conditions, Gibb *et al.* (2014) identified three distinct climatostratigraphic intervals: a glacial interval when productivity was practically nil (~36.6-12.2 cal ka BP), a deglacial interval characterized by low salinity conditions due to the transit of huge amounts of meltwater (~12.2-8.3 cal ka BP) and the post-glacial, when productivity rose rapidly to full interglacial values ($\leq \sim 8.3$ cal ka BP). Gibb *et al.* (2014) highlighted the fact that if the site did record major meltwater pulses linked to H3 (?), H2, H1 and the final drainage of Lake Agassiz, it did not record the Younger Dryas nor the H0 event (see Andrews *et al.*, 1994, Hillaire-Marcel *et al.*, 1994a, Pearce *et al.*, 2013, for information on the H0 event in the Labrador Sea). Building on Gibb and others' work (2014), we intend to further document here detrital sediment sources and fluxes as well as sedimentary processes, in the western most area of Labrador Sea, based on U- and Th-series isotopes. In a context of continental slope processes and at the emplacement of the LIS margin, these tracers could provide information about the past ice-sheet dynamics as well as about the variability of deep currents (e.g., Veiga-Pires and Hillaire-Marcel, 1999; Yu *et al.*, 1996).

2.2 Materials and methods

The 895 cm-long core HU08-029-004PC (henceforth 004PC) was retrieved from a water depth of 2674 m on the lower Labrador continental slope, approximately 180 km seaward from the Hudson Strait shelf edge (61°27'N, 58°2'W; Fig. 1; Campbell and de Vernal, 2009).

2.2.1. Sedimentological parameters

Once core sections were split lengthwise, the sediment was visually examined for its structure, texture and color. Sections were then scanned at high resolution (~0.1-1 mm) by computerized coaxial tomography (CAT-scan) technique to acquire 3D X-rays images (St-Onge and Long, 2009). CAT-scan gives a view on the internal structure of the sediment cores, especially specific features such as IRD. Core sections were also photographed at 500 dpi (dots per inch) using a high resolution Smartcube™ Smart Camera Image Scanner (SmartCIS).

Qualitative and semi-quantitative ($\pm 1\sigma \approx 5\%$) analyses of mineralogical assemblages were made using X-ray diffraction (XRD) following procedures described in Last (2001), Moore and Reynolds (1997) and Thorez (2003). A homogeneous powder of the < 63 μm bulk fraction was scanned using a Siemens D5000™ diffractometer, with a CoK α 1, 2 X-radiations ($\lambda=1.76896$) and a Si detector, between 2° and 50° 2 θ angles. Qualitative and semi-quantitative estimates were based on peak identifications and relative intensity measurements of their X-ray patterns using the Diffracplus EVA™ software.

Total carbon- (C) content, inorganic carbon (C_{inorg}) and organic carbon (C_{org}) were analyzed on the bulk-fraction at 8 cm-intervals and reported in percentage vs dry sediment weight (dw%; Fig. S3). Aliquots of ~9 mg were analyzed for their total C-

content using an NC 2500TM elemental analyzer (Carlo-ErbaTM). Aliquots were then fumigated for ~24 hours with vapors of 12M HCl to dissolve carbonate minerals and measure the residual C_{org}-content (Hélie, 2009). Values of C_{inorg} were finally estimated by subtracting the C_{org} values from the total C values. However, this dissolution procedure may have not removed all the fraction of the C_{inorg} (dolomite can be partly refractory to acid treatment) or might be slightly biased by the dissolution of HCl-leachable compounds, both resulting in minor anomalies in C_{org}-estimations. An internal precision of 0.1% ($\pm 1\sigma$) was nonetheless estimated based on duplicated analyses from the analogue coulometer technique (see Fig. S3). Assuming that the C_{inorg} content is representative of calcite and dolomite abundances (based on X-ray diffraction scans; Last, 2001; Moore and Reynolds, 1997; Thorez, 2003), estimates of their respective dry weight percentages within the sediment were calculated.

The core chronology was established by Gibb *et al.* (2014) and constrained by radiocarbon (¹⁴C) dates obtained from hand-picked planktic foraminifera *Neogloboquadrina pachyderma* sinistral from the dw% > 106 µm sediment fraction (Fig. 2). Accelerator mass spectrometry (AMS) measurements were made at the Lawrence Livermore National Laboratory and at the National Ocean Sciences AMS Facility. Radiocarbon ages were calculated using the Libby half-life of 5568 years and normalized to a δ¹³C-value of -25‰. A marine reservoir correction of 400 years was applied ($\Delta R=0$; see a discussion in the supplementary material of Hillaire-Marcel *et al.*, 2007), and the ages were converted to calibrated years using Oxcal 4.2 (Ramsey, 2008) and the Marine09 calibration curve (Reimer *et al.*, 2009). The *p-sequence* model in OxCal was selected for estimating the probability of each age. This model is based on a Bayesian approach taking into account the probability distribution of calibrated ages, the sample depths and changes in deposition rates (see Gibb *et al.*, 2014, for more details). Three ¹⁴C ages depict in particular an age interval of 8441–8179 cal ka BP for the 85–36 cm layer, with an average value of 8327 cal ka

BP, deposited during the final drainage of Lake Agassiz (e.g., Lewis *et al.*, 2012; Barber *et al.*, 1999; Hillaire-Marcel *et al.*, 2007), although the sediment does not show here a significant increase in detrital carbonates in contrary to what is generally observed (e.g., Hillaire-Marcel *et al.*, 2007; Nicholl *et al.*, 2012). Linear interpolation between each modelled age were used to calculate the sedimentation rates and the age-depth relationship, which was finally used to plot proxy data against age as well as to carry back in time radioactive disequilibria in the U-series isotopes. The modeled results provide a basal age of ~36.6 cal ka BP. Sedimentation rate is hence ~24.4 cm/ka on average but depicts large variations downcore (see Fig. 2).

2.2.2. Radionuclide analyses

Several techniques were combined for the measurement of actinides. ^{238}U , ^{234}U , ^{232}Th and ^{230}Th separation and extraction were performed following analytical procedures described in Lally (1992). Sampling was made at 12 cm intervals from bottom up to a depth of 140 cm depth downcore, then at 8 cm to 4 cm intervals, above, where sedimentation rate revealed much lower based on the calibrated ^{14}C -chronology. Samples from the upper 40 cm interval were measured by Thermal Ionization Mass Spectrometry (TIMS; VG-SectorTM single collector) whereas below, dowcore, they were measured by alpha-emission spectrometry (using OrtecTM alpha counter).

For ^{238}U , ^{234}U , ^{230}Th and ^{232}Th measurements, bulk sediment aliquots of ~0.2 g (TIMS) and ~1 g (alpha counting) were heated at ~550°C for ~2 hours to oxide organic matter and facilitate further treatments. A ^{233}U - ^{236}U - ^{229}Th (TIMS) or ^{232}U - ^{228}Th (alpha counter) spike was added to the samples prior to $\text{HNO}_3/\text{HF}/\text{HCl}$ acid digestion. U and Th were then isolated from other constituents by ion exchange chromatography using resin columns. A Dowex AG1 X8 200-400 mesh anion exchange resin was used in combination with ultra-pure H_2O and 8M HCl to separate U and Th. Th was then purified to remove any residual constituents, and U was

separated from Fe with a U/TEVA resin. Finally, for alpha counting, U and Th were electrodeposited as monoatomic layers on silver disks from which their activity was measured using an Ortec™ alpha counter (see Vallières, 1997 or Veiga-Pires, 1998 for a detailed description of the methodology) or directly measured by TIMS. The analytical uncertainty is better than 3% ($\pm 1\sigma$) for all isotopes (^{238}U , ^{234}U , ^{232}Th and ^{230}Th) with the alpha counting measurements, and better than 0.5% ($\pm 1\sigma$), with TIMS measurements.

A total of 46 sediment samples of ~0.5 g distributed throughout the sequence were also analyzed for their ^{231}Pa vs ^{230}Th concentrations. Prior to $\text{HNO}_3/\text{HF}/\text{HCl}/\text{HClO}_4$ acid digestions (as above), known amount of ^{233}Pa , ^{236}U and ^{229}Th spikes were added to the samples. Isotopes were extracted from the sediment samples by anion exchange chromatography with the Dowex AG1 X8 200-400 mesh resin following analytical procedures in Choi *et al.* (2001). ^{231}Pa and ^{230}Th were measured on a multi-collector inductively coupled plasma mass spectrometer (MC-ICP-MS; Nu IITM instrument), respectively by peak jumping at masses 231 and 233, and at masses 229 and 230, on a filtered ion counter. The filter allows to significantly reduced tailing from ^{232}Th which is particularly important for ^{230}Th measurements as ^{232}Th is much more abundant than ^{230}Th . Monitoring ^{232}Th tailing at mass 230.5 allowed us to estimate that the tailing contribution from ^{232}Th was actually smaller than the uncertainty on ^{230}Th measurements and was hence considered negligible. Mass fractionation was monitored on the $^{238}\text{U}/^{235}\text{U}$ ratio from an intern solution of HU-1. Certified reference material NBL-117, U500 and U010 were analyzed daily for their $^{238}\text{U}/^{235}\text{U}$ ratio and corrected for fractionation using an exponential law. Corrections using the intern HU-1 solution gave deviations from the certified values less than 2%. Internal errors for Pa measurements were less than 1% except for samples with relatively low concentrations where the error could be as high as 2-4%. Internal errors for Th measurements were less than 1%. Blanks were under 2 fg and 260 fg for Pa and Th, respectively. Reproducibility uncertainty is ~6.1% for ^{231}Pa and ~3% for ^{230}Th (both

in $\pm 1\sigma$) calculated from replicate measurements of an internal sedimentary standard (see Fig. S1).

2.3 Results

Note that all sample values and statistical means are reported hereafter with a $\pm 1\sigma$ uncertainty.

2.3.1 Sedimentological features

The sediments are predominantly composed of gray silty clays (Figs. 2, 3; Campbell and de Vernal, 2009; Gibb *et al.*, 2014). CAT-scan images reveal dispersed gravels of millimetric and centimetric dimensions (i.e., IRD) inside the fine matrix (Fig. 2). These are observed throughout the sequence except in the uppermost ~150 cm (i.e., the last ~11 cal ka BP; Figs. 2, 3; see Gibb *et al.*, 2014). Moreover, two thick intervals depict brown color and fine laminated structures of sand-size particles and with higher IRD concentrations.

The organic carbon content of the sedimentary sequence is generally low (0.3 ± 0.1 dw% on average; Fig. 4), and compares with other Labrador Sea sequences with similar sedimentation rates (e.g., Hillaire-Marcel *et al.*, 1994b). Except rare intervals, most values fall within the internal analytical uncertainty of $\pm 0.1\%$ (see *material and methods*).

The dw% $> 106 \mu\text{m}$ size fraction, considered here as proxy of IRD-content, varies significantly (Fig. 4; see Gibb *et al.*, 2014). The highest values, reaching up to 65 dw%, are observed from core bottom up to the layer dated ~33.7 cal ka BP, as well as within the ~25.2-24.4 cal ka BP and the ~17.8-15.7 cal ka BP intervals. They are also abundant but to a lesser extent (maximum dw% $> 106 \mu\text{m}$ size fraction value of ~7.5 dw%) at ~14.5-14.3 cal ka BP and ~12.9-11.4 cal ka BP. Data strongly fluctuate in an irregular sawtooth shape inside these intervals indicating alternation of fine and coarse material deposition.

Semi-quantitative analyses ($\pm 1\sigma \approx 5\%$) of mineralogical abundances revealed four main constituents (Fig. 3). The most abundant mineral is quartz, with a mean content of $37 \pm 9.3\%$. The feldspar group is the second most abundant, with alkaline-feldspars reaching $20.5 \pm 8.1\%$ on average, and potassium-feldspars, $5 \pm 3\%$ on average. Carbonates hold the next position with $15.8 \pm 14.2\%$ and $7.9 \pm 5.4\%$ on average, respectively for calcite and dolomite (note their high standard deviations with dispersion higher than 70%). Pyroxene is only significantly present, averaging $6.6 \pm 1\%$, within two intervals: ~ 34 to ~ 25.5 cal ka BP and ~ 24.2 to ~ 17.9 cal ka BP. Other trace minerals (with a total abundance $\leq 5\%$) include: micas, amphiboles, kaolinite/chlorite and smectite/chlorite clay groups. They do not show significant evolution since their variations are within the estimated analytical uncertainty. Nonetheless, a significant peak in mica is observed in the layer assigned to the final drainage of the Lake Agassiz (at ~ 8.3 cal ka BP; Gibb *et al.*, 2014).

The total carbonate content ranges between 0 and ~ 61.2 dw% (Fig. 4). Calcite and dolomite abundances vary similarly, except in the top 100 cm-section ($< \sim 9.7$ cal ka BP), where biogenic carbonate production resulted in high calcite sedimentary fluxes (see Hillaire-Marcel *et al.*, 1994c). Dolomite abundance is almost nonexistent within this interval whereas calcite increases rapidly from ~ 2 dw% background signal up to ~ 21 dw% (the calcite/dolomite ratio reaches up to ~ 19.3 at ~ 3.85 cal ka BP). Dowcore, two very well defined intervals depict high total carbonate abundances with up to ~ 49.5 dw% of calcite and ~ 22.6 dw% of dolomite (Fig. 4). The first peak is dated between ~ 25.2 and ~ 24.3 cal ka BP (760-700 cm depth) and the second one, between ~ 17.8 and ~ 15.7 cal ka BP (588-488 cm depth), both presenting an abrupt increase directly followed by a more progressive decrease suggesting some bioturbation at their top (Fig. 3). These correspond to the Heinrich layers H2 and H1 (see *discussion* below). The detrital carbonate profile also shows high values (up to ~ 26 dw% in total carbonate content) at core bottom ($\geq \sim 33.7$ cal ka BP; i.e., 860 cm depth; see Fig. 3), as well as between ~ 14.5 to ~ 14.3 cal ka BP, both intervals

associated with higher coarse fraction contents (i.e., fraction $> 106 \mu\text{m}$ dw%) – as evoked above. Moreover, visual lithological examinations of the bottom part of the core reveal a sediment layer composed of massive gray sand. The highest values in the $> 106 \mu\text{m}$ size fraction (i.e., up to $\sim 65\%$) are recorded in this very layer (Fig. 4).

The sediments are predominantly composed of gray silty clays (Figs. 2, 3; Campbell and de Vernal, 2009; Gibb *et al.*, 2014). CAT-scan images reveal dispersed gravels of millimetric and centimetric dimensions (i.e., IRD) inside the fine matrix (Fig. 2). These are observed throughout the sequence except in the uppermost ~ 150 cm (i.e., the last ~ 11 cal ka BP; Figs. 2, 3; see Gibb *et al.*, 2014). Moreover, two thick intervals depict brown color and fine laminated structures of sand-size particles and with higher IRD concentrations.

Downcore the organic carbon content is generally low, with 0.3 ± 0.1 dw% on average (Fig. 4), and compares with other sequences from Labrador Sea of similar sedimentation rates (e.g., Hillaire-Marcel *et al.*, 1994b). Except rare intervals, most of the values are contained within the internal analytical uncertainty estimated to $\sim 0.1\%$ (see *material and methods*).

The dw% $>106 \mu\text{m}$ size fraction, considered here as proxy of IRD-content, varies significantly downcore (Fig. 4; see Gibb *et al.*, 2014). The highest values, reaching up to 65 dw%, are present at the bottom of the core to ~ 33.7 cal ka BP, in the ~ 25.2 - 24.4 cal ka BP and the ~ 17.8 - 15.7 cal ka BP intervals. They are also significantly abundant but in a lesser extent (maximum dw% $>106 \mu\text{m}$ size fraction value of ~ 7.5 dw%) at ~ 14.5 - 14.3 cal ka BP and ~ 12.9 - 11.4 cal ka BP. Data strongly fluctuate in an irregular sawtooth shape inside these intervals indicating an alternation between fine and coarse material.

Semi-quantitative analyses ($\pm 1\sigma \approx 5\%$) of mineralogical abundances indicate that the sediment is composed by four main assemblages (Fig. 3). The most abundant is the quartz with a mean of $37 \pm 9.3\%$. The feldspar group is the second most abundant group, containing the alkaline-feldspars with $20.5 \pm 8.1\%$ on average and the potassium-feldspars, much less abundant, with $5 \pm 3\%$ on average. Carbonates hold the next position with $15.8 \pm 14.2\%$ and $7.9 \pm 5.4\%$ on average, respectively for calcite and dolomite (note their high standard deviations with dispersion higher than 70%). Pyroxene is only present at two sections from ~ 34 to ~ 25.5 cal ka BP and from ~ 24.2 to ~ 17.9 cal ka BP with a relatively high average of $6.6 \pm 1\%$. Other trace minerals ($\leq 5\%$: mica, amphibole, the kaolinite/chlorite and smectite/chlorite clay groups) do not show significant evolution since variations are contained in the error bars – they nevertheless evolve in opposite phase with detrital carbonate profiles as for quartz and feldspars. Only a significant peak in mica is observed in the layer assigned to the final drainage of the Lake Agassiz (at ~ 8.3 cal ka BP; Gibb *et al.*, 2014).

Estimated in dry weight percent of the sediment from inorganic carbon content (see *material and methods*), the total carbonate content ranges between 0 and ~ 61.2 dw% downcore (Fig. 4). Calcite and dolomite abundance profiles vary similarly throughout the sequence except in the last upper one hundred centimeters ($<\sim 9.7$ cal ka BP). Dolomite abundance is almost nonexistent within this interval whereas calcite increases rapidly from ~ 2 dw% background signal up to ~ 21 dw% (the calcite/dolomite ratio reaches up to ~ 19.3 at ~ 3.85 cal ka BP). Two very well defined intervals contain high carbonate abundances, up to ~ 49.5 dw% for calcite and ~ 22.6 dw% for dolomite (Fig. 4). The first peak spreads between ~ 25.2 and ~ 24.3 cal ka BP (760-700 cm depth) and the second one between ~ 17.8 and ~ 15.7 cal ka BP (588-488 cm depth), both presenting an abrupt increase directly followed by a more progressive decrease (Fig. 3). These correspond to the well-known Heinrich layers H2 and H1 (see *discussion* below). The detrital carbonate profile also shows high values (up to ~ 26 dw% in total carbonate content) at the beginning of the record until ~ 33.7 cal ka BP (i.e., 860 cm

depth; see Fig. 3) and a little peak between ~14.5 to ~14.3 cal ka BP, both associated with higher dw%>106 µm values – as evoked above. Moreover, visual lithological examinations of the bottom part of the core reveal a sediment layer composed of massive gray sand. The highest values in dw%>106 µm size fraction (i.e., up to ~65%) are recorded in this interval (Fig. 4).

2.3.2 Radionuclide data

Downcore bulk sediment U concentrations vary from $0.71 \pm 0.004 \text{ } \mu\text{g.g}^{-1}$ to $2.23 \pm 0.01 \text{ } \mu\text{g.g}^{-1}$ and show generally high values throughout the glacial and deglacial intervals (Fig. 5). Afterwards, the values decrease progressively (except for a peak at ~12.2 cal ka BP), with minimum values recorded in the uppermost 8 cm. Bulk sediment Th-concentrations also fluctuate considerably, between $2.86 \pm 0.06 \text{ } \mu\text{g.g}^{-1}$ and $9.14 \pm 0.18 \text{ } \mu\text{g.g}^{-1}$, with a similar decreasing trend through time (Fig. 5). Note that both U- and Th-concentrations are low in the high detrital carbonate content intervals, reflecting low amounts of U and Th in these detrital minerals (see Fig. 5). The $(\text{U}/\text{Th})_{\text{AR}}$ and U/Th mass ratios range 0.36 ± 0.01 to 1.41 ± 0.01 , and 0.12 ± 0.003 to 0.48 ± 0.01 (Fig. 5), respectively, whereas the $(^{234}\text{U}/^{238}\text{U})_{\text{AR}}$ varies between 0.88 ± 0.03 and 1.13 ± 0.01 (Fig. 5). ^{230}Th activities fluctuate significantly in the sequence, with values ranging from 0.56 ± 0.01 to $3.66 \pm 0.37 \text{ dpm.g}^{-1}$, and following a progressive increase upward (Fig. 5). ^{231}Pa activities range 0.013 ± 0.001 to $0.365 \pm 0.022 \text{ dpm.g}^{-1}$, with a similarly increasing trend towards the post-glacial (Fig. 5). For both isotopes, extremely low contents are observed in the detrital carbonate layers.

2.4 Discussion

2.4.1 Late vs early diagenetic evolution of U-contents and activity ratios

Redox conditions are known to be the main factor controlling the U behavior in the marine environment in influencing its solubility. The removal of U into anoxic (or suboxic) sediments mostly depends on productivity-driven fluxes of particulate organic matter to the seafloor, on the supply of oxygen linked to deep-water ventilation and on sedimentation rates. The alpha-recoil effect is also an important process to consider due to the disequilibrium it produces between ^{234}U and ^{238}U (e.g., Cochran, 1992; Henderson and Anderson, 2003).

Throughout the study sequence, deficits or excesses in ^{234}U (over ^{238}U) are observed. In the glacial and deglacial intervals (i.e., ~36.6-8.3 cal ka BP), $\delta^{234}\text{U}$ offsets from secular equilibrium reach as much as -115 and +74‰ (Fig. 5). As a quite general rule, excesses in ^{234}U over ^{238}U are observed in sediments with high organic matter contents. Under such conditions, strong redox gradients result in the diffusion and precipitation of U below the water-sediment interface (e.g., Gariépy *et al.*, 1994). Here however, organic matter is far from abundant and thus unlikely to influence U-contents or $(^{234}\text{U}/^{238}\text{U})_{\text{AR}}$. One single layer, located just above the Heinrich 2 interval (i.e., deposited during the Last Glacial Maximum -LGM- *stricto sensu*), shows some correlation between U-concentrations, excesses in ^{234}U vs ^{238}U , and C_{org} contents. Accordingly, elsewhere in the study sequence, deficits in ^{234}U vs ^{238}U might result from loss of uranium with preferential ^{234}U -leaching, either through the continental cycling of carrier particles (in soils for example), or during their transport (e.g., clays from distal locations) and sedimentation. Now, in chemically poorly reactive sub-polar environments, chemical weathering might be seen as ineffective, although Refsnider *et al.* (2012) have reported very high ^{234}U excesses in subglacial calcites, leading to hypothesize ^{234}U -depleted "reservoirs" in source rocks. Similarly, large

departures from $^{234}\text{U}/^{238}\text{U}$ equilibrium have been reported in high latitude peats and permafrost systems (Schirrmeyer *et al.*, 2002). Thus, since sedimentary supplies from such sources cannot be discarded, any unequivocal interpretations of U-isotope behavior in the study core must be discarded. Moreover, one cannot discard either a late diagenetic evolution in the sediment with ^{234}U -enriched U displaced in relation with discrete redox gradients (e.g., Colley and Thomson, 1992; Thomson *et al.*, 1996). Such a process was already suggested by Vallières (1997; Fig. S2) for a core retrieved from the Greenland continental slope and in which (i) large deficits in ^{234}U vs ^{238}U were recorded within oxidized sediments deposited during the glacial intervals of MIS 2, 4 and 6, whereas (ii) strong excesses were observed in the immediate under- and overlying reduced layers deposited during interstadials and interglacials.

In core 004PC, the $(^{234}\text{U}/^{238}\text{U})_{\text{AR}}$ are mostly low within the brown oxidized fast-deposited Heinrich layers, as well as throughout the glacial sediments. The corresponding sediment furthermore records very low C_{org} contents. In comparison, $(^{234}\text{U}/^{238}\text{U})_{\text{AR}}$ are higher in deglacial to post-glacial sediments, and also depict a few high values in the sediment immediately overlying H2- and H1-layers (Fig. 5). As a matter of fact, at least one of these intervals with high $(^{234}\text{U}/^{238}\text{U})_{\text{AR}}$, above H2, is also characterized by a high organic carbon content (Fig. 4), which might have led to some early diagenetic U-uptake from the water column. However, as already stated above, the overall variability of $(^{234}\text{U}/^{238}\text{U})_{\text{AR}}$ cannot permit to discard a late diagenetic U-relocation in relation with discrete redox gradients.

In the post-glacial sedimentary section (i.e., $\leq \sim 8.3$ cal ka BP), the excesses in ^{234}U (with $\delta^{234}\text{U}$ averaging $\sim +84\text{\textperthousand}$) suggest uptake of marine U either through fluxes of biogenic U-carriers, and/or due to early diagenetic diffusion from the deep-water mass into the sediment. Using the $^{234}\text{U}/^{238}\text{U}$ activity ratio of 1.146 ± 0.002 in seawater (Cheng *et al.*, 2000) and assuming the deposition of detrital particles with U isotopes

in secular equilibrium, this U-flux would account for up to 50% of the total U measured.

A significant and progressive increase in calcite abundance is observed during the last ~9.7 cal ka BP (Figs. 3, 4; see also Gibb *et al.*, 2014). It is likely of biogenic origin since the dolomite abundance is almost nil in this interval. Previous studies based on correlations between calcite and primary productivity indicators, mostly coccoliths, also suggest this hypothesis (see Hillaire-Marcel *et al.*, 1994b; Veiga-Pires, 1998; Vallières, 1997). However, authigenic U linked to the resulting micritic rain should not have contributed to a significant part of the U-uptake in the core top sediment, since most biogenic minerals show very low amounts of authigenic uranium (e.g., ~ 4.92 ± 0.01 ng.g⁻¹ in foraminifers from a Greenland Rise core; Hillaire-Marcel, 2009).

The C_{org} content of the sediment is relatively low for the post-glacial sediments (~0.3 ± 0.05 dw% on average). These might be the result of a near-complete oxidation of the fresh organic matter, along with the drop of sedimentation rates also observed (see also Hillaire-Marcel *et al.*, 1994b). The early diagenetic precipitation of U would have occurred or be still active below the core-top 4 cm, as this layer is characterized by (²³⁴U/²³⁸U)_{AR} much closer to secular equilibrium. As a matter of fact, a transition from brown (oxidized) to gray (reduced) color is observed at a depth of ~ 7 cm (see Gariépy *et al.*, 1994).

Worth of mention is the fact that the layer dated at ~8.3 cal ka BP and assigned to the final Lake Agassiz drainage shows a relatively high calcite abundance (Fig. 3) together with an excess of ²³⁴U over ²³⁸U. However, the absence of dolomite in this layer, and the fact that nearly constant calcite percentages are also observed in the under- and overlying sediments, lead us to assign this calcite to a more or less steady biogenic carbonate production.

2.4.2 Terrigenous detrital supply

Based on U/Th activity and mass ratios, Vallières (1997) then Veiga-Pires (1998) identified three different regional signatures of terrigenous detrital material in the Labrador Sea: (i) the Reykjanes ridge, (ii) the Labrador continental slope, and (iii) the Greenland continental slope (see Fig. 1). The distal supply would also be dependent on the WBUC intensity carrying fine particles from the Reykjanes ridge (Fagel *et al.*, 1996; Hillaire-Marcel *et al.*, 1994a; see also Veiga-Pires, 1998). In 004PC glacial and deglacial sediments, large variations of U/Th activity and mass ratios are reported. Assuming in a first approximation that $(^{234}\text{U}/^{238}\text{U})_{\text{AR}}$ are close to secular equilibrium and since any significant early-diagenetic U-uptake might have only occurred in the very core top sediment, these large amplitude variations mostly suggest changes in terrigenous detrital sediment sources (Fig. 5).

2.4.3 Constraints from $(^{230}\text{Th}_{\text{xs}})_0$ and $(^{231}\text{Pa}_{\text{xs}})_0$

The production rate of ^{230}Th and ^{231}Pa in the water column is nearly constant but for the ~3% change in U-concentration and salinity between glacial and interglacial episodes (e.g., Schmidt and Spero, 2008; see also Not *et al.*, 2012). The theoretical $^{230}\text{Th}_{\text{xs}}$ vertical flux, $F(^{230}\text{Th}_{\text{xs}})_v$, calculated for the 2674 m water depth of 004PC site, is ~7.14 dpm.cm⁻².ka⁻¹ (Fig. 5; cf. Suman and Bacon, 1989). Within the above ~3% uncertainty range and neglecting glacial/interglacial changes in sea-level thus variations in water depth at the site, this value hence represents the $^{230}\text{Th}_{\text{xs}}$ flux at the seafloor strictly linked to U-decay in the overlying water column. It has been used to estimate deviations of measured initial excess of ^{230}Th fluxes in the sediment samples (i.e., $(F^{230}\text{Th}_{\text{xs}})_M$; see Fig. 6).

To estimate initial excesses, measured values (^{230}Th and ^{231}Pa ; dpm.g⁻¹) were corrected from: (i) the supported component from U present in mineral lattices of

detrital particles, (ii) the authigenic component (applied only on the data of post-glacial interval $\sim 0.44\text{-}8.3$ cal ka BP), and (iii) the natural decay since the time of deposition. This approach implies that the U-series isotopes are in secular equilibrium in the detrital component and that the ^{238}U -decay can be neglected. Calculations were done as follows:

$$(1) \quad (^{230}\text{Th}_{xs})_0 = e^{\lambda_{230} t} [^{230}\text{Th} - (R_d * ^{232}\text{Th}) - (1.14 * (^{238}\text{U} - R_d * ^{232}\text{Th}) * (1 - e^{-\lambda_{230} t}))]$$

$$(2) \quad (^{231}\text{Pa}_{xs})_0 = e^{\lambda_{231} t} [^{231}\text{Pa} - (0.046 * R_d * ^{232}\text{Th}) - 1.14 * ((0.046 * ^{238}\text{U}) - (0.046 * R_d * ^{232}\text{Th})) * (1 - e^{-\lambda_{231} t})]$$

Where $(^{230}\text{Th}_{xs})_0$ and $(^{231}\text{Pa}_{xs})_0$ represent the initial activities of both isotopes (dpm.g^{-1}), λ is the disintegration constant (time unit $^{-1}$), t represents the time since the deposition of the sediment (time unit) obtained from independent radiocarbon chronology (Gibb *et al.*, 2014), ^{232}Th corresponds to ^{232}Th measured in the sediment (dpm.g^{-1}), 0.046 is the $(^{235}\text{U}/^{238}\text{U})_{\text{AR}}$ value in natural material, R_d corresponds to the mean of the $(^{238}\text{U}/^{232}\text{Th})_{\text{AR}}$ for the detrital component.

Considering that all data points from the late glacial section ($\sim 36.6\text{-}12.2$ ka, Heinrich-layers excluded) are representative of detrital material, the mean $(^{238}\text{U}/^{232}\text{Th})_{\text{AR}}$ calculated on this interval is ~ 0.61 . This value is used as the detrital value for the sediment $> \sim 8.3$ cal ka BP (Fig. 5). The mean $(^{238}\text{U}/^{232}\text{Th})_{\text{AR}}$ of the oxidized uppermost 4 cm equals to ~ 0.47 , and is considered as representative of the detrital fraction for the post-glacial interval. These values are concordant with those acquired elsewhere in North Atlantic sediments (e.g., ~ 0.58 at Orphan Knoll from Veiga-Pires and Hillaire-Marcel, 1999). Inside the glacial and deglacial intervals ($\sim 36.6\text{-}8.3$ cal ka BP), ^{234}U -offsets from secular equilibrium are estimated to be less than 4.4% on an average. The uncertainty on the estimation of the initial excesses of ^{230}Th and ^{231}Pa is therefore also set at $\leq \pm 4.4\%$. Note that the overall analytical uncertainty is estimated to be better than $\sim \pm 10.4\%$ for $(^{231}\text{Pa}_{xs})_0$, and $\sim \pm 8.5\%$ for $(^{230}\text{Th}_{xs})_0$. The overall

analytical uncertainty for $(^{231}\text{Pa}_{\text{xs}}/^{230}\text{Th}_{\text{xs}})_0$ is then estimated to be within a $\sim \pm 10\text{-}13\%$ range.

Results plotted in Fig. 6 show that $(^{230}\text{Th}_{\text{xs}})_0$ and $(^{231}\text{Pa}_{\text{xs}})_0$ values are highly variable and tend to increase upward in the sequence (Heinrich-layers excluded). Values are especially high in the post-glacial interval, reaching up to $3.08 \pm 0.23 \text{ dpm.g}^{-1}$ for $(^{230}\text{Th}_{\text{xs}})_0$ and $0.35 \pm 0.02 \text{ dpm.g}^{-1}$ for $(^{231}\text{Pa}_{\text{xs}})_0$. These calculations occasionally yielded negative values. Either poor estimates of the age of the corresponding sediments or changes in the mineralogical composition of the detrital fraction, thus in its U/Th ratio, might be evoked. For such intervals, we have considered the excess as null. The analytical errors, in addition to uncertainties about sedimentation rates, adding the high variability of $(^{234}\text{U}/^{238}\text{U})_{\text{AR}}$ and (U/Th) mass ratios, raise doubts about any more precise assessment of the “supported” ^{230}Th and ^{231}Pa -fractions in such a setting, and hence on any interpretation using these tracers.

2.4.4 $(^{230}\text{Th}_{\text{xs}})_0$ durations of H2 and H1

At site 004PC, in the near proximity of the Hudson Strait streaming area, Heinrich layers 2 and 1 are very well documented (Fig. 3). Their boundaries have been delimited based on the carbonate content, a composition markedly different of that in the ambient glacial sediment that consists mostly of quartz and feldspars (e.g., Andrews *et al.*, 2012). During H-event intervals, the sedimentation rate has been much higher than during glacial times as a whole. Their coarse fraction content is high and also displays a strong irregular sawtooth pattern (see also Rashid *et al.*, 2003). Both layers present a laminated structure of sand-size particles alternating with finer particles and high concentration of gravels (especially at their bottom). They also depict a characteristic brown color (Figs. 3, 4). Their calcite/dolomite ratio is ~ 2.5 on average, which is a characteristic value of detrital carbonates originating from Hudson Bay area (e.g., Andrews and Tedesco, 1992). Their isotopic

compositions are characterized by $^{234}\text{U}/^{238}\text{U}$ activity ratio <1 and by very low $(^{230}\text{Th}_{\text{xs}})_0$ and likewise $(^{231}\text{Pa}_{\text{xs}})_0$ values (Figs. 5, 6). Such low values indicate extremely fast deposition (e.g., François and Bacon, 1994). Immediately under- and overlying the H2 and H1 layers, peaks in $(^{230}\text{Th}_{\text{xs}})_0$ are observed as it was the case of similar layers at Orphan Knoll (Veiga-Pires and Hillaire-Marcel, 1999). This feature, possibly linked to the depositional process of H-layers, is still unexplained.

At last, the layer dated older than ~33.7 cal ka BP seems more likely to have been deposited during the H4-event rather than during H3, which has been dated at ~31 cal ka BP (Hemming, 2004; see also Andrews *et al.*, 2014). This >~33.7 cal ka BP layer could be dated more precisely here.

The duration of the deposition of Heinrich layers might also be documented based on $(^{230}\text{Th}_{\text{xs}})_0$ inventories, using the $(^{230}\text{Th}_{\text{xs}})_0$ constant flux approach (e.g., François and Bacon, 1994; Veiga-Pires and Hillaire-Marcel, 1999). Time is estimated from $(^{230}\text{Th}_{\text{xs}})_0$ inventories *vs* a constant $(^{230}\text{Th}_{\text{xs}})_0$ flux at sediment surface, thus neglecting the dependence between $^{230}\text{Th}_{\text{xs}}$ and the particle composition and grain-size, as well as with post-depositional mechanisms. Inventories of $(^{230}\text{Th}_{\text{xs}})_0$ are calculated as follows:

$$(1) \quad I = \sum_i \{ [(^{230}\text{Th}_{\text{xs}})_0]_i * \rho_i * \Delta X_i \}$$

Where the inventory I (I; dpm.cm⁻²) for a given interval of a thickness ΔX_i is the integral of the multiplication of the $(^{230}\text{Th}_{\text{xs}})_0$ with ρ corresponding to the density of the sediment (g of dry sediment per cubic cm of humid sediment).

The $^{230}\text{Th}_{\text{xs}}$ flux at sediment surface may be set either based on vertical production in the overlying water column ($(F^{230}\text{Th}_{\text{xs}})_V$) or from the mean effective $(^{230}\text{Th}_{\text{xs}})_0$ flux

measured ($(F^{230}\text{Th}_{xs})_M$). In the first case, using a $(F^{230}\text{Th}_{xs})_V$ to the seafloor equals to $\sim 7.14 \text{ dpm.cm}^{-2}.\text{ka}^{-1}$, estimated durations would be ~ 3.0 and ~ 3.5 ka for H2 and H1, respectively, i.e., much higher than those reported in the literature (Hemming, 2004). Using the mean $(F^{230}\text{Th}_{xs})_M$ throughout the glacial section (i.e., $\sim 41 \text{ dpm.cm}^{-2}.\text{ka}^{-1}$; see Fig. 5), duration estimates fall to 0.53 and 0.61 ka for H2 and H1, respectively. Comparatively, radiocarbon ages give durations of 0.70 and 1.57 ka for H2 and H1, respectively. Accordingly, in a context of continental margin, where $(F^{230}\text{Th}_{xs})_M$ might be highly variable (Fig. 6), such calculations lead to unconstrained durations. Moreover, linkages between deep currents, grain size, mineralogical composition of detrital fluxes, primary productivity, all have impacts on $^{230}\text{Th}_{xs}$ fluxes (e.g., Chase *et al.*, 2002). Furthermore, some uncertainties also raised from the difficulty to set an upper limit for the H-layers due to bioturbation, as indicated by carbonate profiles, CAT-scan images and visual examination. At last, anomalies evoked above such as the high $^{230}\text{Th}_{xs}$ values immediately above and below H-layers boundaries, add to the uncertainty. Here H2 and H1 were re-delimited on the 712-700 cm and 588-512 cm intervals to mitigate these uncertainties. However, these uncertainties lead to question the representativeness of $(^{230}\text{Th}_{xs})_0$ inventories assigned to Heinrich layers.

2.4.5 $(^{231}\text{Pa}_{xs}/^{230}\text{Th}_{xs})_0$ and paleoceanographic implications

Since dissolved U is reasonably homogeneously distributed in the seawater, $^{230}\text{Th}_{xs}$ and $^{231}\text{Pa}_{xs}$ (half-life $^{230}\text{Th} = 75690 \pm 230$ a; Cheng *et al.*, 2000; half-life $^{231}\text{Pa} = 32760 \pm 220$ a; Robert *et al.*, 1969) are uniformly produced throughout the ocean at a constant activity ratio of ~ 0.092 (François, 2007). Strictly interpreted as paleoceanographic signals, deviations of sedimentary $(^{231}\text{Pa}_{xs}/^{230}\text{Th}_{xs})_0$ ratio from the production ratio might result from fluctuations in (i) particle flux, (ii) particle composition ($^{231}\text{Pa}_{xs}$ is more reactive with biogenic opal and Mn oxides while $^{230}\text{Th}_{xs}$ appears to have more affinity with carbonates; Chase *et al.*, 2002), and/or, (iii) lateral advection of fractionated $^{231}\text{Pa}_{xs}$ vs $^{230}\text{Th}_{xs}$ linked to WBUC transport, assuming that

this current was mostly responsible for off-balance $(^{231}\text{Pa}_{\text{xs}}/^{230}\text{Th}_{\text{xs}})_0$ -budgets (Fran ois, 2007). It cannot be excluded that deviations of $(^{231}\text{Pa}_{\text{xs}}/^{230}\text{Th}_{\text{xs}})_0$ from theoretical value are produced by other mechanisms down-slope, such as particle dependent scavenging rates.

In 004PC core, $(^{231}\text{Pa}_{\text{xs}}/^{230}\text{Th}_{\text{xs}})_0$ values fall generally below the production ratio in the water column (Fig. 6). Throughout the glacial interval, as the particle flux was relatively high ($\geq 12 \text{ cm.ka}^{-1}$; Fig. 2) and the particle composition nearly constant (Heinrich-layers excluded; see Fig. 3), such low values suggest that some ^{231}Pa is exported southward by advection. As illustrated Fig. 6, estimates of $(F^{230}\text{Th}_{\text{xs}})_M$ and $(F^{230}\text{Th}_{\text{xs}})_V$ are not much different throughout most of the record. The only exceptions are short time slices, following H1 and until ~ 8.3 cal ka BP, the late Holocene, and surprisingly the H2 layer interval itself. These exceptions suggest some $^{230}\text{Th}_{\text{xs}}$ advection or focusing. In the post-glacial sedimentary section (i.e., $\leq \sim 8.3$ cal ka BP), $(^{231}\text{Pa}_{\text{xs}}/^{230}\text{Th}_{\text{xs}})_0$ values remain generally lower than the production ratio, whereas overall increases in $(^{230}\text{Th}_{\text{xs}})_0$ and $(^{231}\text{Pa}_{\text{xs}})_0$ values matching enhanced biogenic carbonate production, suggest some role of the micritic rain in the ^{230}Th and ^{231}Pa scavenging.

2.5 Conclusion

A large variability has been observed in U- and Th-series at the study site, in relation with highly variable sedimentary fluxes. The Heinrich-layers H2 and H1 stand out due to their high content in U and Th-poor detrital carbonates, as well as their low $(^{230}\text{Th}_{\text{xs}})_0$ values in response to their fast deposition.

In the study core, redox conditions seem to have induced either some U-uptake from the water column (Holocene) or some late diagenetic U-mobility along discrete redox gradients. The high amplitude variations in $(^{230}\text{Th}_{\text{xs}})_0$, $(^{231}\text{Pa}_{\text{xs}})_0$ and accordingly $(^{231}\text{Pa}_{\text{xs}}/^{230}\text{Th}_{\text{xs}})_0$ ratio suggest highly variable fluxes of these isotopes at sediment surface. As a consequence, the use of $(^{230}\text{Th}_{\text{xs}})_0$ inventories to put time constraints on Heinrich-layer depositional intervals seems out of reach. Moreover, methodological limitations make precise estimation of the supported vs ingrowth fractions of these isotopes quite challenging. The most robust features to retain here are:

- 1) $(^{231}\text{Pa}_{\text{xs}}/^{230}\text{Th}_{\text{xs}})_0$ values indicating a nearly continuous export of $^{231}\text{Pa}_{\text{xs}}$ vs $^{230}\text{Th}_{\text{xs}}$.
- 2) $(F^{230}\text{Th}_{\text{xs}})_M$ illustrating contrasted regimes with notably high advection or focusing during the deglacial interval and the late Holocene, likely due to distinct type of particulate fluxes (i.e., respectively mostly detrital vs biogeochemically enhanced fluxes).

Finally, the high geochemical and sedimentary variability observed on the Labrador Sea slopes yield to challenge any unequivocal use of U- and Th-series isotopes for paleoceanographic reconstructions under such settings.

Acknowledgments

This study is part of the Canadian contribution to the Past4Future project of the 7th Framework Program of the European Commission. Support is acknowledged from MDEIE (Ministère du Développement Économique, de l’Innovation et de l’Exportation) and FRQNT (Fonds de la Recherche du Québec sur la Nature et les Technologies). Financial support from the Canadian Foundation for Climate and Atmospheric Sciences (CFCAS), the Natural Resources Canada (NRCan), and the Natural Sciences and Engineering Research Council of Canada (NSERC) is acknowledged for the sampling expedition. Special thanks are due to Bassam Ghaleb for his help in U- and Th-series analyses assistance and to Michel Preda for his help to XRD measurements at the GEOTOP laboratories.

References

- Anderson, R.F., Lao, Y., Broecker, W.S., Trumbore, S.E., Hofmann, H.J., Wolfli, W., (1990), Boundary scavenging in the Pacific Ocean: a comparison of ^{10}Be and ^{231}Pa , *Earth and Planetary Science Letters*, 96, 287–304.
- Andrews, J. T., O. Gibb, A. E. Jennings, and Q. Simon (2014), Variations in the provenance of sediment from ice sheets surrounding Baffin Bay during MIS 2 and 3 and export to the Labrador Shelf Sea: site HU2008029-0008 Davis Strait, *Journal of Quaternary Science*, 29, 3-13.
- Andrews, J. T., D. C. Barber, A. E. Jenning, D. D. Eberl, B. MacClean, M. E. Kirby, and J. S. Stoner (2012), Varying sediment sources (Hudson Strait, Cumberland Sound, Baffin Bay) to the NW Labrador Sea slope between and during Heinrich events 0 to 4, *Journal of Quaternary Science*, 1-10.
- Andrews, J. T., K. Tedesco, W. M. Briggs, and L. W. Evans (1994), Sediments, sedimentation rates, and environments, SE Baffin Shelf and NW Labrador Sea 8 to 26 Ka, *Canadian Journal Earth Sciences*, 31, 90–103.
- Andrews, J. T., and K. Tedesco (1992), Detrital carbonate-rich sediments, northwestern Labrador Sea: Implications for ice-sheet dynamics and iceberg rafting (Heinrich) events in the North Atlantic, *Geology*, 20, 1087-1090.
- Barber, D. C., A. Dyke, C. Hillaire-Marcel, A. E. Jennings, J. T. Andrews, M. W. Kerwin, G. Bilodeau, R. McNeely, J. Southon, M. D. Morehead, and J.-M. Gagnonk (1999), Forcing of the cold event of 8,200 years ago by catastrophic drainage of Laurentide lakes, *Nature* 400, 344-348.
- Broecker, W. S. (1991), The great conveyor belt, *Oceanography*, 4(2), 79-89.
- Campbell, D. C., and A. de Vernal (2009), Marine geology and paleoceanography of Baffin Bay and adjacent areas. Nain, NL to halifax, NS, August 28-September 23, 2008. Cruise report of CCGS Hudson Expedition 2008029, Geological Survey of Canada, Open File 5989, Natural Resources Canada, 2010 pages.
- Chase, Z., R. F. Anderson, M. Q. Fleisher, and K. P.W. (2002), The influence of particle composition and particle flux on scavenging of Th, Pa and Be in the ocean, *Earth and Planetary Science Letters*, 204, 215-229.
- Cheng, H., R. L. Edwards, J. Hoff, C. D. Gallup, D. A. Richards, and Y. Asmerom (2000), The half-lives of uranium-234 and thorium-230, *Chemical Geology*, 169, 17–33.

- Choi, M. S., R. Francois, K. Sims, M. P. Bacon, S. Brown-Leger, A. P. Fleer, L. Ball, D. Schneider, and S. Pichat (2001), Rapid determination of Th-230 and Pa-231 in seawater by desolvated micro-nebulization Inductively Coupled Plasma magnetic sector mass spectrometry, *Marine Chemistry*, 76, 99-112.
- Cochran, J. K. (1992), The oceanic chemistry of the uranium- and thorium-series nuclides, in *Uranium-series Disequilibrium: Application to Earth, Marine, and Environmental Sciences*, edited by M. Ivanovich and R. S. Harmon, pp. 334-395, Clarendon Press, Oxford.
- Colley, S., and J. Thomson (1992), Behaviour and mobility of U series radionuclides in Madeira Abyssal Plain turbidites over the past 750,000 years, *Marine Geology*, 109, 141-158.
- Fagel, N., C. Robert, and C. Hillaire-Marcel (1996), Clay mineral signature of the NW Atlantic Boundary Undercurrent, *Marine Geology*, 130(1-2), 19-28.
- François, R. (2007), Paleoflux and Paleocirculation from Sediment 230Th and 231Pa/230Th, in *Proxies in Late Cenozoic Paleoceanography*, edited by C. Hillaire-Marcel and A. de Vernal, pp. 681-716, Elsevier.
- François, R., and M. P. Bacon (1994), Heinrich events in the North Atlantic: radiochemical evidence, *Deep-Sea Research I*, 41, 315-334.
- Gariépy, C., B. Ghaleb, C. Hillaire-Marcel, A. Mucci, and S. Vallières (1994), Early diagenetic processes in Labrador Sea sediments: uranium-isotope geochemistry, *Canadian Journal of Earth Sciences*, 31(1), 28-37.
- Gibb, O., C. Hillaire-Marcel, and A. de Vernal (2014), Oceanographic regimes in the northwest Labrador Sea since Marine Isotope stage 3 based on dinocyst and stable isotope proxy records, *Quaternary Science Reviews*, 92, p. 269-279.
- Hélie, J.-F. (2009), Elemental and stable isotopic approaches for studying the organic and $\delta^{13}\text{C}$ inorganic carbon components in natural samples. In *Deep-Sea to Coastal Zones: Methods Techniques for Studying Paleoenvironments*, *IOP Conference Series: Earth and Environmental Science*, 5, 012006.
- Hemming, S. R. (2004), Heinrich events: Massive late Pleistocene detritus layers of the North Atlantic and their global climate imprint, *Review of Geophysics*, 42, 1-43.
- Henderson, G. M., and R. F. Anderson (2003), The U-series Toolbox for Paleoceanography, *Mineralogical Society of America*, 52(1), 493-531.

- Hillaire-Marcel, C. (2009), The U-series dating of (biogenic) carbonates, *IOP Conference Series: Earth and Environmental Science*, 5(1), 012008.
- Hillaire-Marcel, C., A. de Vernal, and D. J. W. Piper (2007), Lake Agassiz Final drainage event in the northwest North Atlantic, *Geophysical Research Letters*, 34, L15601.
- Hillaire-Marcel, C., A. De Vernal, G. Bilodeau, and A. J. Weaver (2001), Absence of deep-water formation in the Labrador Sea during the last interglacial period, *Nature*, 410(6832), 1073-1077.
- Hillaire-Marcel, C., A. de Vernal, G. Bilodeau, and G. Wu (1994a), Isotope stratigraphy, sedimentation rates, deep circulation, and carbonate events in the Labrador Sea during the last ~200 ka, *Canadian Journal of Earth Sciences*, 31, 63-89.
- Hillaire-Marcel, C., A. de Vernal, M. Lucotte, and A. Mucci (1994b), La mer du Labrador au cours du Quaternaire récent: Avant-propos., *Revue canadienne des sciences de la Terre*, 31, 1-4.
- Hillaire-Marcel, C., A. de Vernal, M. Lucotte, A. Mucci, G. Bilodeau, A. Rochon, S. Vallières, and G. Wu (1994c), Productivité et flux de carbone dans la mer du Labrador au cours des derniers 40 000 ans, *Canadian Journal Earth Sciences*, 31(1), 139-158.
- Lally, A. E. (1992), Chemical procedures, in Uranium series disequilibrium: Applications to Earth, Marine, and Environmental Sciences, edited by M. Ivanovich and R. S. Harmon, pp. 95-126, Clarendon Press, Oxford.
- Last, W. M. (2001), Mineralogy analysis of lake sediments, in Tracking Environmental Change Using Lake Sediments, edited by W. M. Last and J. P. Smol, pp. 143-187, Kluwer Academic Publishers, Dordrecht, The Netherlands.
- Lazier, J. R. N. (1973), The renewal of Labrador Sea Water, *Deep Sea Research*, 20(4), 341-353.
- Lewis, C. F. M., A. A. L. Miller, E. Levac, D. J. W. Piper, and G. V. Sonnichsen (2012), Lake Agassiz outburst age and routing by Labrador Current and the 8.2 cal ka cold event, *Quaternary International*, 260, 83-97.
- Moore, D. M., and J. C. Reynolds (1997), X-Ray Diffraction and the Identification and Analysis of Clay Minerals, Oxford University Press, New York.

- Nicholl, J. A. L., D. A. Hodell, B. D. A. Naafs, C. Hillaire-Marcel, J. E. T. Channell, and O. E. Romero (2012), A Laurentide outburst flooding event during the last interglacial period, *Nature geoscience*, 5, 901-904.
- Not, C., K. Brown, B. Ghaleb, and C. Hillaire-Marcel (2012), Conservative behavior of uranium vs. salinity in Arctic sea ice and brine, *Marine Chemistry*, 130-131, 33-39.
- Pearce, C., M.-S. Seidenkrantz, A. Kuijpers, G. Massé, N. F. Reynisson, and S.M. Kristiansen (2013), Ocean lead at the termination of the Younger Dryas cold spell, *Nature Communications*, 4: 1664.
- Ramsey, C. B. (2008), Deposition models for chronological records, *Quaternary Science Reviews*, 772(1), 42-60.
- Rashid, H., R. Hesse, and D. J. W. Piper (2003), Origin of unusually thick Heinrich layers in ice-proximal regions of the northwest Labrador Sea, *Earth and Planetary Science Letters*, 208, 319-336.
- Rashid, H., F. Saint-Ange, D. C. Barber, M. E. Smith, and N. Devalia (2012), Fine scale sediment structure and geochemical signature between eastern and western North Atlantic during Heinrich events 1 and 2, *Quaternary Science Reviews*, 46, 136-150.
- Refsnider, K. A., G. H. Miller, C. Hillaire-Marcel, M. L. Fogel, B. Ghaleb, and R. Bowden (2012), Subglacial carbonates constrain basal conditions and oxygen isotopic composition of the Laurentide Ice Sheet over Arctic Canada, *Geology*, 40(2), 135-138.
- Reimer, P. J., M. G. L. Baillie, E. Bard, A. Bayliss, J. W. Beck, P. G. Blackwell, C. B. Ramsey, C. E. Buck, G. C. Burr, R. L. Edwards, M. Friedrich, P. M. Grootes, T. P. Guilderson, I. Hajdas, T. J. Heaton, A. G. Hogg, K. A. Hughen, K. F. Kaiser, B. Kromer, F. G. McCormac, S. W. Manning, R. W. Reimer, D. A. Richards, J. R. Southon, S. Talamo, C. S. M. Turney, J. van der Plicht, and C. E. Weyhenmeyer (2009), IntCal09 and marine09 radiocarbon age calibration curves, 0–50,000 years cal BP, *Radiocarbon*, 51, 1111–1150.
- Robert, J., C. F. Miranda, and R. Muxart (1969), Mesure de la période du protactinium-231 par microcalorimétrie, *Radiochimical Acta*, 11, 104-108.
- Schirrmeyer, L., D. Oezen, and M. A. Geyh (2002), 230Th/U Dating of Frozen Peat, Bol'shoy Lyakhovsky Island (Northern Siberia), *Quaternary Research*, 57, 253-258.

- Schmidt, M. W., and H. J. Spero (2008), North Altantic salinity oscillations linked to changes in atmospheric and ocean circulation over the last glacial cycle, *PAGES News*, 16(1), 23-25.
- St-Onge, G., and B. F. Long (2009), CAT-scan analysis of sedimentary sequences: an ultrahigh-resolution paleoclimatic tool, *Engineering Geology*, 103, 127–133.
- Suman, D. O., and M. P. Bacon (1989), Variations in Holocene sedimentation in the North American Basin determined from ^{230}Th measurements, *Deep Sea Research Part A. Oceanographic Research Papers*, 36, 869-878.
- Thomson, J., N. C. Higgs, and S. Colley (1996), Diagenetic redistributions of redox-sensitive elements in northeast Atlantic glacial/interglacial transition sediments, *Earth and Planetary Science Letters*, 139, 365-377.
- Thorez, J. (2003), L'argile, minéral pluriel, *Bulletin de la Société Royale des Sciences de Liège*, 72, 19-70.
- Vallières, S. (1997), Flux d'uranium et excès de ^{230}Th dans les sédiments de la Mer du Labrador - Relation avec les conditions paléocénographiques et la paléoproduction du bassin, 144 pp, Université du Québec à Montréal, Montréal (QC), Canada.
- Veiga-Pires, C. C. (1998), Flux de thorium-230 et flux sédimentaires dans l'Atlantique du Nord Ouest au cours des derniers 40 ka en relation avec les variations du climat, environment sciences thesis, 169 pp, Université du Québec à Montréal, Montréal.
- Veiga-Pires, C. C., and C. Hillaire-Marcel (1999), U and Th isotope constraints on the duration of Heinrich events H0-H4 in the southeastern Labrador Sea, *Paleoceanography*, 14(2), 187-199.
- Wu, G., and C. Hillaire-Marcel (1994), Accelerator mass spectrometry radiocarbon stratigraphies in deep Labrador Sea cores: paleoceanographic implications, *Canadian Journal Earth Sciences*, 31(1), 38-47.
- Yu, E. F., R. Francois, and M. P. Bacon (1996), Similar rates of modern and last-glacial ocean thermohaline circulation inferred from radiochemical data, *Nature*, 379, 689-694.

Figures

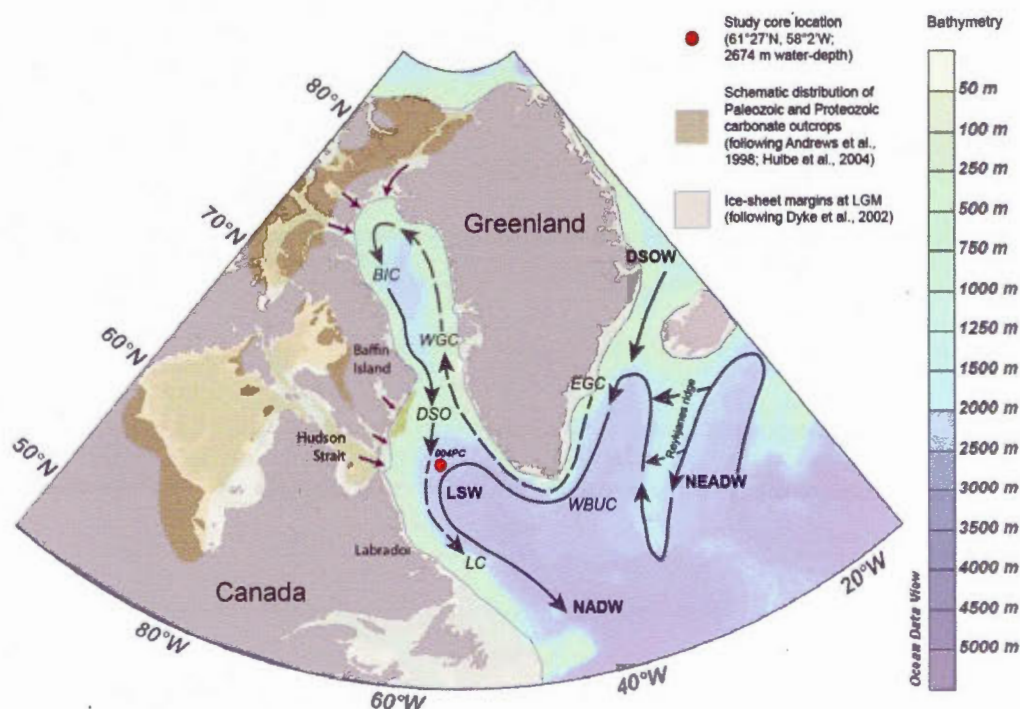


Figure 1 – Location map of core HU08-029-004PC in the Labrador Sea: bathymetry, ice-sheet extension during the Last Glacial Maximum, carbonate outcrops with major ice streaming outlets toward the ocean (purple arrows) and schematic illustration of the major components of the Atlantic Meridional Overturning Circulation (AMOC). Present-day deep (solid lines) and intermediate (dashed lines) oceanic currents and water masses (WGC – Western Greenland Current; BIC – Baffin Island Current; DSO – Davis Strait Overflow; LC – Labrador Current; EGC – East Greenland Current; WBUC – Western Boundary Undercurrent; NEADW – Northeast Atlantic Deep Water; LSW – Labrador Sea Water; DSOW – Denmark Strait Overflow Water; NADW – North Atlantic Deep Water).

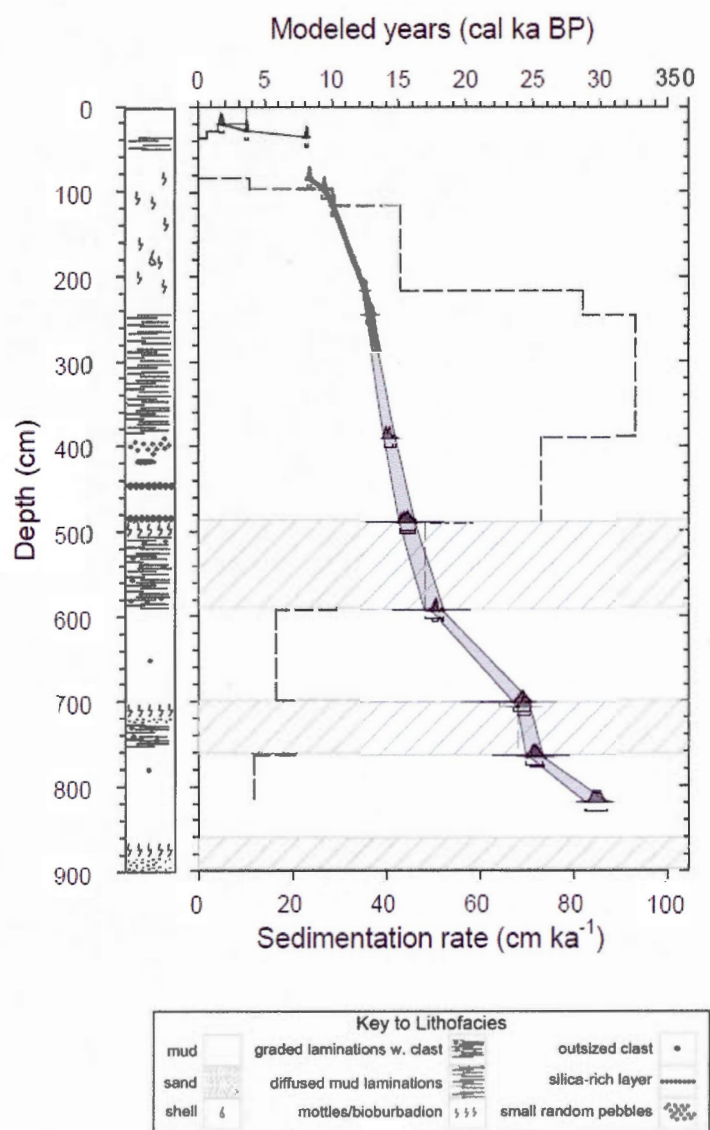


Figure 2 – Core HU08-029-004PC: Age depth model based on calibrated radiocarbon ages, sedimentation rate and lithostratigraphy (from Gibb *et al.*, 2014).

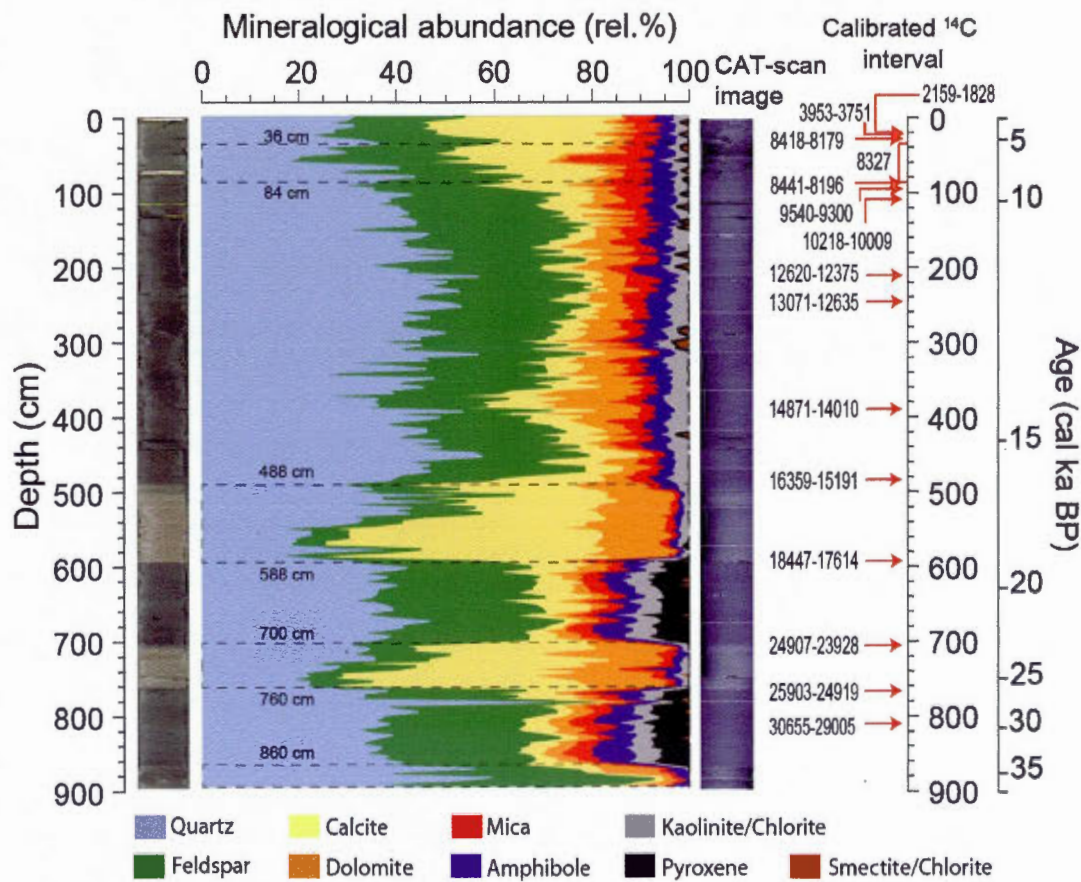


Figure 3 – Mineralogical abundance vs core depth and sediment age. From left to right: photography; semi-quantitative ($\pm 1\sigma \approx 5\%$) mineralogical abundances (relative %); CAT-scan image; modelled calibrated radiocarbon age intervals ($\pm 2\sigma$; from Gibb *et al.*, in press). The dashed lines correspond to rapid depositional Heinrich layers and to the sediment layer associated with the final drainage of Lake Agassiz (their depth boundaries were identified based on the detrital carbonate content).

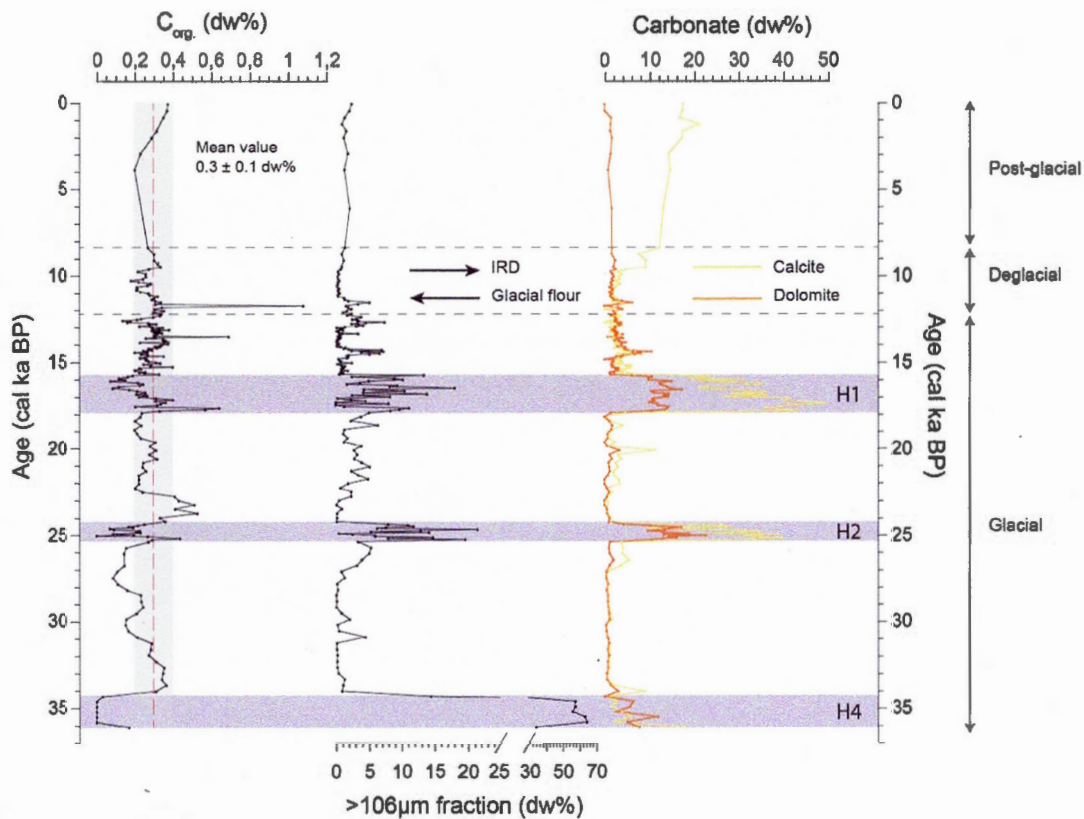


Figure 4 – Sedimentological parameters *vs* age. From left to right: C_{org} content (mean value and standard deviation); coarse fraction of the sediment ($>106\mu\text{m}$ in dry weight percent; dw% $>106\mu\text{m}$); carbonate content (calcite and dolomite in dw%). The gray horizontal intervals correspond to rapid depositional Heinrich layers and to the sediment layer associated with the final drainage of Lake Agassiz. The dashed lines correspond to boundaries between the three oceanic regimes: glacial, deglacial and post-glacial (see text for explanations).

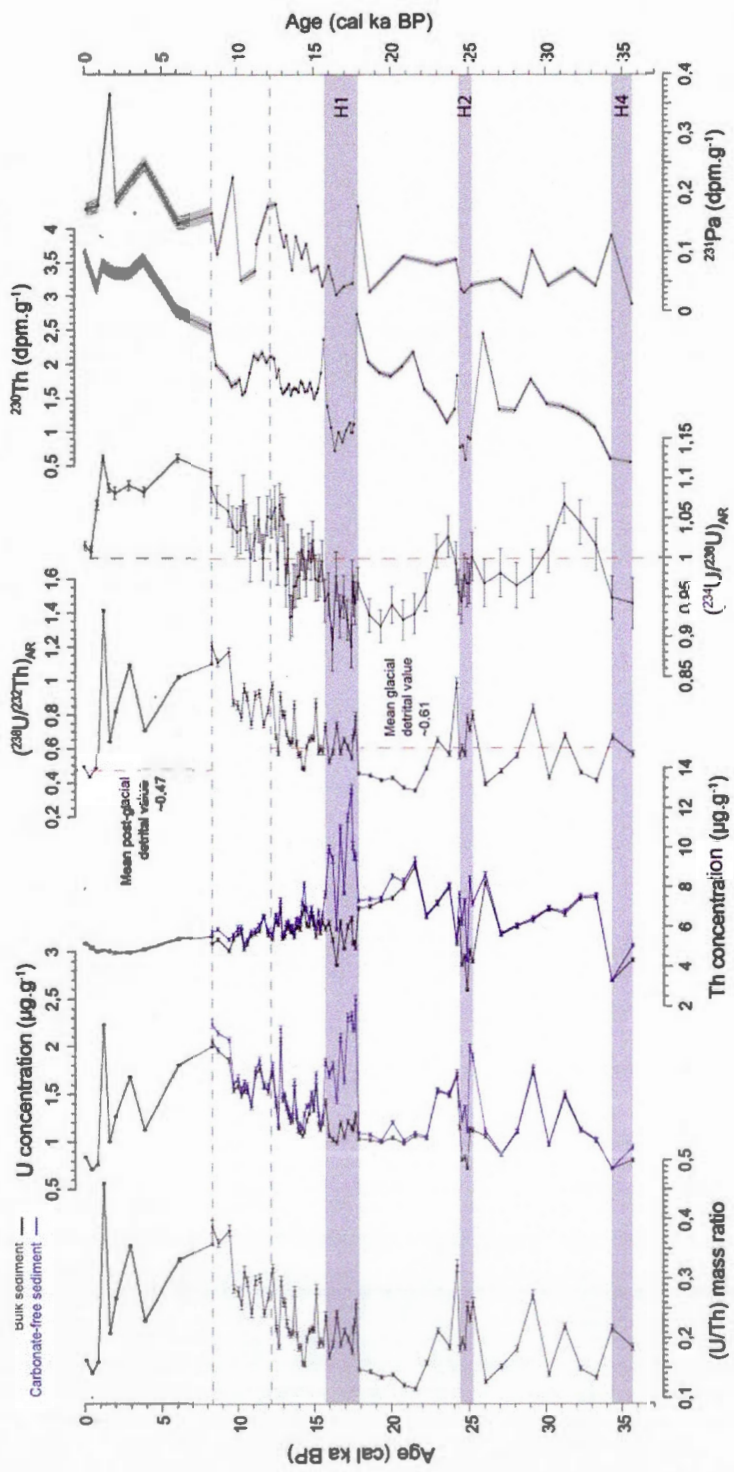


Figure 5 – U-, Th- and Pa-concentrations, mass and activity ratios vs age. From left to right: (U/Th) mass ratio; U-concentration; Th-concentration; U-Th activity ratio; $^{234}\text{U}/^{238}\text{U}$ activity ratio; ^{231}Pa activity. Data points are represented with their $\pm 1\sigma$ analytical uncertainty. The gray horizontal intervals correspond to the rapidly deposited Heinrich layers and to the sediment layer associated with the final drainage of Lake Agassiz. The dashed lines correspond to boundaries between the three oceanic regimes: glacial, deglacial and post-glacial (see text for explanations). As the detrital carbonate content is highly variable in the glacial-deglacial part of the sequence, U- and Th- concentrations were converted into carbonate-free sediment for these intervals, as follows:

$$\text{U}_{\text{carbonate-free sediment}} = (\text{U} * 100) / (100 - \text{dw}\% \text{CaCO}_3); \text{Th}_{\text{carbonate-free sediment}} = (\text{Th} * 100) / (100 - \text{dw}\% \text{CaCO}_3)$$

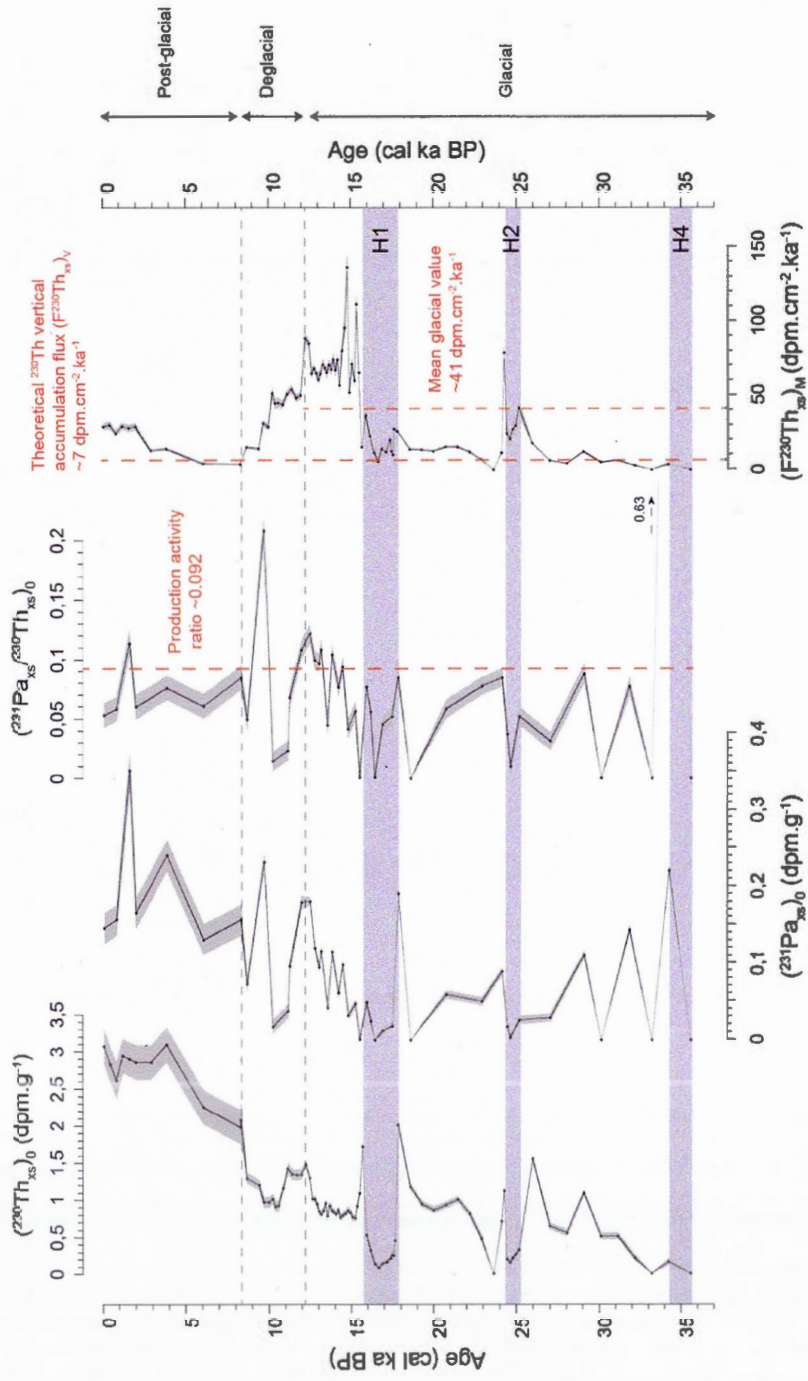


Figure 6 – ^{230}Th - and ^{231}Pa -concentrations and activity ratios, and $(^{230}\text{Th}_{\text{xs}})_0$ inventory vs age. From left to right: initial excess of ^{230}Th activity; initial excess of ^{231}Pa activity; initial $^{231}\text{Pa}_{\text{xs}}$ normalized to the $^{230}\text{Th}_{\text{xs}}$; measured initial $^{230}\text{Th}_{\text{xs}}$ flux. Data are plotted with their $\pm 1\sigma$ analytical uncertainty. The gray horizontal intervals correspond to the rapidly deposited Heimrich layers and to the sediment layer associated with the final drainage of Lake Agassiz. The dashed lines correspond to boundaries between the three oceanic regimes: glacial, deglacial and post-glacial (see text for explanations).

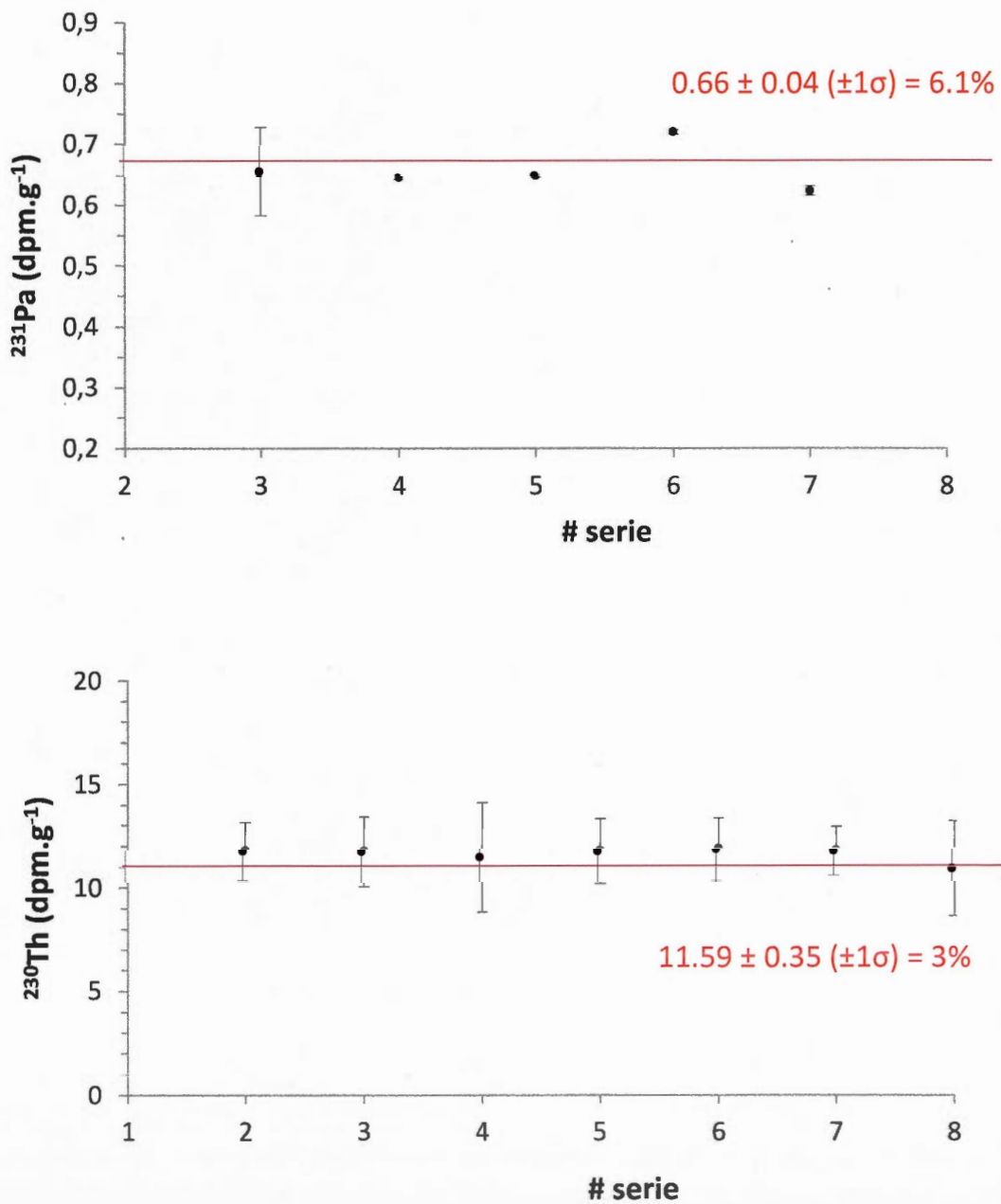


Figure S1 – Analytical uncertainties for ^{230}Th and ^{231}Pa , estimated to be ~3% and ~6.1% respectively, based on replicate analyses of a sample (deep Arctic surface sediment).

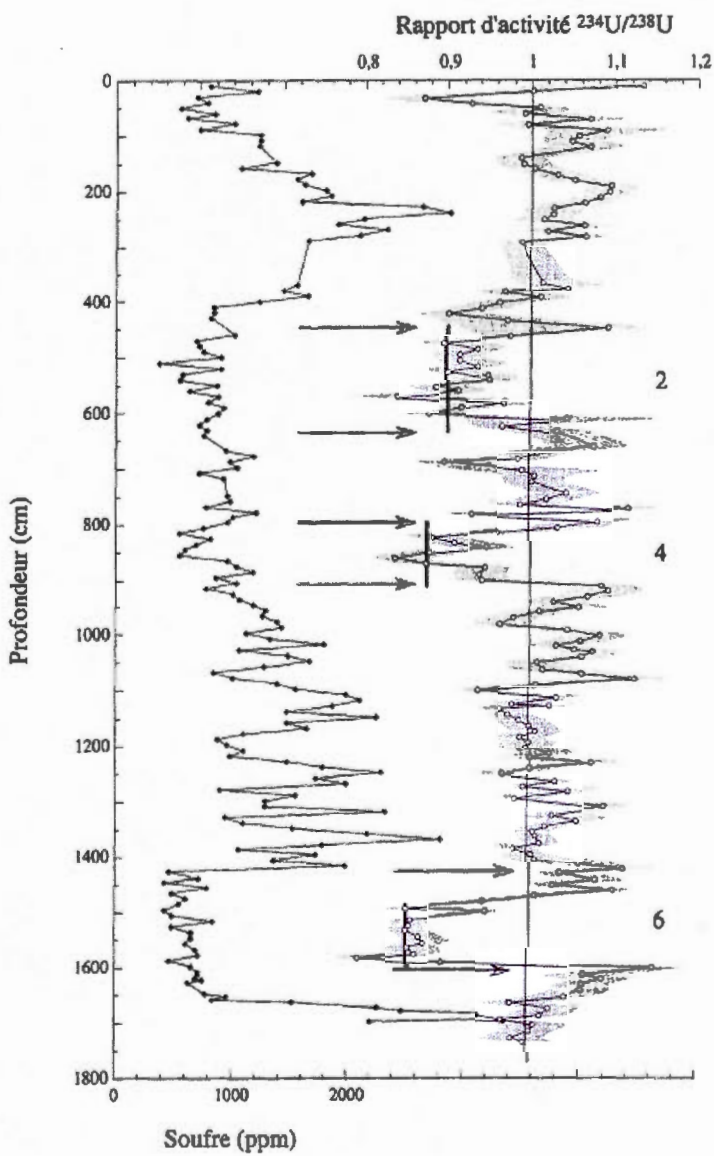


Figure S2 – Changes in $^{234}\text{U}/^{238}\text{U}$ activity ratios and sulfur content vs depth in the 90-013-013 sediment sequence (Greenland continental slope; from Vallières, 1997). The arrows indicate the re-localization areas of late diagenetic uranium from the oxidized intervals of marine isotopic stages 2, 4 and 6.

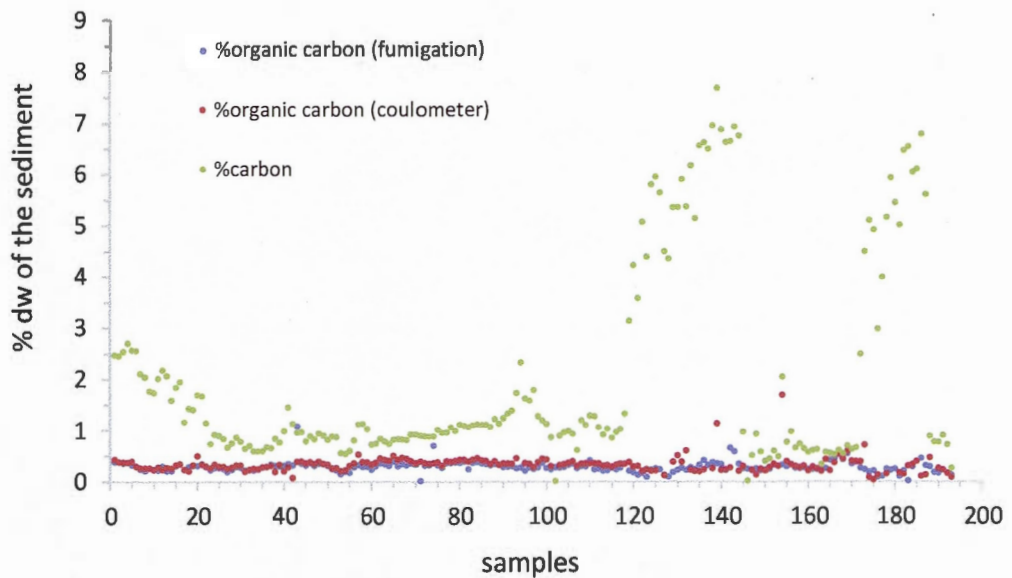


Figure S3 – Fraction in dry weight bulk sediment (dw%) of total carbon and organic carbon measured by both fumigation and coulometer techniques (see text for explanations).

CONCLUSION GÉNÉRALE

La présente recherche s'est attardée à l'étude des sédiments profonds du Quaternaire récent provenant de la baie de Baffin et de la mer du Labrador. L'objectif était d'évaluer précisément la dynamique sédimentaire passée de ces deux bassins océaniques localisés en zone de marges continentales, afin d'obtenir une information originale en ce qui a trait à l'évolution de l'océanographie et de la dynamique glaciaire de la région au cours du dernier cycle glaciaire. Pour y parvenir, nous avons choisi d'utiliser les séries de l'U et du Th, plus particulièrement des isotopes de l'U, du Th et du Pa, trois éléments chimiques de la famille des actinides. En effet, dans les études sédimentologiques, leurs propriétés physico-chimiques intrinsèques offrent la possibilité d'aborder les mécanismes de mobilisation géochimique ayant lieu dans le sédiment, fournissant des informations essentielles sur les processus sédimentaires et les conditions du milieu, mais également sur les flux particulaires entraînés par les masses d'eau et les processus sédimentaires des marges océaniques. Les deux chapitres développés ont mis en évidence que, lorsque combinés à une approche multi-paramètres, ces isotopes pouvaient constituer de très bons outils pour acquérir des informations sur les conditions environnementales passées. Il a été vu que leur mise en application dépendait du milieu considéré, du type de matériel étudié, de la période examinée et des objectifs poursuivis.

Le premier chapitre de cette thèse portait sur les sédiments provenant de la plaine abyssale centrale de la baie de Baffin et datés des derniers ~115 ka. Les études sédimentologiques de cette partie de la baie s'étaient vues restreintes jusque très récemment (Simon *et al.*, 2012), par le manque de marqueurs temporels. Pourtant, la baie de Baffin constitue une région essentielle à intégrer dans la recherche en paléoclimatologie/paléocéanographie étant donné sa localisation centrale par rapport aux grandes masses de glace et son rôle de bassin de transition entre l'océan Arctique et Atlantique. Ici, une chronostratigraphie établie récemment par Simon *et al.* (2012)

a permis d'étudier pour la première fois en haute résolution le comportement des isotopes de l'U et du Th dans ce bassin, l'unique étude antérieure ayant dû rester très partielle par manque d'information à ce sujet (voir Causse et Hillaire-Marcel, 1989).

Les compositions isotopiques en U et en Th permettent d'évaluer les sources, les flux et les processus géochimiques et sédimentaires. Toutefois, l'interprétation des signaux géochimiques en baie de Baffin s'est avérée peu aisée, principalement parce que la dynamique sédimentaire est complexe. Les concentrations et rapports d'activité U et Th ont mis en évidence des sources variées de sédiments détritiques, probablement liées à des décharges locales spécifiques à la dynamique des trois calottes de glace entourant la baie. Les faibles contenus en carbone organique enregistrés, l'absence de flux d'U diagénétique précoce et le signal de Mn rendent compte d'une faible productivité biologique passée de la colonne d'eau et de la persistance de conditions oxydantes dans les sédiments de surface, y compris durant l'Holocène. Des micro-gradients rédox établis le long de la séquence pourraient cependant avoir entraîné des remobilisations d'U diagénétiques tardives, générant notamment des incertitudes quant à l'estimation des valeurs du $(^{230}\text{Th}_{\text{xs}})_0$. Ces données au sujet du $(^{230}\text{Th}_{\text{xs}})_0$ semblent par ailleurs indiquer qu'au flux particulaire relativement abondant qui caractérise la période glaciaire se superpose des processus de "focusing", c'est-à-dire de redistribution sédimentaire syn- ou post-dépôt. A l'opposé, durant l'interglaciaire actuel, une perte par advection du $^{230}\text{Th}_{\text{xs}}$ laisse croire à une circulation de la masse d'eau profonde et à l'exportation partielle de $^{230}\text{Th}_{\text{xs}}$, s'effectuant très probablement à travers le courant de débordement du détroit de Davis vers la mer du Labrador.

Le deuxième chapitre de cette thèse portait sur l'analyse d'une séquence sédimentaire prélevée sur le bas du talus océanique du bassin du Labrador, proche de la sortie du détroit d'Hudson, et datée des derniers ~37 cal ka BP. L'étude se focalisait sur deux thèmes : (i) les processus sédimentaires régissant la mise en place des couches

relatives aux événements de Heinrich H2 et H1 et, (ii), la circulation océanique dans cette région de formation des eaux profondes froides, un des mécanismes majeurs de la boucle de circulation méridienne de renversement caractérisant l'océan Atlantique Nord.

L'utilisation des inventaires de $(^{230}\text{Th}_{\text{xs}})_0$ s'était déjà révélée fructueuse pour estimer les vitesses de dépôts des couches relatives aux événements de Heinrich à un site localisé plus au sud, à Orphan Knoll (Veiga-Pires et Hillaire-Marcel, 1999). Il s'agissait ici d'explorer à l'aide des mêmes outils un site d'étude localisé plus près de la sortie du détroit d'Hudson. Cette proximité permettait de recouvrir l'entièreté de l'intervalle, incluant les particules fines provenant de l'eau de fonte sous-glaciaire et le sédiment grossier largué par la fonte des icebergs. Cependant, des incertitudes ont été mises en évidence, rendant l'erreur sur l'estimation des vitesses de dépôt trop large et donc peu fiable.

Ensuite, il s'agissait d'utiliser le rapport $(^{231}\text{Pa}_{\text{xs}}/^{230}\text{Th}_{\text{xs}})_0$ pour évaluer l'évolution du débit des masses d'eau intermédiaires et profondes dans le bassin. Cependant, il a été montré que les flux en sédiment y sont complexes suite à la localisation : (i) en zone de marge continentale, proche du détroit d'Hudson, source majeure en icebergs et eaux sous-glaciaires lors d'épisodes de fonte de la calotte de glace des Laurentides, et (ii) en situation de confluence des différents courants en provenance de l'Atlantique du Nord-Est et de la baie de Baffin. Des flux importants de $(^{230}\text{Th}_{\text{xs}})_0$ ont été estimés dans certains intervalles et suggèrent des processus d'advection ou de "focusing". Ceux-ci sont spécialement élevés durant la période de déglaciation pour laquelle des flux détritiques massifs ont été reportés. Par ailleurs, le processus semble s'accélérer durant la deuxième moitié de l'Holocène, mais est cette fois probablement lié à la production de carbonates biogéniques. Par ailleurs, il a été montré que le sous-courant côtier de l'ouest pouvait avoir été suffisamment puissant pour avoir exporté le ^{231}Pa hors du bassin durant la majorité de l'intervalle étudié.

De manière générale, l'étude des sédiments profonds de bassins océaniques localisés en zone de marge continentale comporte des difficultés étant donné les flux sédimentaires et géochimiques complexes y opérant. Les données isotopiques en U, Th et Pa constituent des outils très puissants pour étudier la dynamique sédimentaire et sont peu documentés dans les régions de hautes latitudes. La large variabilité des sources et des flux, tant spatialement que temporellement, enregistrée dans les séquences étudiées est fortement liée à la dynamique glaciaire spécifique opérant le long des marges continentales. De plus, les remobilisations particulières syn- et post-sédimentaires sont fréquentes le long des marges de ces bassins et peuvent induire de nouveaux échanges géochimiques. La diffusion d'U à la suite de processus diagénétiques précoce et tardifs semble également se produire dans les séquences étudiées et peuvent influencer les signaux géochimiques originaux. Par ailleurs, des processus de diagénèse précoce semblent opérer dans les sédiments superficiels de la mer du Labrador, au contraire de la baie de Baffin. Cela s'expliquerait principalement par une productivité primaire très différente pour ces deux bassins.

Une fois tous les processus bien identifiés et dans la mesure du possible quantifiés, les excès initiaux de ^{231}Pa et de ^{230}Th peuvent être utilisés comme traceurs de la dynamique géochimique et particulière. Dans ce cadre, les résultats obtenus sur la séquence prélevée en baie de Baffin ont montré deux situations océanographiques contrastées entre la dernière période glaciaire et l'Holocène. En mer du Labrador par contre, les données de $(^{231}\text{Pa}/^{230}\text{Th}_{\text{xs}})_0$ indiquent qu'un courant profond fût suffisamment puissant pour exporter le ^{231}Pa de manière continue durant les derniers ~37 cal ka BP.

Des mesures de plus hautes résolutions dans les sédiments des deux bassins pourraient apporter des précisions supplémentaires. Cependant, des données d'autres traceurs géochimiques, tel le beryllium, en baie de Baffin notamment, l'analyse de métaux rédox-sensibles (e.g., manganèse) en mer du Labrador, et des mesures des

gradients rédox lors des carottages, pourraient s'avérer plus utiles pour compléter et valider les interprétations présentées dans cette thèse.

En définitive, en améliorant les connaissances et en démontrant l'efficacité des méthodes utilisées pour des problématiques spécifiques, ce travail contribue aux recherches paléoclimatiques et paléocéanographiques actuelles, tout en concourant au développement d'une base d'information à portée plus globale.

ANNEXE A

AUTHIGENIC, DETRITAL AND DIAGENETIC MINERALS IN THE LAGUNA POTROK AIKE SEDIMENT SEQUENCE

Laurence Nuttin^{1,2}, Pierre Francus^{2,3}, Michel Preda¹,
Bassam Ghaleb^{1,2} and Claude Hillaire-Marcel^{1,2}

¹Université du Québec à Montréal
CP. 8888, Succ. Centre-Ville, Montréal, QC, H3C 3P8, Canada

²GEOTOP Research Center
C.P. 8888, Succ. Centre-Ville, Montréal, QC, H3C 3P8, Canada

³Institut National de la Recherche Scientifique - Centre Eau, Terre, Environnement
490 rue de la Couronne, Québec, QC, G1K 9Q9, Canada

Keywords: XRD, clays, U-Th measurements, vivianite, paleoclimate, late Quaternary, Argentina, ICDP-PASADO

Article publié dans Quaternary Science Reviews (2013), 71, 109-118.

Abstract

The ~100 m-long Laguna Potrok Aike sediment sequence yielded a record spanning the Last Glacial period to the Holocene. This paper presents and discusses two aspects of the mineralogy of the lake. The first aspect is based on a semi-quantitative X-ray diffraction analysis of bulk and clay mineralogical assemblages. Minor mineralogical changes are observed throughout the glacial section suggesting relatively uniform sediment sources. The transition into the Holocene is characterized by increasing fluxes of endogenic calcite thought to relate to lower lake levels. The second aspect is based on analysis of uranium-series disequilibria in diagenetic vivianite from the glacial section. U-series ages were expected to yield minimum ages for the host-sediment. Unfortunately, very little authigenic U is present in vivianite grains. The low primary productivity of the lake and thus low organic carbon fluxes might have prevented the development of strong redox gradients at the water-sediment interface and thus reduced diagenetic U-uptake into the sediment. One vivianite sample, at a 56.9 m composite depth, yielded enough authigenic uranium to calculate a ^{230}Th -age of 29.4 ± 5.9 ka ($\pm 2\sigma$). This age is younger than the one indicated by the radiocarbon chronology. It is thus concluded that a relatively late diagenetic evolution of the U-Th system characterizes the recovered vivianite minerals. The authigenic U displays a very high excess in ^{234}U (over ^{238}U) with an activity ratio of 4.58 ± 0.58 ($\pm 2\sigma$). It suggests that it originates from the transfer of highly fractionated U from surrounding detrital minerals through very low U-content pore waters.

A.1. Introduction

Laguna Potrok Aike ($51^{\circ}58' S$, $70^{\circ}23' W$ in south-eastern Patagonia, Argentina) is one of the older maars of the Pali Aike Volcanic Field (PAVF), which is the most extensive maar field in South America. A $\sim 200 \text{ km}^2$ watershed contains a quasi-circular bowl-shaped crater $\sim 5 \text{ km}$ in diameter filled by a lake of $\sim 100 \text{ m}$ depth and $\sim 3.5 \text{ km}$ width (Zolitschka *et al.*, 2009). The crater was formed by an explosive eruption of rising magma contacting ground water, meltwater from ground ice or permafrost (Corbella, 2002; Figure 1). $^{40}\text{Ar}/^{39}\text{Ar}$ data of a basaltic clast from the phreatomagmatic tephra outcropping on the eastern side of the maar provided an age of $0.77 \pm 0.24 \text{ Ma}$ for the event (Zolitschka *et al.*, 2006; Figure 1). Seismic surveys indicate an exceptionally thick lacustrine sediment infill (up to 370 m in thickness) likely underlain by volcanoclastic deposits (Anselmetti *et al.*, 2009; Gebhardt *et al.*, 2011) which seemed to be protected from glacial erosion, deflation or desiccation (Zolitschka *et al.*, 2006). Therefore, Laguna Potrok Aike has the potential to preserve a continuous and high-resolution late Quaternary sediment record suitable to extract a long paleoenvironmental reconstruction for the Southern Hemisphere (Anselmetti *et al.*, 2009; Haberzettl *et al.*, 2007; Zolitschka *et al.*, 2006).

The Potrok Aike Maar Lake Sediment Archive Drilling Project (PASADO) was thus undertaken within the framework of the International Continental Scientific Drilling Program (ICDP). From the available material, a $\sim 100 \text{ m}$ -long composite record from the southern part of the lake was investigated using multiple tracers (Ohlendorf *et al.*, 2011). Our contribution to this project is twofold. First, using semi-quantitative X-ray diffraction analyses, we investigated mineralogical changes in order to document potential changes in soil hydrolysis conditions and in sediment sources through time, since minerals might reflect weathering conditions in the watershed (e.g., Chamley, 2000; Last, 2001; Moore and Reynolds, 1997; Thorez, 2003; Velde, 1992). Second, we analyzed U-series isotopes in authigenic and/or early diagenetic vivianite

$[\text{Fe}_3(\text{PO}_4)_2 \cdot 8\text{H}_2\text{O}]$, present at several depths in the composite sequence. High uranium concentrations were indeed reported in vivianite from similar settings (e.g., Lake Baikal; Fagel *et al.*, 2005). Here, the objective was to elaborate ^{230}Th -ages for this diagenetic mineral, as successfully done in a large array of diagenetic minerals from East African Lakes by Goetz and Hillaire-Marcel (1992).

A.2. Regional settings

The lake is located at 113 m above sea level (lake level in 2003; Ohlendorf *et al.*, 2011) in the older western part of the PAVF, ~300 km east of the Andes, ~85 km west of the city of Río Gallegos and ~80 km north of the Strait of Magellan. The PAVF consists of Pliocene (3.8 Ma) to Holocene (0.01 Ma) alkali-olivine basalts in a back-arc type of volcanism (Corbella, 2002). Scoria cones and plateau lavas formed during Late Miocene to Middle Pleistocene times are found in the catchment area (Coronato *et al.*, this issue) as well as fine-grained molasse-type fluvial sandstones of the Lower Miocene Santa Cruz formation. Furthermore, Pleistocene glaciations left behind fluvioglacial deposits and tills dated between 1.2 and 0.8 Ma (Zolitschka *et al.*, 2006). It seems that glaciers did not reach the catchment area during the last few glaciations (Coronato *et al.*, this issue; Mercer, 1976; Rabassa and Clapperton, 1990).

Laguna Potrok Aike is currently polymictic due to the strong southern hemispheric westerly winds (mean annual wind speed of ~7.4 m/s; Zolitschka *et al.*, 2006). This setting prevents the development of any ice cover during the austral winter and generates a non-stratified water column with oxygen-rich bottom waters. Today, subsaline conditions induce low productivity. The mean annual temperature recorded at the meteorological station of Río Gallegos is 7.4°C (Zolitschka *et al.*, 2006). Air masses passing over the Patagonian Andes produce a strong rainfall gradient from west to east and trigger semi-arid conditions in the Laguna Potrok Aike region with annual precipitation below 200 mm (Zolitschka *et al.*, 2006). However, precipitation was highly variable during recent millennia and mainly related to northward and southward shifts of the westerly winds (Zolitschka *et al.*, 2009). Today rainfalls are more often associated with easterly winds whereas westerly winds deliver fewer precipitations.

The crater has been permanently water-filled since 53.5 ka cal. BP (Gebhardt *et al.*, 2012) and has been mostly hydrologically closed (Zolitschka *et al.*, 2006), which caused a strong relationship between its water level and the evaporation/precipitation ratio (Haberzettl *et al.*, 2005; Ohlendorf *et al.*, this issue). This feature is demonstrated in the topography of the watershed by the presence of several lake level terraces above and below present day lake level on which surface runoff has created deep gullies (Anselmetti *et al.*, 2009). The highest subaerial terrace reached 21 m (above lake level in 2003) and corresponds to overflow conditions (Figure 1). Luminescence ages suggest that the lake level overflow occurred during the Last Glacial period around 17 ka cal. BP (Kliem *et al.*, this issue-b). Episodic inflows were linked to snowmelt events with the major inlet located on the western shore (Gebhardt *et al.*, 2012; Figure 1). More detailed descriptions of regional settings with regard to hydroclimatic variability and lake level fluctuations are provided by Gebhardt *et al.* (2012), Kliem *et al.* (this issue-b) and Ohlendorf *et al.* (this issue).

A.3. Materials and methods

A.3.1. Materials

The sediment cores were collected during the ICDP deep lake drilling expedition no. 5022 which was carried out from September to late November 2008. Coring was performed from a floating platform (GLAD800) using a hydraulic piston core (Ohlendorf *et al.*, 2011; Zolitschka *et al.*, 2009). A composite sequence of 106.08 m has been spliced from the best core sections from three different cores drilled at site 5022-2, located in the southern region of the lake (Zolitschka *et al.*, 2009; Kliem *et al.*, this issue-a; Figure 1). Further details on drilling and sampling are given in Ohlendorf *et al.* (2011). The record is mainly composed of lake mud, although the grain size of the lacustrine layers varies from clay to sand and gravel (Zolitschka *et al.*, 2009). Kliem *et al.* (this issue-a) established a lithostratigraphic description as outlined in Figure 4 and constructed the age model of the 106.08 m composite profile based on 58 radiocarbon dates yielding a basal age of 51.2 ka cal. BP.

Mineralogical analyses were performed on this composite sequence with a 16 cm sampling interval. Reworked intervals as visually identified by Kliem *et al.* (this issue-a) and resulting from mass movement deposits were excluded. These disturbed sediments are more frequent in the glacially derived sections, especially below ~50 m and account for ~54% of the 645 subsamples. A total of 270 samples were analyzed within this study interval between 0 to 96 m composite depth (mcd).

Visual examination of the cores reported dark blue layers containing concretions of vivianite (Figure 2a-e). A total of six samples (V1 to V5 and V5') were collected, respectively, at 56.9 mcd (V1, V5, V5'), 66.2 mcd (V2), 67.1 mcd (V3) and 78.6 mcd (V4).

A.3.2. Analytical procedures

A.3.2.1. Mineralogical analyses

Qualitative and semi-quantitative analyses of mineralogical assemblages were made using X-ray diffraction (XRD) following procedures described in Last (2001), Moore and Reynolds (1997) and Thorez (2003). Approximately 1 cm³ of dried bulk sediment was ground by hand with an agate mortar and pestle. The homogeneous powder was sieved at 63 µm with ultrapure water buffered to a pH of 7. The 0-63 µm fraction was then compacted on a circular slide using the back-side technique (i.e., as a non-oriented minerals powder) (Last, 2001). The sediment was scanned using a Siemens D5000™ diffractometer of CoKα1, 2 X-radiations ($\lambda = 1.76896$) and a Si detector between 2° and 50° 2θ angles. Qualitative and semi-quantitative estimates were based on peak identification and relative intensity measurements of their X-ray patterns using the Diffracplus EVA™ software (Figure 3). Peak position was determined using Bragg's law (Last, 2001; Moore and Reynolds, 1997; Thorez, 2003). Correction factors calculated from standards were automatically applied to intensity peaks by the EVA™ software and then semi-quantitative estimates of their relative abundances were based on the maximum intensity of each mineral peak (i.e., peak heights in counts per second) normalized to 100%. All mineral abundances were calculated from the corresponding principal diffraction peak except for quartz, for which a correction factor of 2.86 was applied to its second largest intensity diffraction peak. This correction allows to weight the crystallinity of quartz to that of the others minerals (Thorez, 2003). The analytical reproducibility of the method is approximately 5% ($\pm 1\sigma$).

In addition to the XRD analyses on the bulk fraction, clay analyses were also performed on the <2 µm fraction. From the <63 µm bulk fraction of 57 samples selected from the above series, approximately 1 cm³ was dispersed in distilled water

allowing the $<2 \mu\text{m}$ material to be separated by settling following Stokes's law (Moore and Reynolds, 1997). The $<2 \mu\text{m}$ fraction was then smeared on a clean glass slide to be analyzed using the diffractometer with the above settings, except that scanning was restricted to the $2\text{-}30^\circ 2\theta$ range. Each slide was measured after the following treatments: (1) drying (i.e., without further treatment), (2) ethylene-glycol solvation by vaporization in a desiccator for 24 hours, and (3) roasting at 500°C for 4 hours (Last, 2001; Moore and Reynolds, 1997; Thorez, 2003). Qualitative identification was based on the comparison of the three different X-ray diffractograms, since clays react specifically to each treatment. Semi-quantitative estimates of relative clay mineral abundances were based on peak maximum intensities (i.e., height of their respective peaks) on ethylene-glycol saturated patterns, summed to 100%. Clay fluxes could not be estimated due to their very low abundance and the small sample sizes allocated to this study. Smectite crystallinity was assessed from high-resolution measurements of the 17\AA peaks from ethylene-glycol diffractograms. The v/p ratio was then calculated in order to estimate the crystallinity of the smectites. This ratio corresponds to the 17\AA peak height (in counts per second) above the base of the low-angle side of the peak (v for "valley") and its height above background (p for "peak") (Biscaye, 1965; Thorez, 2003). When smectite peaks display v/p ratio values near 1, this suggests a well-defined crystallinity of the mineral. In contrast, values of v/p ratios tending to 0 indicate flatter peaks, which testify poorly developed smectite.

The bulk sediment XRD data set was statistically examined by Principal Component Analysis (PCA) using the Canoco v.4 software (ter Braak and Šmilauer, 1998). Trace minerals were excluded because semi-quantitative XRD estimates carry an uncertainty of 5%. Therefore, five minerals were only included in the statistical analysis and normalized to 100%.

A.3.2.2. U and Th isotope analyses

Vivianite samples V1 to V4 were analyzed in bulk sediment samples (Table 2). The cohesiveness of vivianite with the host sediment made its separation difficult, resulting in U and Th isotope analyses on mixed detrital-authigenic samples.

Sample V5 is a centimetric concretion from 56.9 mcd (Figure 2c). It was ultrasonicated for one hour to remove as much detrital material as possible from its surface. From this concretion a few grains were hand-picked and analyzed separately. These grains were referred to as sample V5' (Figure 2d).

U and Th separation and extraction were performed following the analytical procedures described in Edwards *et al.* (1987). Samples were analyzed on ~1 g of material of the four vivianite-detrital samples (V1 to V4), the entire cleaned concretion (V5), and all of the selected grains hand-picked from V5 (V5'). The samples were heated at 550°C for 2 hours to remove organic matter and facilitate further treatments. A ^{233}U - ^{236}U - ^{229}Th spike was added to the samples prior to an HCl/HNO₃/HF acid digestion. After this step, samples were dissolved in a HNO₃ solution. Then, in order to concentrate U and Th, a Fe(OH)₃ precipitate was created by adding a solution of ammonium hydroxide until obtaining a pH between 7 and 9. The precipitate was recovered by centrifugation and then dissolved in 6M HCl. U and Th were then separated from other constituents by ion exchange chromatography using resin columns. A Dowex AG1 X8 anion exchange resin was used in combination with ultra-pure H₂O and 6M HCl to isolate U and Th respectively. In order to remove any residual constituents, Th was purified using the same Dowex AG1 X8 anion exchange resin, and U using U/TEVA® resin. Finally, measurements were performed using a Triton Plus™ thermal-ionisation mass spectrometer (TIMS) in GEOTOP laboratories.

A.4. Results

A.4.1. Mineralogical assemblages

Bulk samples reveal that quartz accounts for the largest relative amount with an average of $57 \pm 9\%$ ($\pm 1\sigma$) (Table 1, Figure 3, 4). Feldspar is the second most abundant mineral with $18 \pm 6\%$, followed by the groups of smectite-chlorite and kaolinite-chlorite each presenting an average value of $7 \pm 5\%$. These clay minerals cannot be distinguished in bulk samples because their peaks overlap. Calcite is a distinct mineral in this sequence: nearly absent in the lower part of the core, it increases in the upper 15 m up to values as high as 42% (Figure 4). Trace quantities ($\leq 5\%$) of others minerals, such as amphibole, mica, zeolite and pyroxene have also been recorded. Cristobalite was observed with an average of $18 \pm 7\%$ in eight samples above 40 mcd (Figure 4). Likewise, monohydrocalcite, the hydrated form of calcite ($\text{CaCO}_3 \cdot \text{H}_2\text{O}$), was found in two intervals: between 9.7 and 9 mcd and between 8.5 and 6 mcd (Figure 4). Results of the PCA performed on bulk samples are reported in Figure 5. The two first principal components (i.e., PC1 and PC2) account for 80.2% of the total variance. PC1 shows an anti-correlation between calcite (0.91) and quartz (-0.81) and to a lesser extent feldspar (-0.35). PC2 splits quartz (-0.51) and calcite (-0.41) from the clay minerals groups of kaolinite-chlorite (0.87) and smectite-chlorite (0.77) whereas the weight of feldspar is not significant (-0.06). Another way to report the results obtained from the PCA is to plot the scores of principal components with depth (or time) in order to highlight synthetic variations throughout the profile (Figure 6). Results of the two first principal components show a distinct change at ~ 12 ka cal. BP (i.e., ~ 15 mcd) when calcite became the dominant mineral.

The analysis of the clay fraction ($< 2 \mu\text{m}$) led to the identification of four clay species. These are smectite with an average of $41 \pm 12\%$ ($\pm 1\sigma$) in relative abundance of the total clay fraction, followed by chlorite contributing for $25 \pm 8\%$, illite with 22

$\pm 4\%$, and finally kaolinite with $12 \pm 3\%$. The histogram of cumulative percentages of the clay fraction (Figure 7) shows that smectite increases in the upper 15 m of the core, whereas chlorite and illite tend to be more abundant in the underlying section. Kaolinite displays a steady profile throughout the whole sequence except a sharp increase at ~ 18 mcd ($\sim 26\%$). Moreover, smectite is mainly well crystallised with a v/p ratio average of 0.5 and a slight increase in the Holocene with values as high as 0.9 (Figure 7).

A.4.2. U and Th data

In order to confirm the visual identification of vivianite (Figure 2a-e), we performed complementary XRD and scanning electron-microscope energy-dispersive spectroscopy (SEM-EDS) analyses on bulk vivianite (V1 to V4). XRD analyses revealed the presence of vivianite ($d(001)=6.73 \text{ \AA}$) accounting for 1 to 3% in relative abundance of bulk samples (Figure 8), and SEM-EDS measured high percentages of Fe and P in the grains (Figure 9).

The concentrations and activity ratios of U and Th obtained from the geochemical analyses on the vivianite concretion (V5), the isolated grains (V5') and the four vivianite-detrital samples (V1 to V4) are listed in Table 2. Contrary to expectations, the vivianite samples do not show high U concentrations as recorded in the vivianite from Lake Baikal (total U concentrations between 0.82 and $260 \mu\text{g g}^{-1}$; Fagel *et al.*, 2005). U concentrations in the mixed detrital-authigenic samples are slightly above $1 \mu\text{g g}^{-1}$ for samples V1 to V4. The ‘cleaned’ vivianite concretion (V5) and the selected grains (V5') display much lower U concentrations, with values of 0.286 ± 0.001 and $0.213 \pm 0.001 \mu\text{g g}^{-1}$ respectively, thus indicating that most of the U present in the mixed samples might be simply inherited with detrital fractions. In contrast, Th concentrations are relatively high, with values averaging $5 \mu\text{g g}^{-1}$ for samples V1 to

V4. The Th values for the concretion and the selected grains are much lower with values around $1 \mu\text{g g}^{-1}$, still indicating some contamination by detrital material.

A.5. Discussion

A.5.1. Paleoenvironmental changes

Mineralogical abundances (Figure 4, 7) and principal component score plots (Figure 6) indicate a marked change at \sim 15 mcd which corresponds to \sim 12 ka cal. BP based on the age-depth model (Kliem *et al.*, this issue-a). As already discussed in earlier studies (e.g., Haberzettl *et al.*, 2007; Zolitschka *et al.*, 2009), this change corresponds to the transition from glacial to interglacial conditions. Calcite is consistently absent or in very low quantities prior to 12 ka cal. BP whereas it is almost always present in relatively large amounts after 12 ka cal. BP (Figure 4). As no carbonaceous rocks are present in the watershed, the Ca^{2+} ions in the lake water mostly originate from the weathering of basaltic rocks in the catchment area (Haberzettl *et al.*, 2005). These authors also concluded that calcite precipitation occurred during phases of a low lake level or lake level lowering when calcite saturation was reached in the water column. Accordingly, no calcite precipitation occurred when the lake level was rising or was high, reflecting the dilution of the water column. Cold temperatures of the glacial period also prevented from calcite precipitation. Likewise, the geochemical approach performed on the composite core PTA03/12+13 (Figure 1) by Haberzettl *et al.* (2007) also showed that monohydrocalcite, a type of calcite precipitated by bacterial activity at high salt concentrations, can be used as a lake level proxy, since it is linked to enhanced Ca^{2+} concentration resulting from a reduced lake water volume. Hence, the monohydrocalcite presence between 6 and 9.7 mcd indicates a pronounced low lake level between 8.4 and 7.1 ka cal. BP. Moreover, seismic data (Anselmetti *et al.*, 2009; Gebhardt *et al.*, 2011) reveal that the lake level dropped to a depth of \sim 33 m below the lake level of 2003 during this interval. Low lake level phases might follow drier and/or warmer climatic conditions. Other indicators point also to a low lake level around this period (e.g., Haberzettl *et al.*, 2007: geochemical data; Massaferro *et al.*, this issue: diatoms and chironomids; Wille *et al.*, 2007: pollen and diatoms).

Quartz abundance decreased during the Holocene compared to the glacial period. Quartz flux varied roughly proportionally to sedimentation rates (see age model proposed by Kliem *et al.*, this issue-a). The quartz polymorph cristobalite which is present with relatively high percentages but in few samples only, is a mineral frequently found in volcanic rocks. It is formed at atmospheric pressure, between 1470°C and its melting point 1627°C, but it can crystallize and persist in a metastable state at lower temperatures (Downs and Palmer, 1994). The presence of cristobalite is likely related to volcanism in the region, brought to the lake after weathering since basaltic deposits are present in the catchment area. Feldspars appear with relatively higher concentrations in the glacial interval, as well as both clay groups (kaolinite-chlorite and to a lesser extent smectite-chlorite). During the Late Glacial chlorite and smectite constitute the two main clay groups in relative abundance, smectite being the most abundant clay in the Laguna Potrok Aike sediments particularly in the Holocene (Figure 7). Both originate from weathering of mafic rocks (smectite after an additional degree of alteration) which are abundant in the catchment basin and preferentially yield this type of clay (Chamley, 2000; Thorez, 2003). Smectite can also derive from authigenesis processes. High v/p ratios indicate authigenetic smectite, while low ratios point to pedogenetic-derived smectites (Thorez, 2003). Hence, higher v/p values in the Holocene tend to indicate stronger authigenesis. However, such higher Holocene v/p values might also relate to an increase in the smectite abundance rather than to a change in its genetic origin (Figure 7). Since clay fluxes cannot be estimated, it is difficult to assess if this relative increase of smectite is due to increased hydrolysis in the watershed or to intensification of authigenic processes in the water column or to both. Amphibole, zeolite, mica and pyroxene concentrations are too low to provide a basis for any interpretation of their relative variability.

Results from the PCA on the five main assemblages (Figure 5) highlight three distinct mixing end-members: detrital (containing quartz and feldspar), endogenic (composed

exclusively of calcite) and a third one containing the clays (smectite, chlorite and kaolinite) ensuing from weathering processes. Feldspar is more associated to the PC1 axis than quartz, and tends towards the clay mineral end-member on PC2. This behaviour characterizes an environment in which feldspar is subjected to more intense chemical alteration than quartz.

PC1 shows a relatively abundant detrital input in the glacial section of the sequence (Figure 6). This detrital fraction is replaced by endogenic calcite after ~12 ka cal. BP. The clays are also more abundant in the section deposited prior to ~12 ka cal. BP, possibly indicating higher gelification and/or eolian supplies under periglacial conditions (e.g., Basile *et al.*, 1997; Gaiero, 2007; Sugden *et al.*, 2009).

For the past 16 ka in the PTA03/12+13 sequence, Haberzettl *et al.* (2007) suggested wetter conditions from 16 to 8.7 ka cal. BP (ending Last Glacial to early Holocene) interrupted by a dry and warm phase from 13.1 to 11.4 ka cal. BP. Drier conditions would prevail from 8.7 ka cal. BP until now. Mineralogical data confirms this overall pattern. The 13.1 to 11.4 ka cal. BP dry and warm period corresponds to a calcite peak (Figure 4) possibly indicating a drier and/or warmer period. During the glacial period, the slightly higher abundance of quartz, feldspars and clay groups might result from an increase of gelification processes and/or higher eolian supplies in the periglacial environment. Two intervals at ca. 50 and 46 ka cal. BP within this glacial period present higher smectite contents (Figure 7). The v/p ratio is stable in the earlier interval (~50 ka cal. BP) and increases in the second (~46 ka cal. BP). Higher v/p ratio might explain the increase of smectite content as an intensification of the authigenic process. Both intervals also depict higher clay abundances according to the PCA analysis (Figure 5, 6). Taken alone, these mineralogical variations are difficult to interpret. However, they can be understood in the light of the biochemical proxies collected by Hahn *et al.* (this issue) suggesting higher lake level and increased productivity during these two time intervals. Increased clay content would result from

more frequent snowmelt events in a warmer environment and in a more distal location (due to higher lake level). Higher relative smectite abundance could be explained as resulting from chemical alteration rather than from gelification, while higher v/p could result from stronger authigenesis in a more productive lake.

A.5.2. U-Th "dating" of vivianite

Vivianite is formed either by precipitation in the water column or by diagenetic processes within the sediment. Well-oxygenated bottom waters tend to produce more ferric hydroxides (since ferrous cations are more soluble than ferric cations) which can co-precipitate with P released from pore waters by forming ferrosoferric hydroxyphosphates at the water-sediment interface (Fagel *et al.*, 2005; Nriagu and Dell, 1974; Taylor *et al.*, 2008). Any subsequent increase in reducing conditions will then give rise to transformation of such complexes into vivianite. Such a diagenetic process of precipitating vivianite seems to correspond to the polymictic conditions prevailing in Laguna Potrok Aike rather than vivianite formation in the water column.

Low concentrations of U combined with high concentrations of Th indicate that the vivianite from Laguna Potrok Aike does not contain much authigenic U (Table 2). Most of the U found in samples V1 to V4 seems detritic in origin despite its slight excess in ^{234}U vs. ^{238}U , which is likely due to some uptake of a highly fractionated diagenetic U (see below). With their Th/U mass ratio of about 4, the U-carrying detritic minerals that contaminate vivianite have values reported for volcanic rocks from the area (Demant *et al.*, 2007). The less-contaminated concretion (V5) and the selected vivianite grains (V5') yielded some authigenic U as indicated by their much higher excess in ^{234}U vs. ^{238}U and lower ^{232}Th content. Using the $^{238}\text{U}/^{232}\text{Th}$ ratio as detrital index (Ludwig and Paces, 2002) and assuming that the mean isotopic composition of V2 to V4 provides a fair proxy of the isotopic composition of the detrital contaminant ($^{238}\text{U}/^{232}\text{Th} = 0.719 \pm 0.008$; $^{234}\text{U}/^{232}\text{Th} = 0.804 \pm 0.010$;

$^{230}\text{Th}/^{232}\text{Th} = 0.889 \pm 0.013$), one may estimate the $^{230}\text{Th}/^{234}\text{U}$ and $^{234}\text{U}/^{238}\text{U}$ ratios linked to the authigenic fraction of U present in sample V5 (Table 3). V1 and V5' were not included in the calculation of the average detrital fraction because of their slightly higher authigenic uranium. Unfortunately, the attempt to use the $^{238}\text{U}/^{232}\text{Th}$ ratio to decipher the detrital vs. authigenic U-fractions results in too large uncertainties to provide reliable interpretations. Thus V5 seems to be the only sample suitable to estimate a ^{230}Th -age and an isotopic composition ($^{234}\text{U}/^{238}\text{U}$) of the authigenic U-fraction. Values of 29.4 ± 5.9 ka and 4.58 ± 0.58 ($\pm 2\sigma$) are obtained. The strong excess in ^{234}U suggests that the highly-fractionated U has been transferred from surrounding detrital minerals through a U-poor pore water medium. Such relative enrichments in ^{234}U recoiled from detrital grains are characteristic of low Eh and U-depleted pore waters (e.g., Andrews and Kay, 1982). Noteworthy is the fact that the detrital correction made using data from V2 to V4 bypasses the fact that these contain a small fraction of authigenic U, as indicated by their excess in ^{234}U vs. ^{238}U . Estimates of authigenic fractions in U-series isotopes are thus slightly lower than in reality resulting consequently in an underestimated ^{230}Th -age.

The low U content in the vivianite from Laguna Potrok Aike suggests reduced diagenetic U-fluxes in the sediment. U-series analysis of vivianite grains from Lake Jacques Cartier in eastern Canada (47°N , 71°W) and from the Laptev Sea (76°N , 125°E) (own unpublished data) yielded concentrations of authigenic U in the range of those observed in the sediments of Laguna Potrok Aike (U total concentration values between 0.805 and $1.649 \mu\text{g g}^{-1}$ in three vivianite samples from Lake Jacques Cartier and a value of $0.333 \pm 0.002 \mu\text{g g}^{-1}$ was obtained in the sample from the Laptev Sea). Thus, the high U-content reported for vivianite from Lake Baikal by Fagel *et al.* (2005) seems more an exception rather than a rule.

Nonetheless, the ^{230}Th -age estimate for the authigenic U in sample V5 constitutes a lower age limit for the embedding sediment due to both the diagenetic origin of the

carrier mineral and the fact that this age is an underestimation of the true vivianite age, as discussed above. It is 11.7 ± 5.9 ka younger than the model-age estimated by Kliem *et al.* (this issue-a). Assuming that the model-age stands strong, one may further hypothesize: i) a relatively late diagenetic precipitation of the carrier-vivianite, ii) a more or less continuous growth of vivianite with decreasing precipitation rates through time, iii) an open system with respect to U, allowing it to be continuously trapped in vivianite with decreasing rates through time, or iv) a combination of these processes.

A.6. Conclusion

The mineralogical study of Laguna Potrok Aike sediments confirms and supports the paleoenvironmental reconstruction constructed by other members of the PASADO science team using other indicators. The low variability of mineralogical assemblages within the glacial sequence suggests moderate environmental changes throughout this interval (~ 51 to 12 ka cal. BP). The slightly higher bulk and clay mineralogical abundance found during this period might correspond to a slight increase of gelification processes and/or higher eolian supplies under periglacial conditions. The shift in the precipitation/evaporation ratio at the Holocene-Last Glacial transition is marked by the addition of an authigenic calcite component. Its formation is related to lower lake levels, therefore probably to dryer and/or warmer Holocene climatic conditions. A higher crystallinity of smectite is observed during this interval and might correspond to some authigenic production or to a more effective hydrolysis in soils or to both.

An attempt to date the only diagenetic mineral, vivianite, using U-series is not conclusive. Low U-fluxes in the embedding sediment result in vivianite grains with too low co-precipitated U. Moreover, the formation of vivianite seems to be a long lasting process after burial and does not permit estimating precise and reliable diagenetic precipitation ages.

Acknowledgments

This research used samples and/or data provided by the International Continental Scientific Drilling Program (ICDP) in the framework of the “Potrok Aike Maar Lake Sediment Archive Drilling Project” (PASADO). Funding for drilling was provided by the ICDP, the German Science Foundation (DFG), the Swiss National Funds (SNF), the Natural Sciences and Engineering Research Council of Canada (NSERC), the Swedish Vetenskapsrådet (VR) and the University of Bremen. Special acknowledgments are due to the PASADO science team (http://www.icdp-online.org/front_content.php?idcat=1494), to financial support from NSERC-Special Research Opportunity for graduate scholarships to Laurence Nuttin and from FQRNT for infrastructure support of GEOTOP laboratories. We particularly owe thanks to Nathalie Fagel (Université de Liège) and one anonymous reviewer for their constructive and helpful comments on an earlier version of this paper.

References

- Andrews, J. N., and R. L. F. Kay (1982), $^{234}\text{U}/^{238}\text{U}$ activity ratios of dissolved uranium in groundwaters from a Jurassic Limestone aquifer in England, *Earth and Planetary Science Letters*, 57, 139-151.
- Anselmetti, F. S., D. Aritzegui, M. De Batist, C. A. Gebhardt, T. Haberzettl, F. Niessen, C. Ohlendorf, and B. Zolitschka (2009), Environmental history of southern Patagonia unravelled by the seismic stratigraphy of Laguna PotrokAike, *Sedimentology*, 56, 873-892.
- Basile, I., F. E. Grousset, M. Revel, J. Robert Petit, P. E. Biscaye, and N. I. Barkov (1997), Patagonian origin of glacial dust deposited in East Antarctica (Vostok and Dome C) during glacial stages 2, 4 and 6, *Earth and Planetary Science Letters*, 146, 573-589.
- Biscaye, P. E. (1965), Mineralogy and sedimentation of recent deep-sea clay in the Atlantic ocean and adjacent seas and oceans, *Geological Society of America Bulletin*, 76, 803-832.
- Chamley, H. (2000), Bases de sédimentologie, second ed., 178 pp., Dunod, Paris.
- Corbella, H. (2002), El campo volcano-tectonico de Pali Aike, Geología y Recursos Naturales de Santa Cruz. Asociación Geológica Argentina., I-18, 285-301.
- Coronato, A., B. Ercolano, H. Corbella, and P. Tiberi (this issue), Glacial, fluvial and volcanic 1 landscape evolution in the Laguna PotrokAike maar area, southernmost patagonia, Argentina, *Quaternary Science Reviews*.
- Demant, A., M. Suárez, and R. De la Cruz (2007), Geochronology and petrochemistry of Late Cretaceous-(?)Paleogene volcanic sequences from the eastern central Patagonian Cordillera (45° - $45^{\circ}40'$ S), *Revista Geológica de Chile*, 34(1), 3-21.
- Downs, R. T., and D. C. Palmer (1994), The pressure behavior of acristobalite, *American Mineralogist*, 79, 9-14.
- Edwards, R. L., J. H. Chen, and G. J. Wasserbburg (1987), ^{238}U ^{234}U ^{230}Th ^{232}Th systematics and the precise measurement of time over the past 500,000 years, *Earth and Planetary Science Letters*, 81, 175-192.
- Fagel, N., L. Y. Alleman, L. Granina, F. Hatert, E. Thamo-Bozso, R. Cloots, and L. André (2005), Vivianite formation and distribution in Lake Baikal sediments, *Global and Planetary Change*, 46, 315-336.

Gaiero, D. M. (2007), Dust provenance in Antarctic ice during glacial periods: From where in southern South America?, *Geophysical Research Letters*, 34, L17707.

Gebhardt, A. C., M. De Batist, F. Niessen, F. S. Anselmetti, D. Ariztegui, T. Haberzettl, C. Kopsch, C. Ohlendorf, and B. Zolitschka (2011), Deciphering lake and maar geometries from seismic refraction and reflection surveys in Laguna Potrok Aike (southern Patagonia, Argentina), *Journal of Volcanology and Geothermal Research*, 201, 357–363.

Gebhardt, A. C., C. Ohlendorf, F. Niessen, M. De Batist, F. S. Anselmetti, D. Ariztegui, P. Kliem, S. Wastegard, and B. Zolitschka (2012), Seismic evidence of up to 200 m lake-level change in Southern Patagonia since Marine Isotope Stage 4, *Sedimentology*, 59, 1087–1100.

Goetz, C., and C. Hillaire-Marcel (1992), U-series disequilibria in early diagenetic minerals from Lake Magadi sediments, Kenya: Dating potential, *Geochimica et Cosmochimica Acta*, 56, 1331–1341.

Haberzettl, T., M. Fey, A. Lücke, N. Maidana, C. Mayr, C. Ohlendorf, F. Schäbitz, G. H. Schleser, M. Wille, and B. Zolitschka (2005), Climatically induced lake level changes during the last two millennia as reflected in sediments of Laguna Potrok Aike, southern Patagonia (Santa Cruz, Argentina), *Journal of Paleolimnology*, 33, 283–302.

Haberzettl, T., H. Corbella, M. Fey, S. Janssen, A. Lücke, , C. Mayr, C. Ohlendorf, F. Schäbitz, G.H. Schleser, M. Wille, S. Wulf and B. Zolitschka (2007), Lateglacial and Holocene wet-dry cycles in southern Patagonia: chronology, sedimentology and geochemistry of a lacustrine record from Laguna Potrok Aike, Argentina, *The Holocene*, 17, 297–310.

Hahn, A., P. Kliem, C. Ohlendorf, B. Zolitschka and P. Rosén (this issue), Climate induced changes as registered in inorganic and organic sediment components from Laguna Potrok Aike (Argentina) during the past 51 ka, *Quaternary Science Reviews*.

Kliem, P., D. Enters, A. Hahn, C. Ohlendorf, A. Lisé-Pronovost, G. St-Onge, S. Wastegård, and B. Zolitschka (this issue-a), Lithology, radiocarbon chronology and sedimentological interpretation of the lacustrine record from Laguna Potrok Aike, southern Patagonia, *Quaternary Science Reviews*.

Kliem, P., J.-P. Buylaert, A. Hahn, C. Mayr, A. Murray, C. Ohlendorf, D. Veres, S. Wastegård, and B. Zolitschka (this issue-b), Magnitude, geomorphologic response and climate links of lake level oscillations at Laguna Potrok Aike, Patagonian steppe (Argentina), *Quaternary Science Reviews*.

- Last, W. M. (2001), Mineralogy analysis of lake sediments, in Tracking Environmental Change Using Lake Sediments, edited by W. M. Last and J. P. Smol, pp. 143-187, Kluwer Academic Publishers, Dordrecht, The Netherlands.
- Ludwig, K. R., and J. B. Paces (2002), Uranium-dating of pedogenic silica and carbonate, Crater Flat, Nevada, *Geochimica et Cosmochimica Acta*, 66(3), 487-506.
- Mercer, J. H. (1976), Glacial history of southernmost south America, *Quaternary research*, 6, 125-166.
- Moore, D. M., and J. C. Reynolds (1997), X-Ray Diffraction and the Identification and Analysis of Clay Minerals, Oxford University Press, New York.
- Nriagu, J. O., and C. I. Dell (1974), Diagenetic formation of iron phosphate in recent lake sediments, *American Mineralogist*, 59, 934-946.
- Ohlendorf, C., C. Gebhardt, A. Hahn, P. Kliem, B. Zolitschka, and t. P. s. team (2011), The PASADO core processing strategy — A proposed new protocol for sediment core treatment in multidisciplinary lake drilling projects, *Sedimentary Geology*, 239, 104-115.
- Ohlendorf, C., M. Fey, C. Gebhardt, T. Haberzettl, A. Lücke, C. Mayr, F. Schäbitz, M. Wille, and B. Zolitschka (this issue), Mechanisms of lake-level change at Laguna PotrokAike (Argentina) - Insights from hydrological balance calculations, *Quaternary Science Reviews*.
- Rabassa, J., and C. M. Clapperton (1990), Quaternary glaciations of the southern Andes, *Quaternary Science Reviews*, 9, 153–174.
- Sugden, D. E., R. D. McCulloch, A. J.-M. Bory, and A. S. Hein (2009), Influence of Patagonian glaciers on Antarctic dust deposition during the last glacial period, *Nature Geoscience*, 2, 281-285.
- Taylor, K. G., K. A. Hudson-Edwards, A. J. Bennett, and V. Vishnyakov (2008), Early diagenetic vivianite $[Fe_3(PO_4)_2 \cdot 8H_2O]$ in a contaminated freshwater sediment and insights into zinc uptake: A μ -EXAFS, μ -XANES and Raman study, *Applied Geochemistry*, 23, 1623–1633.
- ter Braak, C. J. F., and P. Šmilauer (1998), CANOCO Reference Manual and User's Guide to Canoco for Windows: Software for Canonical Community Ordination (version 4), 352 pp., Ithaca, NY, USA.
- Thorez, J. (2003), L'argile, minéral pluriel, *Bulletin de la Société Royale des Sciences de Liège*, 72(1), 19-70.

Velde, B. (1992), Introduction to clay minerals: chemistry, origins, uses and environmental significance, 198 pp., Chapman & Hall, London.

Wille, M., N.I. Maidana, F. Schäbitz, M. Fey, T. Haberzettl, S. Janssen, A. Lücke, C. Mayr, C. Ohlendorf, G.H. Schleser and B. Zolitschka (2007), Vegetation and climate dynamics in southern South America: The microfossil record of Laguna Potrok Aike, Santa Cruz, Argentina, *Review of Palaeobotany and Palynology*, 146, 234–246.

Zolitschka, B., F. Anselmetti, D. Ariztegui, H. Corbella, P. Francus, C. Ohlendorf, F. Schäbitz, and the PASADO Scientific Drilling Team (2009), The Laguna Potrok Aike Scientific Drilling Project PASADO (ICDP Expedition 5022), *Scientific Drilling*, 8, 29-34.

Zolitschka, B., F. Schäbitz, A. Lücke, G. Clifton, H. Corbella, B. Ercolano, T. Haberzettl, N.I. Maidana, C. Mayr, C. Ohlendorf, G. Oliva, M.M. Paez, G.H. Schleser, J. Soto, P. Tiberi and M. Wille (2006), Crater lakes of the Pali Aike Volcanic Field as key sites of paleoclimatic and paleoecological reconstructions in southern Patagonia, Argentina, *Journal of South American Earth Sciences*, 21, 294–309.

Figures

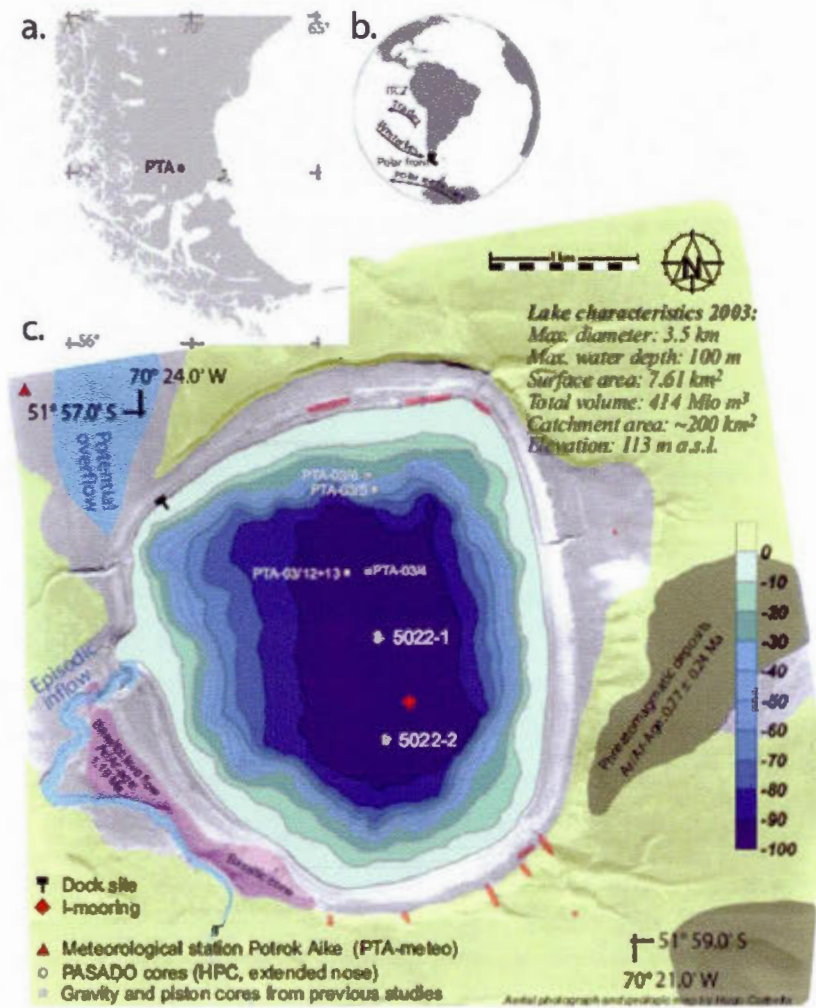


Figure 1 – Location, bathymetry and description of Laguna Potrok Aike. (a) Location of Laguna Potrok Aike (PTA) in southern Patagonia. (b) Schematic circulation of main atmospheric currents in southern America. (c) Aerial photograph of the immediate catchment area of Laguna Potrok Aike, bathymetry, core location and some site characteristics (modified after Ohlendorf *et al.*, this issue).

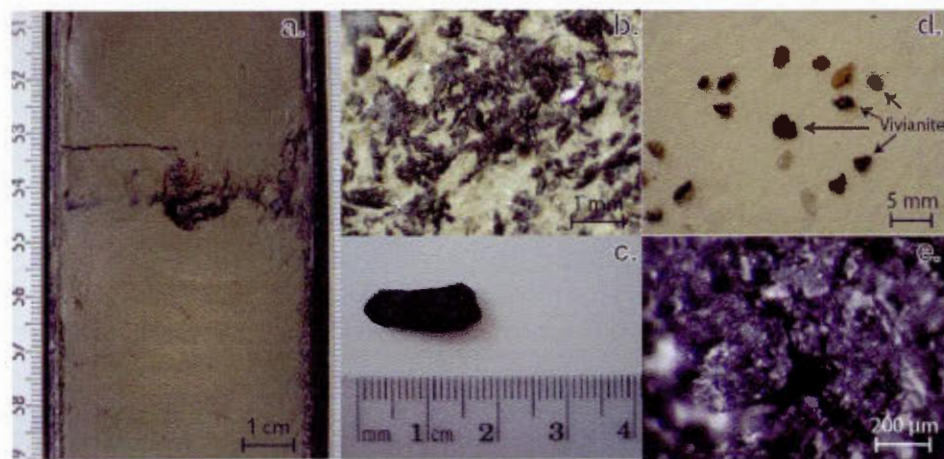


Figure 2 – Photographs of vivianite samples. (a) Dark blue layer of vivianite found at 56.9 mcd. (b) Vivianite crystals with detrital fraction. (c) Centimetric vivianite concretion after ultrasonic cleaning (V5). (d) Hand-picked sample V5'. (e) Binocular view of 'cleaned' vivianite.

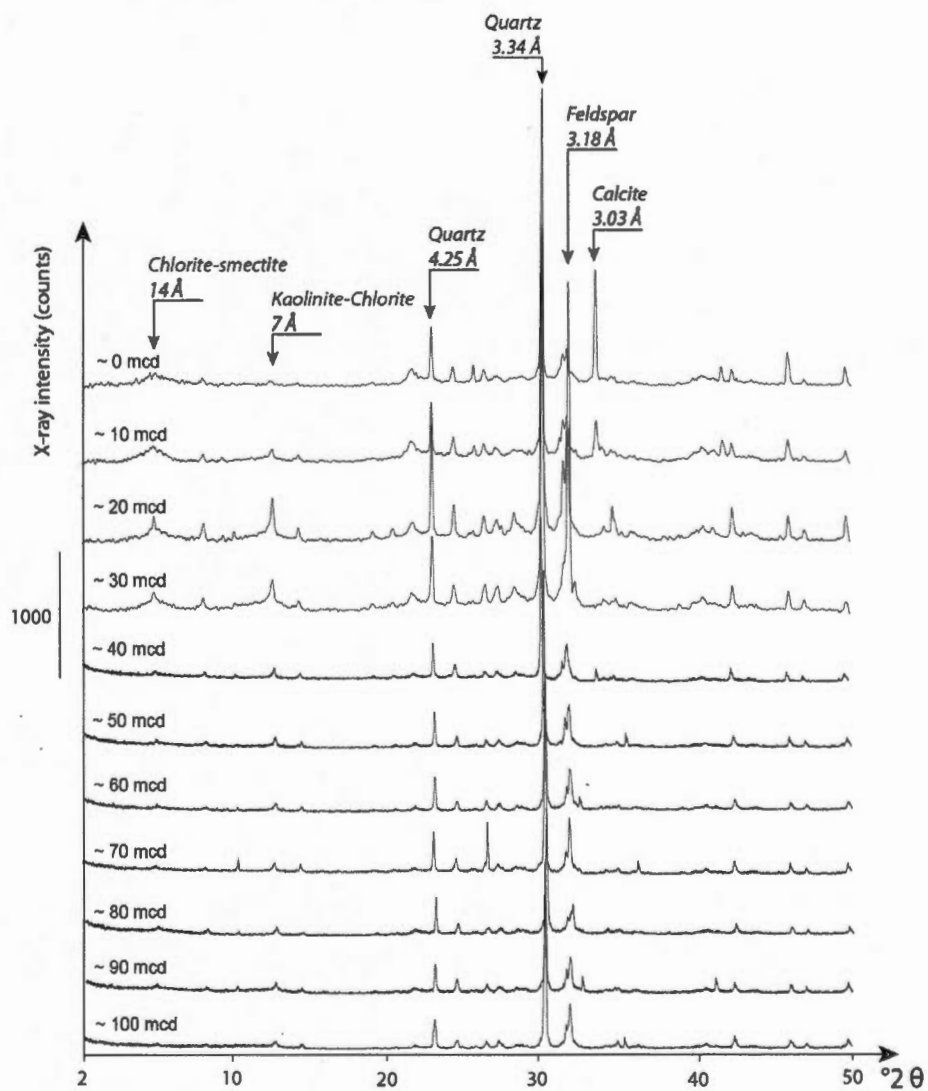


Figure 3 – Evolution of the mineralogy according to X-ray patterns of the $<63 \mu\text{m}$ fraction in 10 m steps for the Laguna Potrok Aike sediment sequence. Peak positions of five most abundant mineral assemblages are reported in angstroms (\AA).

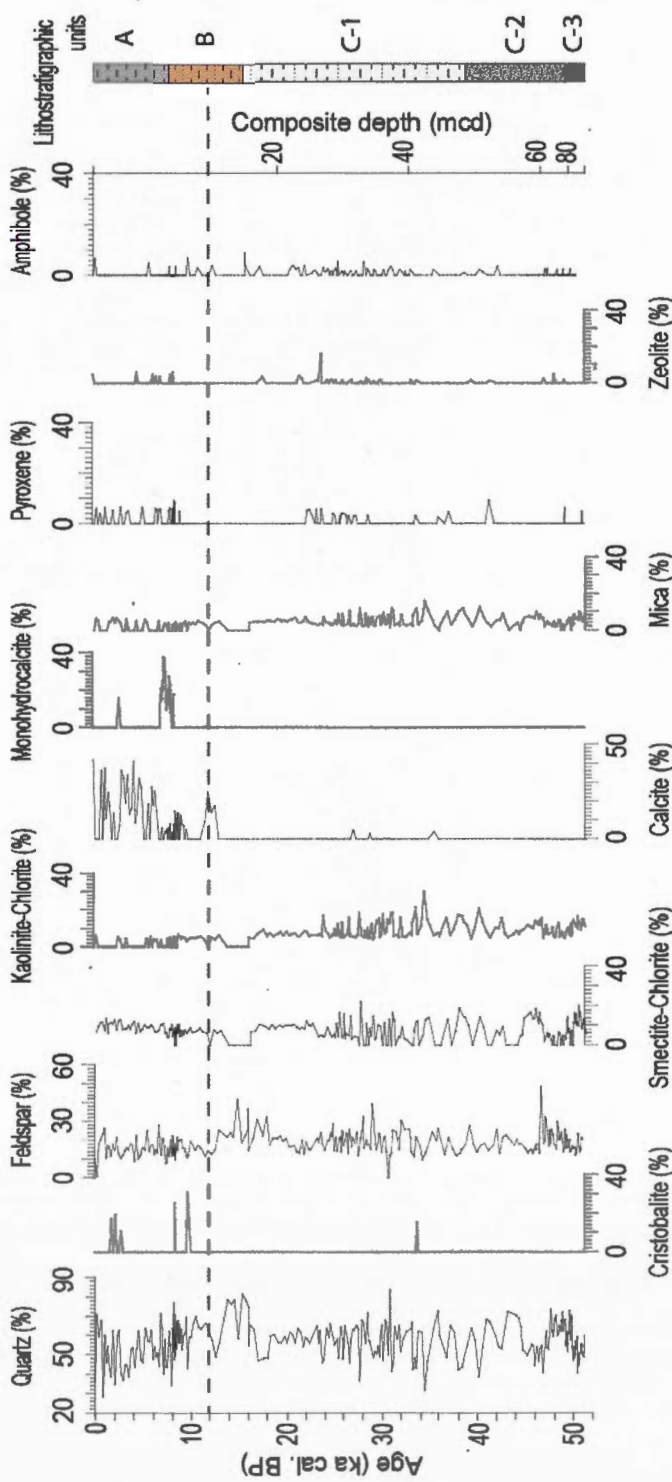


Figure 4 – Semi-quantitative mineral abundances vs. age and composite depth for major minerals with lithostratigraphy according to Kliem *et al.* (this issue-a). The dashed line marks 12 ka cal. BP. Unit A (0-9 mcd): Pelagic laminated silts prevail; almost no mass movement deposits; relatively high amount of calcite crystals; unit B (9-19 mcd): Dominance of pelagic laminated silts intercalated with thin fine sand and coarse silt layers; normal graded units and ball and pillow structures occur; high content of plant macro remains and gastropods; a few calcite crystals occur; unit C-1 (19-40 mcd): Dominance of pelagic laminated silts intercalated with thin fine sand and coarse silt layers; normal graded units and ball and pillow structures occur; unit C-2 (40-82 mcd): Dominance of normal graded units of ball and pillow structures among pelagic laminated silts intercalated with thin fine sand and coarse silt layers; unit C-3 (82-106 mcd): Dominance of normal graded units, ball and pillow structures, sand and gravel layers; a few pelagic laminated silts intercalated with thin fine sand and coarse silt layers occur.

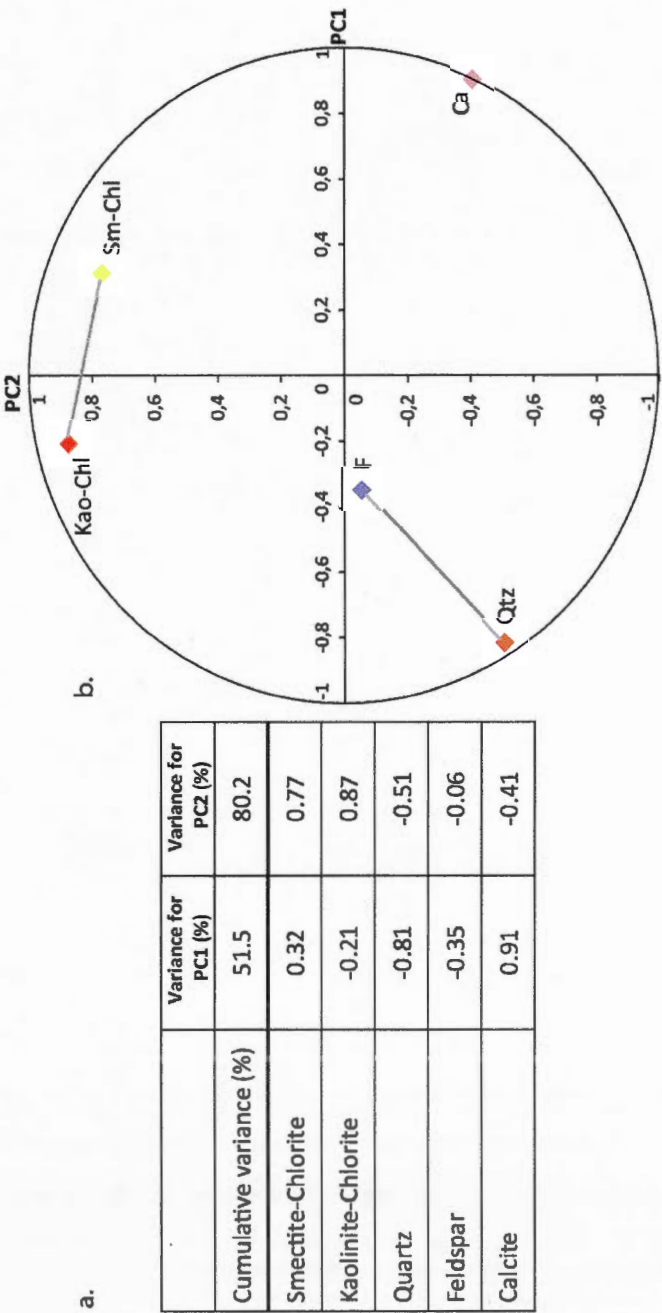


Figure 5 – Results from PCA on the five main mineralogical assemblages (fraction <63 µm). (a) Correlation matrix of major mineralogical assemblages with the two first components; (b) Correlation circle.

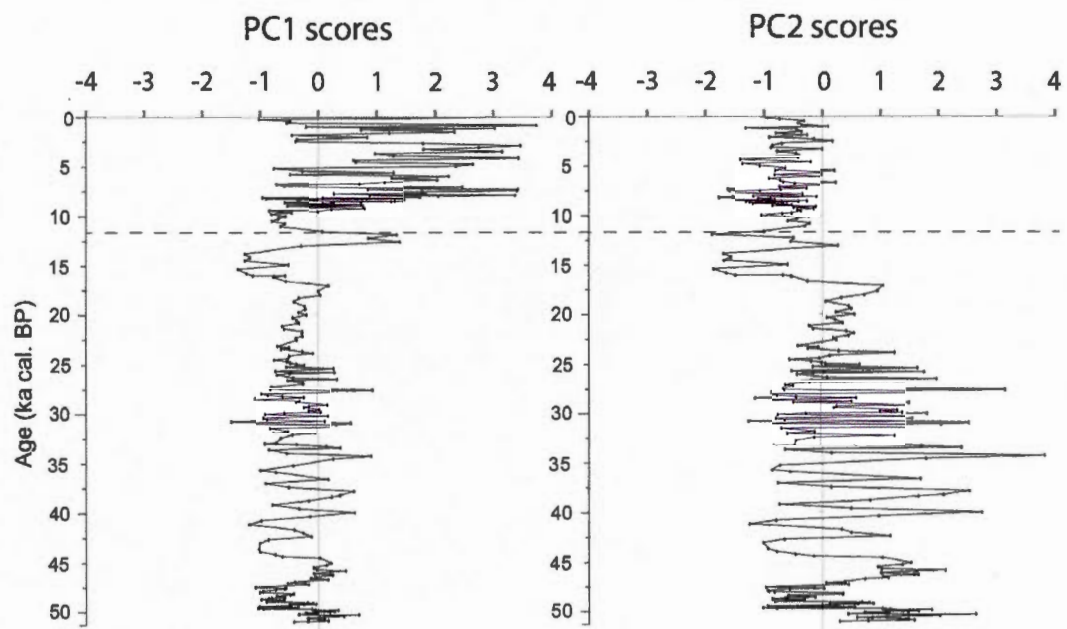


Figure 6 – Scores of PC1 (left) and PC2 (right) of the five main mineralogical assemblages (fraction <63 µm) plotted vs ages according to Kliem *et al.* (this issue-a). The dashed line marks 12 ka cal. BP.

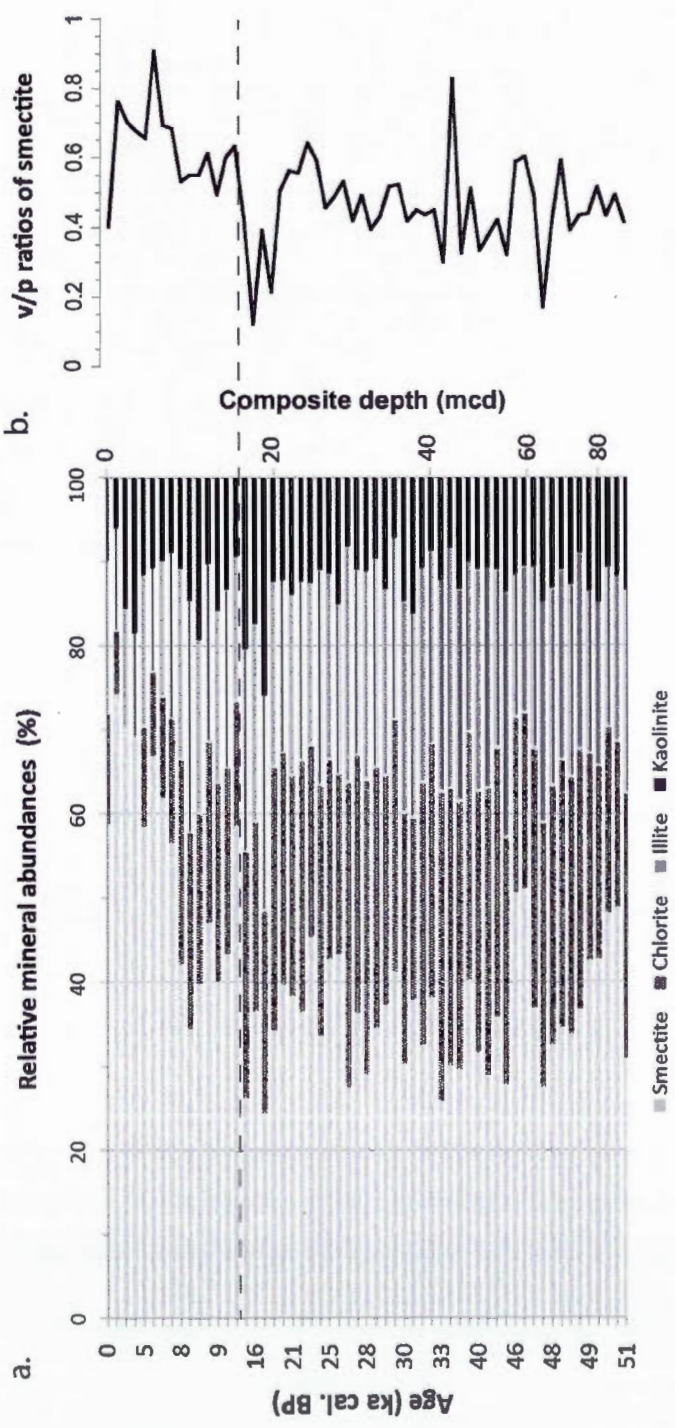


Figure 7 – Mineralogical data for the fraction $<2 \mu\text{m}$. (a) Histogram of semi-quantitative relative mineralogical abundances based on XRD data vs. composite depth and age. (b) Profile of v/p ratios of smectite plotted for comparison.

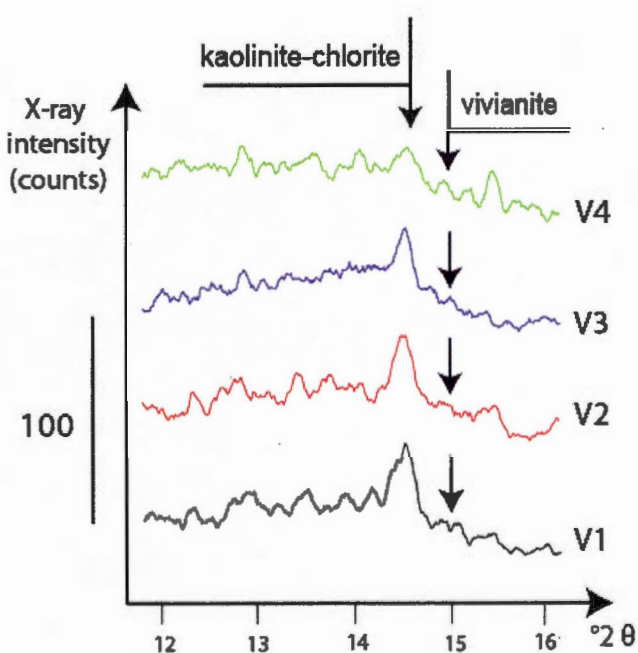


Figure 8 – XRD spectra obtained from the four vivianite samples V1 to V4. All four samples show a vivianite peak ($d = 6.73 \text{ \AA}$) accounting for 1 to 3% and a kaolinite-chlorite peak ($d = 7 \text{ \AA}$) accounting for 7% of the semi-quantitative relative mineralogical abundances.

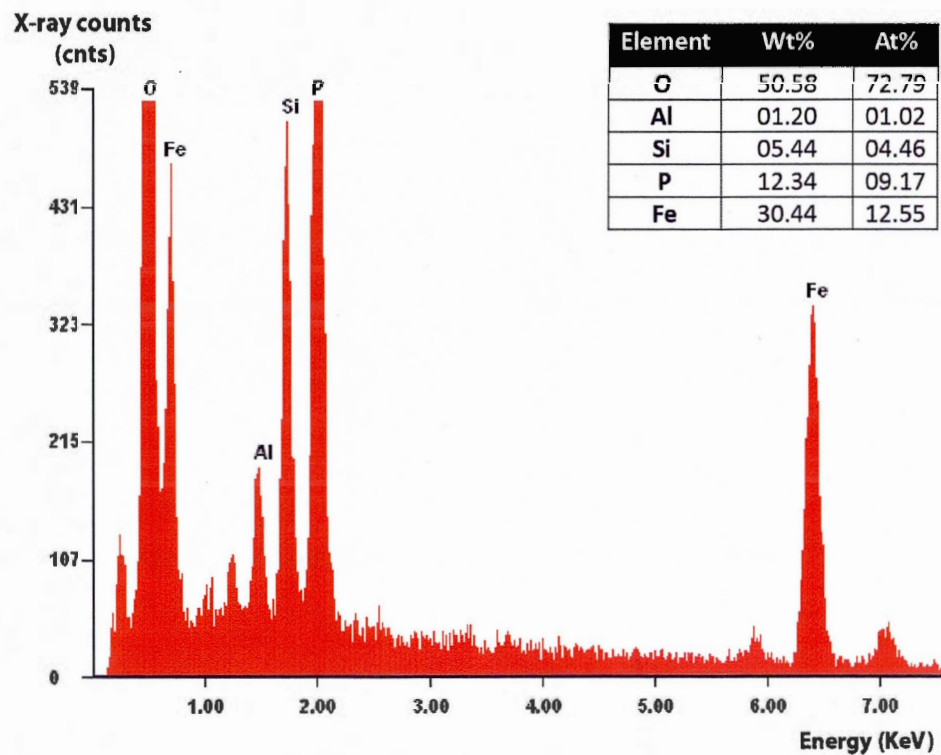


Figure 9 – One of the SEM-EDS spectra from a vivianite-rich region of concretion V5. Note that the high content in iron and phosphorus attests the presence of vivianite as well as the values for weight (wt%) and atomic percentages (at%) in the element abundance table.

Table 1 – Mean ($\pm 1\sigma$) of the semi-quantitative relative abundance (%) and measured d-spacing (Å) reflection intensity for bulk (<63 µm) and clay (<2 µm) fraction minerals over the entire sequence. Note that abundances $\leq 5\%$ correspond to trace minerals

Minerals	Measured intensity of reflection d (Å)	Average relative abundances (%)	$\pm 1\sigma$
<i>Mineralogical assemblages in the 0-63 µm fraction</i>			
Quartz (including cristobalite)	4.25	57 (58)	9 (9)
Feldspar	3.18	18	6
Smectite-Chlorite	1.4	7	5
Kaolinite-Chlorite	7	7	5
Calcite (including monohydrocalcite)	3.03	3 (4)	8 (9)
Mica	1.0	≤ 5	-
Pyroxene	2.99	≤ 5	-
Zeolite	8.99	≤ 5	-
Amphibole	8.42	≤ 5	-
Cristobalite	4.03	≤ 5	-
Monohydrocalcite	4.32	≤ 5	-
<i>Mineralogical assemblages in the 0-2 µm fraction</i>			
Smectite	17	41	12
Chlorite	7	25	8
Illite	10	22	4
Kaolinite	7	12	3

Table 2 – U-Th concentrations and activity ratios of vivianite samples ($\pm 2\sigma$ uncertainties of activity ratios have been calculated following a normal distribution).

ID	Type	Depth (m)	U (µg/g)	Th (µg/g)	$^{234}\text{U}/^{238}\text{U}$	$^{230}\text{Th}/^{234}\text{U}$	$^{230}\text{Th}/^{238}\text{U}$
V1		56.9	1.257	4.686	1.331	0.923	1.229
V2	Bulk sediment containing vivianite	66.2	1.145 ±0.003	5.083 ±0.051	1.139 ±0.008	1.142 ±0.016	1.301 ±0.015
V3		67.1	1.443 ±0.003	5.951 ±0.070	1.145 ±0.008	1.054 ±0.014	1.206 ±0.014
V4		78.6	1.216	5.100	1.069	1.126	1.204
V5	Cleaned concretion	56.9	0.286 ±0.001	1.056 ±0.007	1.568 ±0.011	0.779 ±0.009	1.221 ±0.012
V5'	Hand-picked vivianite grains	56.9	0.213 ±0.001	0.905 ±0.012	1.627 ±0.017	0.827 ±0.111	1.346 ±0.182

Table 3 – Estimates of authigenic vs. detrital U-fractions in the studied samples. Mean $^{238}\text{U}/^{232}\text{Th}$ ratios in samples V2, V3 and V4 have been used to estimate the detrital contribution to the total U in samples V1, V5 and V5', and the ingrowth $^{230}\text{Th}/^{234}\text{U}$ secular equilibrium conditions in the detrital fraction. All estimates are given with a $\pm 2\sigma$ uncertainty. The very strong excess in ^{234}U (vs. ^{238}U) of the authigenic fraction indicates that if some authigenic-U is still present in samples V2 to V4, as shown by their $^{234}\text{U}/^{238}\text{U}$ ratio (Table 2), it should not quantitatively weight very much in comparison with that inherited through detrital contamination.

ID	$^{238}\text{U}/^{232}\text{Th}$	$^{234}\text{U}/^{232}\text{Th}$	$^{230}\text{Th}/^{232}\text{Th}$	^{238}U total	^{238}U detr.	^{238}U auth.	^{234}U total	^{234}U detr.	^{234}U auth.	^{230}Th total	^{230}Th detr.	^{230}Th auth.	$^{230}\text{Th}/^{234}\text{U}$	$^{234}\text{U}/^{238}\text{U}$
V1	0.820 ± 0.010	1.091 ± 0.014	1.007 ± 0.015	0.938 ± 0.016	0.824 ± 0.016	0.115 ± 0.023	1.249 ± 0.022	0.920 ± 0.016	0.329 ± 0.027	1.153 ± 0.022	1.018 ± 0.019	0.135 ± 0.029	-	-
V2	0.688 ± 0.007	0.784 ± 0.010	0.784 ± 0.014	0.896 \dots	- \dots	- \dots	- \dots	- \dots	- \dots	- \dots	- \dots	- \dots	-	-
V3	0.741 ± 0.009	0.848 ± 0.011	0.848 ± 0.015	0.894 \dots	- \dots	- \dots	- \dots	- \dots	- \dots	- \dots	- \dots	- \dots	-	-
V4	0.729 ± 0.007	0.779 ± 0.009	0.779 ± 0.011	0.878 \dots	- \dots	- \dots	- \dots	- \dots	- \dots	- \dots	- \dots	- \dots	-	-
V2 to V4	0.719 ± 0.008	0.804 ± 0.010	0.889 ± 0.013	- \dots	- \dots	- \dots	-	-						
average														
V5	0.827 ± 0.006	1.297 ± 0.013	1.010 ± 0.012	0.213 ± 0.002	0.186 ± 0.002	0.028 ± 0.003	0.335 ± 0.004	0.207 ± 0.003	0.127 ± 0.005	0.260 ± 0.004	0.229 ± 0.004	0.031 ± 0.005	0.24 ± 0.04	4.58 ± 0.58
V5'	0.721 ± 0.010	1.173 ± 0.021	0.971 ± 0.131	0.159 ± 0.003	0.159 ± 0.003	0.003 ± 0.004	0.259 ± 0.006	0.178 ± 0.003	0.082 ± 0.007	0.215 ± 0.029	0.197 ± 0.004	0.018 ± 0.029	-	-

ANNEXE B

TABLEAUX DES DONNÉES

Tableau 1 – Données isotopiques des analyses de la séquence sédimentaire HU08-029-016PC, obtenues par comptage alpha (concentrations en U et en Th, et rapports d'activité).

Prof (cm)	^{238}U $\mu\text{g.g}^{-1}$	$\pm 1\sigma$	^{232}Th $\mu\text{g.g}^{-1}$	$\pm 1\sigma$	$^{234}\text{U}/^{238}\text{U}$	$\pm 1\sigma$	$^{230}\text{Th}/^{232}\text{Th}$	$\pm 1\sigma$	$^{230}\text{Th}/^{234}\text{U}$	$\pm 1\sigma$
0,5	1,555	0,025	13,897	0,261	0,943	0,022	1,667	0,040	5,201	0,115
8,5	1,712	0,034	11,883	0,217	0,984	0,027	1,353	0,033	3,142	0,079
16,5	1,503	0,030	12,946	0,156	0,933	0,027	0,745	0,014	2,264	0,057
24,5	1,283	0,017	9,193	0,132	0,993	0,019	0,760	0,017	1,805	0,038
32,5	1,305	0,023	9,150	0,140	0,985	0,024	0,775	0,018	1,814	0,045
40,5	1,125	0,022	7,405	0,103	0,940	0,027	0,861	0,018	1,984	0,050
48,5	1,022	0,020	4,325	0,067	1,055	0,029	0,963	0,021	1,272	0,032
56,5	1,459	0,032	6,351	0,101	1,007	0,031	0,874	0,020	1,245	0,035
64,5	1,762	0,038	6,910	0,098	1,050	0,031	0,810	0,017	0,997	0,026
72,5	1,842	0,041	8,491	0,124	1,005	0,031	0,634	0,015	0,958	0,027
80,5	1,499	0,033	10,094	0,150	1,004	0,031	0,611	0,015	1,348	0,039
88,5	1,191	0,025	8,038	0,150	0,984	0,030	0,851	0,023	1,922	0,057
96,5	1,021	0,020	7,647	0,119	1,037	0,028	0,743	0,018	1,767	0,047
104,5	1,273	0,025	7,277	0,119	0,985	0,027	0,803	0,020	1,534	0,041
112,5	1,317	0,026	12,461	0,239	0,989	0,027	0,836	0,024	2,631	0,076
120,5	1,261	0,026	11,980	0,177	0,923	0,028	0,798	0,018	2,704	0,074
128,5	1,527	0,029	13,163	0,194	0,897	0,025	0,594	0,014	1,880	0,052
136,5	1,155	0,020	12,111	0,133	0,920	0,023	0,800	0,013	3,002	0,066
144,5	1,049	0,019	15,145	0,154	0,951	0,024	0,657	0,011	3,284	0,073
153,5	0,987	0,019	13,531	0,138	0,989	0,026	0,614	0,010	2,804	0,064

Prof. (cm)	^{238}U $\mu\text{g g}^{-1}$	$\pm 1\sigma$	^{232}Th $\mu\text{g g}^{-1}$	$\pm 1\sigma$	$^{234}\text{U}/$ ^{238}U	$\pm 1\sigma$	$^{230}\text{Th}/$ ^{232}Th	$\pm 1\sigma$	$^{230}\text{Th}/$ ^{234}U	$\pm 1\sigma$
160,5	0,982	0,019	13,894	0,143	0,970	0,027	0,563	0,010	2,702	0,065
168,5	1,175	0,019	9,335	0,109	0,908	0,021	0,630	0,012	1,814	0,041
176,5	1,339	0,020	15,328	0,131	0,926	0,020	0,627	0,009	2,554	0,048
184,5	1,218	0,020	9,544	0,091	0,921	0,021	0,573	0,009	1,604	0,034
192,5	1,806	0,024	13,610	0,138	0,834	0,016	0,643	0,010	1,914	0,037
200,5	1,415	0,021	11,925	0,114	0,897	0,019	0,678	0,010	2,098	0,041
208,5	1,324	0,020	10,991	0,106	0,927	0,020	0,678	0,010	1,998	0,039
216,5	1,054	0,018	8,435	0,091	0,955	0,023	0,462	0,009	1,277	0,030
224,5	0,988	0,017	6,057	0,091	0,922	0,023	0,726	0,017	1,589	0,040
232,5	1,002	0,018	5,722	0,099	0,954	0,024	0,725	0,019	1,428	0,039
240,5	1,128	0,021	6,651	0,114	0,965	0,026	0,715	0,019	1,439	0,040
248,5	1,227	0,023	6,901	0,111	0,914	0,025	0,662	0,017	1,342	0,037
256,5	1,397	0,029	12,757	0,170	0,902	0,027	0,518	0,012	1,726	0,050
264,5	1,582	0,032	9,016	0,137	0,924	0,027	0,599	0,015	1,216	0,035
272,5	1,684	0,032	7,826	0,122	0,933	0,026	0,654	0,016	1,073	0,030
280,5	1,950	0,035	12,858	0,159	0,970	0,025	0,436	0,010	0,976	0,025
288,5	2,611	0,041	11,444	0,140	1,054	0,023	0,670	0,013	0,918	0,020
296,5	2,175	0,036	35,738	0,333	1,016	0,024	0,359	0,006	1,911	0,043
304,5	1,362	0,029	10,108	0,165	1,006	0,030	0,555	0,015	1,347	0,041
312,5	1,015	0,021	5,819	0,098	0,975	0,029	0,627	0,017	1,215	0,037
320,5	1,221	0,024	31,280	0,276	0,933	0,026	0,224	0,005	2,023	0,056
328,5	1,472	0,030	10,912	0,138	0,932	0,027	0,516	0,011	1,352	0,037
336,5	1,753	0,032	14,027	0,176	1,022	0,026	0,583	0,012	1,502	0,037
344,5	1,317	0,028	12,205	0,198	1,033	0,031	0,553	0,015	1,633	0,049
352,5	1,321	0,029	13,231	0,204	1,031	0,032	0,575	0,015	1,841	0,055
360,5	1,100	0,023	11,741	0,104	0,944	0,028	0,749	0,010	2,787	0,066
368,5	0,933	0,018	6,780	0,084	0,966	0,027	0,651	0,013	1,611	0,040
376,5	1,014	0,018	6,670	0,097	0,948	0,025	0,679	0,016	1,551	0,040

Prof. (cm)	^{238}U $\mu\text{g g}^{-1}$	$\pm 1\sigma$	^{232}Th $\mu\text{g g}^{-1}$	$\pm 1\sigma$	$^{234}\text{U}/$ ^{238}U	$\pm 1\sigma$	$^{230}\text{Th}/$ ^{232}Th	$\pm 1\sigma$	$^{230}\text{Th}/$ ^{234}U	$\pm 1\sigma$
384,5	1,048	0,022	8,236	0,134	0,937	0,028	0,612	0,016	1,691	0,051
392,5	0,985	0,016	11,094	0,150	0,955	0,022	0,431	0,011	1,674	0,045
400,5	1,012	0,021	7,471	0,124	0,940	0,029	0,571	0,016	1,478	0,046
408,5	1,071	0,022	7,071	0,113	0,904	0,027	0,624	0,016	1,502	0,044
416,5	1,138	0,023	6,584	0,119	0,982	0,028	0,593	0,017	1,150	0,036
424,5	1,171	0,022	8,703	0,112	0,966	0,026	0,554	0,012	1,402	0,036
440,5	1,669	0,032	50,949	0,479	1,113	0,029	0,327	0,006	2,953	0,072
456,5	1,052	0,021	12,976	0,158	0,948	0,027	0,539	0,011	2,311	0,060
472,5	1,250	0,027	10,221	0,129	0,876	0,027	0,505	0,011	1,552	0,045
488,5	1,107	0,024	10,670	0,147	0,995	0,030	0,460	0,011	1,466	0,043
504,5	1,485	0,028	7,871	0,141	1,033	0,028	0,657	0,019	1,110	0,032
520,5	1,584	0,031	19,003	0,180	0,991	0,027	0,302	0,006	1,204	0,031
536,5	1,055	0,021	8,728	0,143	0,957	0,027	0,521	0,015	1,483	0,045
552,5	1,201	0,023	9,187	0,132	0,955	0,026	0,541	0,013	1,427	0,039
568,5	1,247	0,024	7,819	0,126	0,999	0,028	0,605	0,016	1,251	0,036
584,5	1,111	0,023	8,828	0,121	0,956	0,029	0,547	0,013	1,498	0,043
600,5	0,984	0,016	8,467	0,113	0,904	0,022	0,446	0,011	1,398	0,037
616,5	1,307	0,026	14,248	0,211	0,931	0,027	0,495	0,013	1,910	0,057
632,5	1,273	0,020	11,172	0,153	0,911	0,021	0,462	0,011	1,465	0,039
648,5	1,501	0,032	7,801	0,120	1,049	0,031	0,625	0,016	1,020	0,029
664,5	1,127	0,019	10,378	0,130	0,910	0,022	0,455	0,010	1,515	0,039
680,5	1,360	0,022	9,131	0,106	1,034	0,024	0,490	0,010	1,048	0,024
704,5	1,473	0,027	16,356	0,137	0,837	0,023	0,220	0,004	0,961	0,026
720,5	1,405	0,027	12,085	0,131	0,974	0,026	0,366	0,008	1,063	0,028
736,5	1,395	0,027	9,303	0,097	1,077	0,029	0,399	0,008	0,815	0,020

Tableau 2 – Données isotopiques des analyses de la séquence sédimentaire HU08-029-004PC, obtenues par TIMS (pour les 40 premiers cm) et par comptage alpha (concentrations en U et en Th, et rapports d'activité).

Prof. (cm)	^{238}U $\mu\text{g.g}^{-1}$	$\pm 1\sigma$	^{232}Th $\mu\text{g.g}^{-1}$	$\pm 1\sigma$	$^{234}\text{U}/^{238}\text{U}$	$\pm 1\sigma$	$^{230}\text{Th}/$ ^{232}Th	$\pm 1\sigma$	$^{230}\text{Th}/$ ^{234}U	$\pm 1\sigma$
0,5	0,845	0,002	5,196	0,026	1,016	0,006	2,889	0,099	5,603	0,073
4,5	0,711	0,002	4,978	0,058	1,008	0,008	2,786	0,095	6,315	0,107
8,5	0,763	0,002	4,772	0,019	1,067	0,006	2,693	0,090	5,756	0,059
12,5	2,234	0,006	4,845	0,019	1,126	0,004	2,943	0,098	1,837	0,017
16,5	1,000	0,003	4,787	0,017	1,088	0,005	2,916	0,058	4,338	0,034
20,5	1,265	0,004	4,721	0,023	1,082	0,008	2,910	0,065	3,429	0,042
24,5	1,682	0,005	4,731	0,029	1,092	0,006	2,895	0,061	2,680	0,040
28,5	1,123	0,003	4,885	0,027	1,083	0,006	2,980	0,074	3,998	0,059
32,5	1,803	0,005	5,412	0,041	1,126	0,005	2,113	0,056	1,953	0,038
36,5	2,002	0,006	5,558	0,031	1,108	0,006	1,874	0,057	1,621	0,029
40,5	1,860	0,005	5,262	0,031	1,153	0,003	2,054	0,062	1,870	0,029
48,5	2,310	0,005	5,257	0,026	1,098	0,004	2,676	0,054	1,815	0,036
52,5	1,959	0,036	5,257	0,122	1,087	0,028	2,459	0,067	1,789	0,034
56,5	1,630	0,037	5,257	0,114	1,040	0,033	2,616	0,067	2,299	0,037
68,5	2,558	0,006	5,728	0,034	1,103	0,006	1,855	0,073	1,232	0,048
72,5	2,304	0,044	4,770	0,093	1,076	0,028	1,854	0,045	1,175	0,027
80,5	1,760	0,039	4,888	0,102	1,074	0,033	1,478	0,040	1,258	0,034
88,5	1,963	0,027	5,414	0,081	1,071	0,020	1,515	0,029	1,284	0,023
96,5	1,859	0,026	4,849	0,084	1,060	0,021	1,543	0,034	1,250	0,024
104,5	1,547	0,027	5,425	0,087	1,041	0,025	1,282	0,027	1,422	0,032
112,5	1,598	0,034	5,698	0,123	1,033	0,031	1,246	0,036	1,416	0,040
120,5	1,496	0,031	5,797	0,127	1,037	0,030	1,264	0,037	1,556	0,044
128,5	1,553	0,033	4,955	0,110	1,074	0,032	1,296	0,038	1,269	0,036

Prof. (cm)	^{238}U $\mu\text{g.g}^{-1}$	$\pm 1\sigma$	^{232}Th $\mu\text{g.g}^{-1}$	$\pm 1\sigma$	$^{234}\text{U}/^{238}\text{U}$	$\pm 1\sigma$	$^{230}\text{Th}/^{232}\text{Th}$	$\pm 1\sigma$	$^{230}\text{Th}/^{234}\text{U}$	$\pm 1\sigma$
136,5	1,546	0,031	5,202	0,098	1,040	0,029	1,272	0,032	1,355	0,035
148,5	1,375	0,030	5,640	0,110	1,001	0,031	1,374	0,035	1,854	0,051
160,5	1,714	0,034	5,727	0,102	1,026	0,028	1,533	0,035	1,644	0,040
172,5	1,775	0,035	5,851	0,085	1,049	0,029	1,461	0,028	1,511	0,034
184,5	1,604	0,033	6,577	0,095	1,001	0,029	1,360	0,026	1,834	0,044
196,5	1,533	0,026	5,644	0,083	1,054	0,025	1,487	0,028	1,710	0,035
208,5	1,735	0,029	5,439	0,081	1,051	0,024	1,606	0,030	1,578	0,031
220,5	1,389	0,025	6,331	0,090	1,065	0,027	1,360	0,026	1,917	0,041
232,5	1,148	0,017	6,140	0,086	0,988	0,021	1,216	0,023	2,167	0,043
244,5	2,060	0,037	6,917	0,129	1,068	0,026	1,148	0,029	1,188	0,029
256,5	1,445	0,027	5,491	0,092	1,055	0,027	1,239	0,028	1,469	0,035
268,5	1,461	0,027	5,569	0,093	1,050	0,028	1,166	0,026	1,393	0,033
280,5	1,361	0,027	6,000	0,106	0,966	0,027	1,104	0,027	1,658	0,043
292,5	1,281	0,028	6,032	0,110	1,013	0,031	1,126	0,028	1,724	0,047
304,5	1,217	0,026	5,851	0,098	0,926	0,028	1,203	0,027	2,058	0,055
316,5	1,226	0,023	5,801	0,097	0,927	0,025	1,102	0,025	1,852	0,047
328,5	1,559	0,032	5,544	0,095	0,965	0,028	1,212	0,028	1,470	0,038
340,5	1,254	0,024	6,040	0,101	0,966	0,027	1,126	0,026	1,851	0,047
352,5	1,121	0,023	6,072	0,122	0,978	0,029	1,110	0,031	2,026	0,057
364,5	1,112	0,023	5,959	0,120	0,979	0,029	1,104	0,031	1,990	0,057
376,5	1,066	0,019	6,707	0,118	1,011	0,026	1,075	0,026	2,203	0,055
388,5	1,111	0,021	7,060	0,128	1,001	0,027	1,002	0,026	2,096	0,055
400,5	1,227	0,021	6,145	0,121	0,975	0,023	1,076	0,030	1,820	0,047
412,5	1,300	0,021	6,082	0,112	1,009	0,023	1,094	0,028	1,670	0,040
424,5	1,447	0,024	6,639	0,123	0,996	0,023	1,076	0,028	1,633	0,040
432,5	1,338	0,023	6,196	0,113	1,023	0,024	1,093	0,028	1,630	0,039
444,5	1,585	0,034	5,581	0,118	0,975	0,029	1,104	0,032	1,312	0,038

Prof. (cm)	^{238}U $\mu\text{g.g}^{-1}$	$\pm 1\sigma$	^{232}Th $\mu\text{g.g}^{-1}$	$\pm 1\sigma$	$^{234}\text{U}/^{238}\text{U}$	$\pm 1\sigma$	$^{230}\text{Th}/^{232}\text{Th}$	$\pm 1\sigma$	$^{230}\text{Th}/^{234}\text{U}$	$\pm 1\sigma$
456,5	1,195	0,021	6,284	0,109	0,972	0,025	1,041	0,025	1,854	0,046
464,5	1,138	0,022	5,780	0,105	0,978	0,027	1,176	0,029	2,010	0,051
476,5	1,204	0,022	6,300	0,138	0,997	0,026	1,228	0,036	2,122	0,058
488,5	1,429	0,029	5,970	0,125	0,947	0,027	1,629	0,043	2,367	0,062
500,5	1,070	0,021	6,238	0,122	0,955	0,027	0,914	0,026	1,838	0,053
512,5	1,029	0,022	5,388	0,100	0,885	0,027	0,826	0,023	1,608	0,049
524,5	0,998	0,022	4,110	0,058	0,978	0,030	0,729	0,016	1,011	0,028
536,5	1,195	0,024	6,260	0,114	0,927	0,027	0,661	0,019	1,229	0,038
548,5	1,054	0,021	4,952	0,062	0,952	0,027	0,713	0,014	1,160	0,029
560,5	1,213	0,023	6,062	0,109	0,922	0,025	0,706	0,020	1,260	0,037
572,5	1,156	0,024	6,451	0,107	0,889	0,027	0,731	0,019	1,510	0,044
576,5	1,136	0,022	5,229	0,101	0,972	0,027	0,787	0,023	1,229	0,036
580,5	1,210	0,023	5,289	0,103	0,953	0,026	0,779	0,023	1,177	0,035
584,5	1,295	0,026	4,984	0,100	0,943	0,027	0,930	0,027	1,249	0,036
592,5	1,034	0,016	6,962	0,091	0,968	0,021	1,618	0,027	3,707	0,068
604,5	1,023	0,016	7,058	0,093	0,928	0,021	1,189	0,021	2,912	0,059
616,5	1,000	0,016	7,365	0,094	0,914	0,021	1,052	0,019	2,792	0,057
628,5	1,048	0,018	7,485	0,095	0,941	0,023	1,007	0,018	2,518	0,055
640,5	0,985	0,019	8,083	0,166	0,922	0,025	1,003	0,029	2,939	0,083
652,5	1,064	0,020	9,136	0,182	0,930	0,025	0,983	0,028	2,989	0,083
664,5	1,044	0,019	6,566	0,114	0,957	0,024	1,028	0,025	2,223	0,055
676,5	1,539	0,023	7,207	0,117	1,009	0,021	0,835	0,020	1,276	0,030
688,5	1,495	0,027	8,036	0,150	1,028	0,026	0,591	0,018	1,018	0,031
696,5	1,691	0,033	5,235	0,119	0,994	0,027	1,058	0,034	1,086	0,032
700,5	1,160	0,024	6,341	0,142	0,958	0,029	1,192	0,036	2,241	0,066
712,5	0,822	0,017	4,149	0,086	0,946	0,028	0,774	0,024	1,360	0,043
724,5	0,849	0,017	4,561	0,079	0,979	0,027	0,726	0,019	1,312	0,037

Prof. (cm)	^{238}U $\mu\text{g.g}^{-1}$	$\pm 1\sigma$	^{232}Th $\mu\text{g.g}^{-1}$	$\pm 1\sigma$	$^{234}\text{U}/^{238}\text{U}$	$\pm 1\sigma$	$^{230}\text{Th}/^{232}\text{Th}$	$\pm 1\sigma$	$^{230}\text{Th}/^{234}\text{U}$	$\pm 1\sigma$
736,5	0,731	0,016	2,863	0,055	0,969	0,031	0,862	0,024	1,147	0,035
748,5	1,134	0,021	4,826	0,087	0,968	0,025	0,793	0,022	1,148	0,032
760,5	1,126	0,024	4,302	0,088	1,002	0,031	0,863	0,026	1,084	0,033
772,5	1,063	0,023	8,282	0,136	0,969	0,030	1,218	0,027	3,226	0,086
784,5	0,869	0,019	5,664	0,100	0,982	0,030	0,979	0,025	2,141	0,061
796,5	1,106	0,023	6,043	0,111	0,966	0,029	0,905	0,024	1,686	0,048
808,5	1,742	0,039	6,361	0,112	0,981	0,031	1,151	0,028	1,410	0,039
820,5	0,974	0,020	6,932	0,119	1,011	0,030	0,844	0,021	1,954	0,054
832,5	1,483	0,025	6,677	0,113	1,069	0,025	0,850	0,021	1,179	0,029
844,5	1,123	0,021	7,469	0,117	1,046	0,028	0,702	0,017	1,470	0,039
856,5	1,015	0,023	7,526	0,118	1,017	0,032	0,595	0,015	1,428	0,043
868,5	0,724	0,015	3,318	0,065	0,950	0,028	0,757	0,022	1,203	0,037
884,5	0,811	0,019	4,365	0,077	0,943	0,032	0,527	0,016	0,991	0,034

Tableau 3 – Données isotopiques des analyses de la séquence sédimentaire HU08-029-004PC, obtenues au MC-ICP-MS.

Prof. (cm)	^{230}Th (dpm/g)	$\pm 1\sigma$	^{231}Pa (dpm/g)	$\pm 1\sigma$
0,5	3,3339	0,0196	0,1728	0,0019
8,5	3,2185	0,0166	0,1790	0,0021
16,5	3,5959	0,0215	0,3655	0,0035
20,5	3,2599	0,0159	0,1843	0,0015
28,5	3,6241	0,0201	0,2487	0,0050
32,5	2,7111	0,0183	0,1485	0,0010
48,5	2,8294	0,0178	0,1268	0,0011
72,5	2,1955	0,0253	0,2071	0,0034
88,5	2,1818	0,0175	0,0984	0,0010
104,5	1,8317	0,0205	0,2266	0,0022
120,5	1,9650	0,0116	0,0538	0,0006
160,5	2,3442	0,1015	0,0693	0,0010
164,5	2,1358	0,0235	0,1151	0,0031
196,5	2,3319	0,0133	0,1782	0,0010
220,5	2,2693	0,0156	0,1822	0,0007
244,5	2,1080	0,0111	0,1391	0,0004
268,5	1,7042	0,0264	0,1102	0,0005
280,5	1,8478	0,0139	0,1293	0,0007
316,5	1,6836	0,0177	0,0712	0,0005
340,5	1,8742	0,0139	0,1274	0,0007
376,5	1,7048	0,0211	0,0915	0,0006
400,5	1,8358	0,0149	0,1145	0,0004
424,5	1,6726	0,0198	0,0694	0,0009
456,5	1,6588	0,0124	0,0770	0,0008
476,5	1,9328	0,0109	0,0439	0,0005
500,5	1,4830	0,0138	0,0777	0,0002

Prof. (cm)	^{230}Th (dpm/g)	$\pm 1\sigma$	^{231}Pa (dpm/g)	$\pm 1\sigma$
512,5	1,1868	0,0078	0,0547	0,0003
524,5	0,8438	0,0078	0,0285	0,0002
548,5	0,9738	0,0058	0,0427	0,0002
576,5	1,0722	0,0057	0,0482	0,0001
592,5	2,9515	0,0176	0,1787	0,0005
604,5	2,2391	0,0225	0,0338	0,0001
640,5	2,0425	0,0139	0,0935	0,0007
676,5	1,5987	0,0085	0,0802	0,0004
696,5	1,6248	0,0099	0,0894	0,0007
712,5	0,9783	0,0067	0,0384	0,0004
724,5	0,9143	0,0082	0,0331	0,0002
760,5	1,0449	0,0057	0,0451	0,0001
784,5	1,5776	0,0097	0,0555	0,0003
808,5	1,9184	0,0160	0,1036	0,0003
820,5	1,3964	0,0150	0,0447	0,0005
840,5	1,3901	0,0072	0,0733	0,0004
856,5	1,1416	0,0139	0,0444	0,0003
868,5	0,7506	0,0053	0,1297	0,0003
884,5	0,6671	0,0058	0,0134	0,0002

Tableau 4 – Données de minéralogie de la séquence sédimentaire HU08-029-004PC, obtenues par la technique de diffraction aux rayons X (abondances relatives en %).

Prof. (cm)	Quartz	Feldsp.	Calcite	Dolom.	Mica	Amph.	Kao./ Chlor.	Pyrox.	Sm.
0,5	31,4	22,5	32,4	0	7	3,5	3,2	0	0
4,5	29,8	17,9	39,2	0	5,6	4,3	3,3	0	0
8,5	24,9	18,9	35,7	3,1	8,1	4,4	3,1	0	1,7
12,5	31,4	15,4	39,4	2,5	5,9	2,7	2,6	0	0
16,5	27,2	17	38	2,8	7,2	4,9	2,8	0	0
20,5	27,3	21	37,6	3,6	4,6	2,9	2,9	0	0
24,5	21,3	25,7	30,9	3	6,3	7,5	3,4	0	1,8
28,5	25,5	26,5	34,7	1,8	5,8	3,2	2,4	0	0
32,5	33,3	27,8	20,8	2,5	7,1	5,5	2,9	0	0
36,5	36,7	21,8	25,8	3,8	5,4	3,8	2,7	0	0
40,5	25,1	26,2	29	4,5	6,1	4,4	3	0	1,6
44,5	25,9	26	28,7	4,5	6	4,4	3	0	1,6
48,5	29,7	18,1	34,8	4,6	5,6	4,5	2,7	0	0
52,5	20,32	27,7	23,69	2,81	18,14	4,6	2,74	0	0
56,5	19,71	34,94	18,71	1,7	14,68	5,28	2,64	2,34	0
60,5	14,94	28,56	25,96	1,85	16,63	4,45	3,2	4,39	0
64,5	28,98	24,87	21,51	2,03	14,45	4,82	3,33	0	0
68,5	40,7	21,6	20,6	4,1	5,3	3,9	3,8	0	0
72,5	26,3	26	26,7	3,7	6,4	5,8	3,6	0	1,6
76,5	29,7	26,9	26,8	3,2	5,6	5,4	2,4	0	0
80,5	43,8	22	15,4	4,7	6,5	4,6	3,1	0	0
84,5	36,6	22,5	18,6	3,9	7,2	6,3	3,7	0	1,4
88,5	34,8	26,9	18,3	3,8	8,5	4,7	2,9	0	0
92,5	26	25	19,4	5	10,8	10,2	3,6	0	0
96,5	35,5	25,3	19,7	4,4	7,8	4,1	3	0	0

Prof. (cm)	Quartz	Feldsp.	Calcite	Dolom.	Mica	Amph.	Kao./ Chlor.	Pyrox.	Sm.
100,5	34	31,6	10,9	5,6	9,9	5	2,9	0	0
104,5	43,1	30,4	6,9	3,3	6,7	4,9	3	0	1,7
108,5	37,9	30,2	11,3	5,7	5,7	6,5	2,8	0	0
112,5	38,9	32,1	9,4	6,5	5,9	4,7	2,5	0	0
116,5	34,4	33,2	10	4,7	8,4	6,1	3,2	0	0
120,5	40,7	27,9	6,7	5,6	7,8	6,1	2,8	0	2,4
124,5	41,1	29	9	4,4	7,8	5,3	3,3	0	0
128,5	42,6	31,5	10,3	4,5	2,7	5,2	3,2	0	0
132,5	38,7	30,1	5,8	3,7	11,4	7,9	2,5	0	0
136,5	42,5	32,7	8,9	4,5	3,9	5,5	2,2	0	0
140,5	44,2	26,3	6,3	5,3	7,3	5,7	2,7	0	2,2
144,5	43,8	36	4,1	5,5	5	3,1	2,5	0	0
148,5	32,6	40,1	5,2	3,5	7,4	5,8	3,1	0	2,4
152,5	27,8	49,8	3,1	5,3	7,5	3,1	3,5	0	0
156,5	46,7	26,8	6,9	5	4,8	5,4	4,4	0	0
160,5	44,9	30,3	5,6	6,1	4,8	5	3,4	0	0
164,5	39,3	31,7	7,1	4,8	5,2	7,2	4,9	0	0
168,5	42	29,2	5,8	6,7	6,4	4,8	5,2	0	0
172,5	39,8	28	5,3	10,8	6	4,9	5,2	0	0
176,5	43,4	22,6	7,5	15,3	3,5	5	2,7	0	0
180,5	51,4	22,6	7,8	5,7	5,9	2,9	3,7	0	0
184,5	37,1	25,2	8	8,1	7,8	6,2	4,8	0	2,6
188,5	51,1	24,9	5,9	8	3,4	3	3,6	0	0
192,5	42,1	37	0	9,8	4,9	2,4	3,9	0	0
196,5	35,4	34,6	9	7,5	6,4	3,1	3,9	0	0
200,5	34,9	34,7	5,9	6	6,4	5,5	3,9	0	2,8
204,5	42,5	25,8	7,7	7	4,7	7,4	4,8	0	0
208,5	39	32,9	8,9	3,6	4	7,3	4,3	0	0

Prof. (cm)	Quartz	Feldsp.	Calcite	Dolom.	Mica	Amph.	Kao./ Chlor.	Pyrox.	Sm.
212,5	56,7	21,6	3,9	4,6	3,3	7,8	2,2	0	0
216,5	39	28,9	10,2	8,9	5,9	3,2	4,1	0	0
220,5	50,2	24,9	6	5,4	7,9	3,3	2,3	0	0
224,5	47	32,9	2,4	4,4	4,8	4,1	4,4	0	0
228,5	47,2	29,4	1,9	6,9	6,4	4,4	3,8	0	0
232,5	52,8	30,3	0	6,6	4,1	3,5	2,7	0	0
236,5	45,4	29	3,1	6,1	6,9	5,6	4	0	0
240,5	44,1	29,9	5,6	6,7	5,3	3,9	4,3	0	0
244,5	42,7	26,7	9,1	7,7	4,2	4,7	4,8	0	0
248,5	50,5	22,4	5,9	6,7	5	5	4,5	0	0
252,5	53,2	26,4	3,4	4,5	4	5,1	3,4	0	0
256,5	47,6	28	3,2	6,6	4,5	5,9	4,2	0	0
260,5	39,5	35,9	5,9	7,2	3,2	3,1	5,1	0	0
264,5	42,6	30,8	5	8,2	3,8	5	4,6	0	0
268,5	46,9	29,9	4,7	6,9	3,8	4	3,8	0	0
272,5	40,9	29,1	5,6	5,4	6,5	6,7	5,7	0	0
276,5	41,4	30	6,6	7,3	3,1	8,2	3,5	0	0
280,5	40,7	33,1	5,6	6,5	5,4	4,3	4,4	0	0
284,5	43,7	26,8	4	8,9	5,3	4,6	4,5	0	2,2
288,5	49,8	22,8	6,3	8,6	3,5	3,6	3,3	0	2
292,5	44,6	25,8	7,5	7,4	4,6	5,3	4,7	0	0
296,5	44,9	25,7	5,8	7	3,9	8,4	4,3	0	0
300,5	31,6	29,5	7,4	7,5	7,5	7,2	5,9	0	3,5
304,5	45,1	30	5,5	6,5	3,4	3,3	3,8	0	2,4
308,5	39,9	25,7	7,1	6	8,3	3,9	6,5	0	2,4
312,5	41,6	26,6	7,4	12,9	3,9	3,8	3,8	0	0
316,5	56,6	22,1	3,9	9,4	2	3,1	2,9	0	0
320,5	40,7	28,7	7,6	9	4,6	4,2	5,3	0	0

Prof. (cm)	Quartz	Feldsp.	Calcite	Dolom.	Mica	Amph.	Kao./ Chlor.	Pyrox.	Sm.
324,5	46,4	24	5,8	7,2	5,9	5,4	5,3	0	0
328,5	24,5	36,3	11,8	8,8	7,2	5	6,3	0	0
332,5	39,4	30,8	8,1	9,5	3,9	3,9	4,4	0	0
336,5	46	24,5	7,1	7,9	3,8	5,2	5,3	0	0
340,5	28,6	42,2	5,3	11,3	3,9	5,2	3,5	0	0
344,5	22,1	38,8	7,8	12,5	5,5	8	5,3	0	0
348,5	47,6	27,3	6,2	9,5	2,6	3,4	3,4	0	0
352,5	41,1	27,5	8,4	11,5	4,3	3,2	4	0	0
356,5	39,5	27,3	8,4	11,4	3,8	5,5	3,9	0	0
360,5	45,7	26	10,1	8,8	3,2	2,8	3,6	0	0
364,5	37,7	25,4	9,5	14,5	4,2	4,6	4,2	0	0
368,5	39,4	21,9	8,8	19,9	3,6	2,5	3,9	0	0
372,5	18,6	30,8	16,4	19,5	4,3	4,5	5,8	0	0
376,5	36,4	26,5	11,5	12,6	4,5	3,3	5,2	0	0
380,5	34,8	21,5	10,7	13,2	8,6	5,9	5,3	0	0
384,5	36,5	22,1	13,7	14,8	3,9	4,5	4,5	0	0
388,5	29,3	20	15,9	24,6	3,3	3	3,9	0	0
392,5	53,4	18,5	8,6	9,6	2,7	4,2	3	0	0
396,5	32,5	22,7	8,4	23,9	3,7	4,2	4,7	0	0
400,5	48,8	18,5	10,8	11,5	3,5	3,3	3,6	0	0
404,5	43,6	21,9	8,4	8	9,7	3,7	4,7	0	0
408,5	36,6	29,5	10,3	6,4	7,3	4,5	5,3	0	0
412,5	39,5	31,7	7,7	7,7	4	4,1	5,5	0	0
416,5	46,2	26,2	8,4	5,4	3,4	6,1	4,3	0	0
420,5	46,3	28,4	8,3	5	4,4	3,2	4,5	0	0
424,5	41,8	24,9	9,4	5,4	7,4	3,9	4,6	0	2,6
428,5	38,7	34,6	10,2	5,8	3,5	2,7	4,4	0	0
432,5	48,5	24,4	8,2	3,6	7,3	4,3	3,7	0	0

Prof. (cm)	Quartz	Feldsp.	Calcite	Dolom.	Mica	Amph.	Kao./ Chlor.	Pyrox.	Sm.
436,5	40,2	27	9,4	4,8	5,9	7,4	5,4	0	0
440,5	49,1	28,3	3,8	3,8	5,4	5	4,5	0	0
444,5	41,8	27	13	3,6	5,1	4,9	4,6	0	0
448,5	55,8	20,5	10,7	4,3	2,8	2,7	3,3	0	0
452,5	57,4	22,1	10,2	3	2,5	1,7	3,1	0	0
456,5	49,1	22	11,7	6,4	3,4	3,4	4	0	0
460,5	40	27,9	14,2	7,2	4,5	3,4	2,8	0	0
464,5	46,7	23,4	9,2	8,5	3,9	5	3,2	0	0
468,5	43,6	35	7,8	5,7	2,7	2,1	3,1	0	0
472,5	46,8	31,8	7,1	3,1	4,3	3,1	3,8	0	0
476,5	41,4	27,5	12,6	7	5,1	3,2	3,2	0	0
480,5	39,7	21,7	19,9	4,4	5	4,4	4,9	0	0
484,5	38,8	20,4	23,4	4,7	4,5	3,4	4,8	0	0
488,5	29,6	14,3	33,4	11	4,4	3,6	3,7	0	0
492,5	29,3	10,6	35,8	16	2,4	3,4	2,5	0	0
496,5	35	17,7	24,8	12,6	2,2	5,5	2,1	0	0
500,5	27,8	8,6	44,7	14,1	1,7	1	2,1	0	0
504,5	48,2	15,7	19,3	13,7	1,2	1	0,9	0	0
508,5	28,5	8,9	44	15,6	1,3	0	1,7	0	0
512,5	47,5	6,5	31	11,1	1,2	1	1,7	0	0
516,5	24,6	20,8	35,8	14,7	1,7	1	1,4	0	0
520,5	43	13	24,9	15,3	1,7	1	1,2	0	0
524,5	37,7	12,8	26,4	18,3	2,2	1,2	1,5	0	0
528,5	42,7	14,6	23,4	15,7	1,1	1,4	1	0	0
532,5	28,9	16,5	36,1	11,5	3,2	2,2	1,5	0	0
536,5	33,1	7,5	42,2	12,7	1,3	1,4	1,8	0	0
540,5	32	9,2	36	18	1,9	1,2	1,7	0	0
544,5	26,4	9,3	43,1	15,9	1,9	1,5	2	0	0

Prof. (cm)	Quartz	Feldsp.	Calcite	Dolom.	Mica	Amph.	Kao./ Chlor.	Pyrox.	Sm.
548,5	12,1	11,9	46,4	24,6	2,8	0	2,3	0	0
552,5	22,4	7,9	50,1	13,2	2,2	1,5	2,7	0	0
556,5	22,4	7,3	52,3	13,4	1,8	1,1	1,9	0	0
560,5	19,4	10,9	51,8	14,2	1,8	0	1,9	0	0
564,5	19,3	5,4	56,4	12,4	1,9	1,8	2,7	0	0
568,5	17,9	7,5	55,4	13,1	2	1,8	2,1	0	0
572,5	18,9	6,4	53,6	14,7	1,8	1,1	2,3	0	1
576,5	37,3	7,7	37,4	13,6	1,5	1	1,6	0	0
580,5	21,6	15,4	43,9	17	1	0	1,2	0	0
584,5	14,2	7	54,1	18,4	2,2	1,6	2,5	0	0
588,5	21,5	6	55,9	13,6	1,5	0	1,4	0	0
592,5	30,4	25,9	13,9	4,3	3,9	8,4	4,6	6,3	2,4
596,5	33,2	29,7	16,7	4,3	2,7	4,7	3,4	5,5	0
600,5	42,1	25,3	8	6,2	3,2	3,5	4,6	7,1	0
604,5	37,9	23,9	15,2	6,4	4,2	3,6	4,1	4,7	0
608,5	30,9	29,5	7,3	7,1	4,6	5,6	4,8	10,3	0
612,5	38,1	31	4,8	4,1	4,7	5,2	4,9	7,2	0
616,5	34,9	31,9	5,6	4	3,8	5,1	4,9	6,9	2,9
620,5	31,8	36,8	9,6	0	4	4,7	5,3	7,8	0
624,5	40	27,8	6,6	3,5	5,1	4,2	4,1	5,4	3,3
628,5	36,2	31,4	8,7	2,5	4,4	5,5	4,2	7,1	0
632,5	36,2	29,4	10,1	3,8	4,1	5,2	4,9	6,3	0
636,5	35,7	28,2	10,8	4,8	5	4,1	5,6	5,9	0
640,5	34,6	35,7	9,5	3,6	3,6	3,9	3,7	5,4	0
644,5	29,8	28,9	14	5,1	5,3	4,3	4,7	7,9	0
648,5	35,1	28,2	8,8	5,3	5,1	4,6	7	6	0
652,5	38,1	30,4	10,9	3,7	3,5	3,6	4,1	5,8	0
656,5	39,4	30,2	10,4	0	4,6	4,5	4,8	6,1	0

Prof. (cm)	Quartz	Feldsp.	Calcite	Dolom.	Mica	Amph.	Kao./ Chlor.	Pyrox.	Sm.
660,5	35,2	35,2	8,9	0	5,5	4,2	5,2	5,8	0
664,5	33,1	30	4,4	5,1	5,3	3,9	5,5	9,6	3,1
668,5	38,9	27,7	7,1	4,2	4,4	5,7	4,8	7,2	0
672,5	46,5	27,6	3,4	3,8	4,4	3,5	4,8	5,9	0
676,5	40,9	30,5	4,8	0	4,4	6	5,8	7,7	0
680,5	41,3	28,9	4,2	0	4,9	6,8	5,7	8,2	0
684,5	36,6	29,7	3,8	4,4	5,6	8,2	5	6,6	0
688,5	31,7	34	5	4,1	4,7	7,3	6,4	6,8	0
692,5	38,7	28,3	5,6	5,1	4	4,9	4,7	8,6	0
696,5	35,5	31,3	5,6	3,8	5,2	5,3	5,4	7,9	0
700,5	31,1	22,1	25,9	7,6	3,2	3,1	3,1	4	0
704,5	29,7	10,4	38,1	14,6	2,5	2,1	2,5	0	0
708,5	34,3	9,6	36,6	16,6	1,5	0	1,3	0	0
712,5	32,2	10,4	28,9	22,2	1,9	2,6	1,9	0	0
716,5	30	20,9	16,8	24,9	4,9	2,5	0	0	0
720,5	35,6	11	27,6	19,5	2,4	2,5	1,3	0	0
724,5	35,3	11,2	36,9	11,3	1,8	2	1,5	0	0
728,5	18,1	7,2	49,3	18,2	3,5	1,5	2,2	0	0
732,5	28,4	15,6	34,8	15,4	2,6	1,2	2	0	0
736,5	26,5	13,3	23,2	19,7	3,1	12,6	1,7	0	0
740,5	20,2	7,6	48,4	16,4	2,7	2,6	2,1	0	0
744,5	22	6,9	37	26,3	2,8	0,8	1,3	2,9	0
748,5	17,1	8,5	46	19,6	2,8	3,4	2,5	0	0
752,5	22,2	12,9	41,2	19,1	1,8	1,4	1,3	0	0
756,5	21,8	5,7	50	16,2	2,5	1,8	1,9	0	0
760,5	22,1	6,2	51,3	16,1	1,9	0,9	1,4	0	0
764,5	38,1	28,2	11,2	3,8	4,4	4,5	4,3	5,8	0
768,5	33,4	24	12,3	2,9	4,1	13,2	4,7	5,4	0

Prof. (cm)	Quartz	Feldsp.	Calcite	Dolom.	Mica	Amph.	Kao./ Chlor.	Pyrox.	Sm.
772,5	33,4	31,3	12,9	3,8	4,2	5,3	3,5	5,5	0
776,5	28,5	30,6	13,5	5	5,5	3,7	4	6,7	2,4
780,5	71,1	12,2	5,5	1,7	2,1	1,9	1,9	2,6	1,1
784,5	36,1	30,1	6,5	5,1	4,4	4,9	4,4	8,5	0
788,5	39,4	31,7	3,5	4,1	5	4,9	3,9	7,5	0
792,5	44,4	28,3	3,3	4,3	3,8	4,3	3,1	6,3	2,3
796,5	37,7	31,4	5,6	3,8	3,2	5,4	4,8	8,1	0
800,5	37	28,7	5,5	5	4,3	9,9	3,3	6,4	0
804,5	34,6	30,3	5,7	4,1	5,4	5,9	4,9	9	0
808,5	38,7	27,4	4,8	4,3	4,8	5	5	8	2
812,5	35,5	29,6	6,1	4,2	9,6	3,6	4,1	7,3	0
816,5	31,1	33,1	8,7	5,6	4,9	4,9	3,8	7,8	0
820,5	33,9	31,6	4,9	5,5	3,6	5,9	6	8,7	0
824,5	39,2	30,4	3,8	4,6	3,3	7,7	4,2	6,7	0
828,5	36	37,6	3,4	4	3,3	3,8	3,8	5,8	2,2
832,5	33,4	32,5	5,4	4,5	4,6	7,3	4,4	7,7	0
836,5	32,8	34,3	5,9	3,7	4,4	7,3	4,2	7,4	0
840,5	37	28,1	5,7	4,7	4,4	6	5,2	8,9	0
844,5	35,6	29,5	5	4	5,7	7,7	6,7	5,8	0
848,5	32,6	31	5,4	3,9	7,2	8,3	5,1	6,5	0
852,5	38,2	29	2,8	4,5	4,5	10	5,2	5,8	0
856,5	36,5	31,7	4,3	4,6	4,4	6,7	4,9	6,9	0
860,5	41	26	5,9	3,7	4	5,2	6,1	8,2	0
864,5	35,5	27,7	16,1	5,4	3,4	3,1	3,5	5,3	0
868,5	55,9	15,6	9,4	13,2	2,3	2	1,5	0	0
872,5	41	36,5	4,4	10,5	1,8	5	0,8	0	0
876,5	35,3	43,4	3,8	13,5	1,2	2,7	0	0	0
880,5	59,2	32	2,8	1,8	0,8	2,5	0,8	0	0

Prof. (cm)	Quartz	Feldsp.	Calcite	Dolom.	Mica	Amph.	Kao./ Chlor.	Pyrox.	Sm.
884,5	50,4	42,4	1,9	3,9	0,6	0,7	0	0	0
888,5	31,1	55,4	2,6	6,4	1,2	2,8	0,5	0	0
892,5	45	23,2	18,5	7,8	1,9	2	1,6	0	0

Tableau 5 – Données de carbone (carbone total -C-, carbone organique -C_{org}-, carbone inorganique -C_{inorg}-) de la séquence sédimentaire HU08-029-004PC (en % du poids sec du sédiment total).

Prof. (cm)	%C	%C _{org}	%C _{inorg}
0,5	2,47	0,38	2,09
4,5	2,45	0,37	2,08
8,5	2,54	0,35	2,18
16,5	2,69	0,32	2,25
20,5	2,56	0,29	2,26
24,5	2,55	0,23	1,87
28,5	2,10	0,20	1,84
36,5	2,04	0,23	1,50
40,5	1,76	0,22	1,79
44,5	1,73	0,29	1,89
48,5	2,01	0,20	1,86
52,5	2,18	0,30	1,97
56,5	2,06	0,27	2,00
60,5	2,26	0,38	2,08
64,5	2,27	0,30	1,88
68,5	2,46	0,20	1,38
72,5	2,18	0,30	1,54
76,5	1,58	0,34	1,60
80,5	1,84	0,22	0,94
84,5	1,94	0,28	1,14
88,5	1,16	0,30	1,09
92,5	1,42	0,30	1,39
96,5	1,40	0,34	1,33
100,5	1,69	0,28	0,86
104,5	1,66	0,22	0,51

Prof. (cm)	%C	%C _{org}	%C _{inorg}
108,5	1,14	0,26	0,65
112,5	0,73	0,26	0,62
116,5	0,91	0,24	0,59
120,5	0,89	0,18	0,48
124,5	0,83	0,22	0,52
128,5	0,66	0,29	0,57
132,5	0,75	0,27	0,51
136,5	0,86	0,21	0,43
140,5	0,78	0,22	0,47
144,5	0,64	0,21	0,37
148,5	0,69	0,23	0,35
152,5	0,58	0,27	0,32
156,5	0,59	0,28	0,39
160,5	0,59	0,32	0,33
164,5	0,67	0,30	0,53
168,5	0,65	0,29	0,47
172,5	0,83	0,31	0,67
176,5	0,76	0,34	1,11
180,5	0,98	0,31	0,81
188,5	1,12	0,34	0,62
192,5	0,96	0,31	0,47
196,5	0,97	0,36	0,53
200,5	0,78	0,30	0,53
204,5	0,89	0,34	0,59
208,5	0,83	0,33	0,56
212,5	0,94	0,30	0,51
216,5	0,90	0,24	0,64
220,5	0,81	0,21	0,65

Prof. (cm)	%C	%C _{org}	%C _{inorg}
224,5	0,88	0,14	0,41
228,5	0,87	0,18	0,35
232,5	0,55	0,16	0,43
236,5	0,54	0,27	0,52
240,5	0,60	0,31	0,80
244,5	0,80	0,28	0,84
248,5	1,11	0,28	0,75
252,5	1,12	0,23	0,49
256,5	1,03	0,29	0,44
260,5	0,72	0,35	0,48
264,5	0,73	0,33	0,44
268,5	0,83	0,30	0,43
272,5	0,77	0,38	0,43
276,5	0,73	0,29	0,53
280,5	0,81	0,33	0,49
284,5	0,82	0,31	0,50
288,5	0,82	0,34	0,57
292,5	0,81	0,32	0,59
296,5	0,91	0,00	0,89
300,5	0,91	0,30	0,58
304,5	0,89	0,31	0,56
308,5	0,88	0,69	0,19
312,5	0,87	0,31	0,69
316,5	0,88	0,26	0,69
320,5	1,01	0,35	0,61
324,5	0,95	0,35	0,71
328,5	0,96	0,36	0,62
332,5	1,05	0,35	0,75

Prof. (cm)	%C	%C _{org}	%C _{inorg}
336,5	0,98	0,38	0,71
340,5	1,11	0,23	0,83
344,5	1,09	0,36	0,74
348,5	1,06	0,38	0,74
352,5	1,10	0,35	0,75
356,5	1,11	0,33	0,77
360,5	1,10	0,31	0,75
364,5	1,11	0,33	0,88
368,5	1,06	0,32	0,81
372,5	1,22	0,28	0,96
376,5	1,12	0,28	1,05
380,5	1,23	0,29	1,09
384,5	1,32	0,25	1,48
388,5	1,38	0,27	2,06
392,5	1,73	0,20	1,42
396,5	2,32	0,27	1,31
400,5	1,62	0,23	1,55
404,5	1,58	0,27	1,01
408,5	1,78	0,35	0,84
412,5	1,27	0,26	0,86
416,5	1,19	0,23	0,63
424,5	0,86	0,26	0,63
428,5	0,00	0,27	0,68
432,5	0,89	0,31	0,67
436,5	0,96	0,34	0,59
440,5	0,98	0,25	0,36
444,5	0,93	0,29	0,90
448,5	0,61	0,29	0,82

Prof. (cm)	%C	%C _{org}	%C _{inorg}
452,5	1,19	0,40	0,88
456,5	1,10	0,23	1,04
460,5	1,28	0,24	0,82
464,5	1,27	0,20	0,70
468,5	1,05	0,20	0,82
472,5	0,91	0,26	0,59
476,5	1,03	0,23	0,74
480,5	0,85	0,25	0,77
484,5	0,96	0,33	0,98
488,5	1,02	0,19	2,93
492,5	1,31	0,17	4,05
496,5	3,13	0,12	3,45
500,5	4,22	0,15	4,91
504,5	3,57	0,08	4,31
508,5	5,06	0,22	5,58
512,5	4,38	0,25	5,69
516,5	5,80	0,23	5,41
520,5	5,94	0,12	4,37
524,5	5,63	0,08	4,26
528,5	4,49	0,17	5,18
532,5	4,35	0,22	5,14
536,5	5,35	0,26	5,64
540,5	5,36	0,21	5,15
544,5	5,89	0,27	5,89
548,5	5,36	0,22	4,91
552,5	6,16	0,31	6,24
556,5	5,14	0,40	6,21
560,5	6,55	0,31	6,18

Prof. (cm)	%C	%C _{org}	%C _{inorg}
564,5	6,61	0,36	6,58
568,5	6,49	0,34	7,34
572,5	6,94	0,32	6,55
576,5	7,68	0,21	6,41
580,5	6,87	0,65	5,99
584,5	6,62	0,57	6,35
588,5	6,63	0,33	6,41
592,5	6,92	0,24	0,72
600,5	0,96	0,20	0,29
604,5	0,00	0,24	0,68
608,5	0,50	0,20	0,37
612,5	0,92	0,22	0,17
616,5	0,57	0,23	0,20
620,5	0,39	0,31	0,28
624,5	0,43	0,28	0,19
628,5	0,59	0,31	1,72
632,5	0,48	0,28	0,48
636,5	2,04	0,32	0,65
640,5	0,76	0,25	0,40
644,5	0,97	0,24	0,48
648,5	0,65	0,26	0,37
652,5	0,72	0,22	0,34
656,5	0,63	0,22	0,38
660,5	0,57	0,22	0,39
664,5	0,60	0,20	0,12
668,5	0,62	0,24	0,32
672,5	0,32	0,41	0,13
676,5	0,56	0,43	0,09

Prof. (cm)	%C	%C _{org}	%C _{inorg}
680,5	0,54	0,51	0,09
684,5	0,52	0,41	0,12
688,5	0,60	0,53	0,15
692,5	0,53	0,33	0,28
696,5	0,69	0,36	0,29
700,5	0,62	0,25	2,23
704,5	0,65	0,22	4,27
708,5	2,48	0,17	4,93
712,5	4,49	0,19	4,72
716,5	5,10	0,07	2,90
720,5	4,91	0,09	3,89
724,5	2,97	0,23	4,93
728,5	3,98	0,21	5,71
732,5	5,16	0,23	5,21
736,5	5,92	0,09	4,92
740,5	5,44	0,20	6,25
744,5	5,00	0,00	6,53
748,5	6,45	0,27	5,76
756,5	6,03	0,44	6,33
760,5	6,09	0,30	5,29
764,5	6,77	0,27	0,60
768,5	5,59	0,16	0,60
772,5	0,87	0,15	0,61
780,5	0,75	0,15	0,56
784,5	0,89	0,11	0,13
788,5	0,70	0,09	0,09
792,5	0,24	0,11	0,17
796,5	0,18	0,16	0,14

Prof. (cm)	%C	%C _{org}	%C _{inorg}
800,5	0,29	0,23	0,20
804,5	0,30	0,24	0,20
808,5	0,43	0,25	0,21
812,5	0,44	0,21	0,29
816,5	0,46	0,16	0,34
820,5	0,50	0,15	0,07
824,5	0,50	0,17	0,10
828,5	0,23	0,22	0,15
832,5	0,27	0,29	0,26
836,5	0,37	0,29	0,22
840,5	0,55	0,28	0,26
844,5	0,50	0,31	0,20
848,5	0,53	0,36	0,23
852,5	0,51	0,35	0,11
856,5	0,58	0,34	0,13
860,5	0,46	0,36	0,44
864,5	0,48	0,31	1,42
872,5	0,80	0,00	1,09
876,5	1,73	0,00	0,87
880,5	0,00	0,00	0,73
884,5	1,09	0,00	2,12
888,5	0,87	0,00	0,85
892,5	0,73	0,17	3,11

BIBLIOGRAPHIE

- Aksu, A. E. (1983a), Short-period geomagnetic excursion recorded in Pleistocene sediments of Baffin Bay and Davis Strait., *Geological Society of America*, 11, 537-541.
- Aksu, A. E. (1983b), Holocene and Pleistocene dissolution cycles in deep-sea cores of Baffin Bay and Davis Strait: paleoceanographic implications, *Marine Geology*, 53, 331-348.
- Aksu, A. E., et D. J. W. Piper (1979), Baffin Bay in the past 100,000 yr, *Geology*, 7, 245-248.
- Anderson, R. F., M. P. Bacon, et P. G. Brewer (1983a), Removal of ^{230}Th and ^{231}Pa at ocean margins, *Earth and Planetary Science Letters*, 66, 73-90.
- Anderson, R. F., M. P. Bacon, et P. G. Brewer (1983b), Removal of ^{230}Th and ^{231}Pa from the open ocean, *Earth and Planetary Science Letters*, 62, 7-23.
- Andrews, J. T. (1998), Abrupt changes (Heinrich events) in late Quaternary North Atlantic marine environments: a history and review of data and concepts, *Journal of Quaternary Science*, 13(1), 3-16.
- Andrews, J. T., et K. Tedesco (1992), Detrital carbonate-rich sediments, northwestern Labrador Sea: Implications for ice-sheet dynamics and iceberg rafting (Heinrich) events in the North Atlantic, *Geology*, 20, 1087-1090.
- Andrews, J. T., et B. Maclean (2003), Hudson Strait ice streams: a review of stratigraphy, chronology and links with North Atlantic Heinrich events, *Boreas*, 32, 4-17.
- Azetsu-Scott, K., A. Clarke, K. Falkner, J. Hamilton, P. Jones, C. Lee, B. Petrie, S. Prinsenberg, M. Starr, et P. Yeats (2010), Calcium carbonate saturation states in the waters of the Canadian Arctic Archipelago and the Labrador Sea, *Journal of Geophysical Research*, 115, C11021.
- Barber, D. C., A. Dyke, C. Hillaire-Marcel, A. E. Jennings, J. T. Andrews, M. W. Kerwin, G. Bilodeau, R. McNeely, J. Southon, M. D. Morehead et J.-M. Gagnon (1999), Forcing of the cold event of 8,200 years ago by catastrophic drainage of Laurentide lakes, *Nature* 400, 344-348.

- Begemann, F., K. R. Ludwig, G. W. Lugmair, K. Min, L. E. Nyquist, P. J. Patchett, P. R. Renne, C.-Y. Shih, I. M. Villa, et R. J. Walker (2001), Call for an improved set of decay constants for geochronological use, *Geochimica et Cosmochimica Acta*, 65, 111-121.
- Blinova, M., R. Thorsen, R. Mjelde, et J. I. Faleide (2009), Structure and evolution of the Bellsund Graben between Forlandsundet and Bellsund (Spitsbergen) based on marine seismic data, *Norwegian Journal of Geology*, 89, 215-228.
- Bond, G., et R. Lotti (1995), Iceberg discharges into the North Atlantic on millennial time scales during the Last Glaciation, *Science*, 267, 1005-1010.
- Bond, G., W. Broecker, S. Johnsen, J. McManus, L. Labeyries, J. Jouzel, et G. Bonani (1993), Correlations between climate records from North Atlantic sediments and Greenland ice, *Nature*, 365, 143-147.
- Bourdon, B., S. Turner, G. M. Henderson, et C. C. Lundstrom (2003), Introduction to U-series Geochemistry, in *Uranium-Series Geochemistry*, edited by B. Bourdon, S. Turner, G. M. Henderson et C. C. Lundstrom, pp. 1-21.
- Broecker, W. S. (1987), The biggest chill, *Natural History*, 96, 74-82.
- Broecker, W. S. (1991), The great conveyor belt, *Oceanography*, 4(2), 79-89.
- Broecker, W. S., et G. H. Denton (1989), The role of ocean-atmosphere reorganizations in glacial cycles, *Geochimica et Cosmochimica Acta*, 53, 2465-2501.
- Broecker, W. S., G. Bond, M. Klas, E. Clark, et J. McManus (1992), Origin of the northern Atlantic's Heinrich events, *Climate Dynamics*, 6, 265-273.
- Broecker, W. S., G. H. Denton, R. L. Edwards, H. Cheng, R. B. Alley, et A. E. Putnam (2010), Putting the Younger Dryas cold event into context, *Quaternary Science Reviews*, 29(9-10), 1078-1081.
- Campbell, D. C., et A. de Vernal (2009), Marine geology and paleoceanography of Baffin Bay and adjacent areas. Nain, NL to halifax, NS, August 28-September 23, 2008. Cruise report of CCGS Hudson Expedition 2008029, *Geological Survey of Canada, Open File 5989*, Natural Resources Canada, 2010 pages.
- Causse, C., et C. Hillaire-Marcel (1989), Thorium and uranium isotopes in upper Pleistocene sediments of ODP sites 645 (Baffin Bay), 646, and 647 (Labrador Sea), *Proceedings of the Ocean Drilling Program, Scientific Results*, 105, 551-560.

- Chase, Z., R. F. Anderson, M. Q. Fleisher, et K. P.W. (2002), The influence of particle composition and particle flux on scavenging of Th, Pa and Be in the ocean, *Earth and Planetary Science Letters*, 204, 215-229.
- Chase, Z., R. F. Anderson, M. Q. Fleishera, et P. W. Kubik (2003), Scavenging of ^{230}Th , ^{231}Pa and ^{10}Be in the Southern Ocean (SW Pacific sector): the importance of particle flux, particle composition and advection, *Deep-Sea Research II*, 50, 739–768.
- Cheng, H., R. Lawrence Edwards, M. T. Murrell, et T. M. Benjamin (1998), Uranium-thorium-protactinium dating systematics, *Geochimica et Cosmochimica Acta*, 62(21-22), 3437-3452.
- Cheng, H., R. L. Edwards, J. Hoff, C. D. Gallup, D. A. Richards, et Y. Asmerom (2000), The half-lives of uranium-234 and thorium-230, *Chemical Geology*, 169, 17–33.
- Clarke, G. K. C., A. B. G. Bush, et J. W. M. Bush (2009), Freshwater discharge, sediment transport, and modeled climate impacts of the final drainage of glacial Lake Agassiz, *Journal of Climate*, 22, 2161-2180.
- Cochran, J. K. (1992), The oceanic chemistry of the uranium- and thorium-series nuclides, in *Uranium-series Disequilibrium: Application to Earth, Marine, and Environmental Sciences*, edited by M. Ivanovich et R. S. Harmon, pp. 334-395, Clarendon Press, Oxford.
- Cochran, J. K., et P. Masqué (2003), Short-lived U/Th Series Radionuclides in the Ocean: Tracers for Scavenging Rates, Export Fluxes and Particle Dynamics, *Reviews in Mineralogy and Geochemistry*, 52(1), 461-492.
- de Vernal, A., C. Hillaire-Marcel, A. Aksu, et J. P. Mudie (1987), Palynostratigraphy and chronostratigraphy of Baffin Bay deep sea cores: Climatostratigraphic implications, *Palaeogeography, Palaeoclimatology, Palaeoecology*, 61, 97-105.
- de Vernal, A., G. Bilodeau, C. Hillaire-Marcel, et N. Kassou (1992), Quantitative assessment of carbonate dissolution in marine sediments from foraminifer linings vs. shell ratios: example from Davis Strait, NW North Atlantic, *Geology*, 20, 527–530.
- Dickson, R. R., et J. Brown (1994), The production of North Atlantic Deep Water: Sources, rates, and pathways, *Journal of Geophysical Research*, 99, 12319-12341.
- Dyke, A. S., J. T. Andrews, P. U. Clark, J. H. England, G. H. Miller, J. Shawe, et J. J. Veillette (2002), The Laurentide and Innuitian ice sheets during the Last Glacial Maximum, *Quaternary Science Reviews*, 21, 9-31.

Faure, G., et T. M. Mensing (2005), *Isotopes Principles and Applications*, Third ed., 897 pp., John Wiley & Sons, Inc.

François, R. (2007), Paleoflux and Paleocirculation from Sediment ^{230}Th and $^{231}\text{Pa}/^{230}\text{Th}$, in *Proxies in Late Cenozoic Paleoceanography*, edited by C. Hillaire-Marcel et A. de Vernal, pp. 681-716, Elsevier.

François, R., Bacon M.P., et M. A. Altabet (1993), Glacial/interglacial changes in sediment rain rate in the SW Indian sector of Subantarctic waters as recorded by ^{230}Th , ^{231}Pa , U and $\delta^{15}\text{N}$, *Paleoceanography*, 8, 611-629.

François, R., M. Frank, M. M. Rutgers van der Loeff, et M. P. Bacon (2004), ^{230}Th normalisation: An essential tool for interpreting sedimentary fluxes during the late Quaternary, *Paleogeography*, 19(1).

Gariepy, C., B. Ghaleb, C. Hillaire-Marcel, A. Mucci, et S. Vallières (1994), Early diagenetic processes in Labrador Sea sediments: uranium-isotope geochemistry, *Canadian Journal of Earth Sciences*, 31(1), 28-37.

Heinrich, H. (1988), Origin and consequences of cyclic ice rafting in the northeast Atlantic Ocean during the past 130,000 years, *Quaternary Research*, 29, 142-152.

Hemming, S. R. (2004), Heinrich events: Massive late Pleistocene detritus layers of the North Atlantic and their global climate imprint, *Review of Geophysics*, 42, 1-43.

Hemming, S. R., W. S. Broecker, W. D. Sharp, G. C. Bond, R. H. Gwiazdaa, J. F. McManus, M. klas, et I. Hajdas (1998), Provenance of Heinrich layers in core V28-82, northeastern Atlantic: $^{40}\text{Ar}/^{39}\text{Ar}$ ages of ice-rafterd hornblende, Pb isotopes in feldspar grains, and Nd-Sr-Pb isotopes in the fine sediment fraction, *Earth and Planetary Science Letters*, 164 317-333.

Henderson, G. M., et R. F. Anderson (2003), The U-series Toolbox for Paleoceanography, *Mineralogical Society of America*, 52(1), 493-531.

Hesse, R., et A. Rakofsky (1992), Deep-sea channel/submarine-yazoo system of the Labrador Sea: a new deep-water facies model (1), *Bulletin of the American Association of Petroleum Geologists*, 104, 680-707.

Hesse, R., I. Klaucke, W. B. F. Ryan, et D. J. W. Piper (1997), Ice-sheet sourced juxtaposed turbidite systems in Labrador Sea, *Geoscience Canada*, 24(1), 3-12.

Hillaire-Marcel, C., A. De Vernal, G. Bilodeau, et A. J. Weaver (2001), Absence of deep-water formation in the Labrador Sea during the last interglacial period, *Nature*, 410(6832), 1073-1077.

- Hoffmann, S. S., J. F. McManus, W. B. Curry, et L. S. Brown-Leger (2013), Persistent export of ^{231}Pa from the deep central Arctic Ocean over the past 35,000 years, *Nature*, 497, 603-607.
- Kumar, N., R. Gwiazda, R. F. Anderson, et P. N. Froelich (1993), $^{231}\text{Pa}/^{230}\text{Th}$ ratios in sediments as a proxy for past changes in Southern Ocean Productivity, *Nature*, 362, 45-48.
- Lazier, J., R. Hendry, A. Clarke, I. Yashayaev, et P. Rhines (2002), Convection and restratification in the Labrador Sea, 1990-2000, *Deep-Sea Research I*, 49, 1819-1835.
- Lazier, J. R. N. (1973), The renewal of Labrador Sea Water, *Deep Sea Research*, 20(4), 341-353.
- Lewis, C. F. M., A. A. L. Miller, E. Levac, D. J. W. Piper, et G. V. Sonnichsen (2012), Lake Agassiz outburst age and routing by Labrador Current and the 8.2 cal ka cold event, *Quaternary International*, 260, 83-97.
- Lynch-Stieglitz, J., J.F. Adkins, W" B., Curry, T. Dokken, I.R., Hall, J.C., Herguera, J. J.-M. Hirschi, E.V. Ivanova, C. Kissel, O. Marchal, T.M. Marchitto, I.N. McCave, J.F. McManus, S. Mulitza, U. Ninnemann, F. Peeters, E.-F. Yu et R. Zahn (2007), Atlantic Meridional Overturning Circulation During the Last Glacial Maximum, *Science*, 316, 66-69.
- Marchal, O., R. François, T. F. Stocker, et F. Joos (2000), Ocean thermohaline circulation and sedimentary $^{231}\text{Pa}/^{230}\text{Th}$ ratio, *Paleoceanography*, 15, 625-641.
- Marshall, J., et F. Schott (1999), Open-ocean convection: obercation, theory, and models, *Review of Geophysics*, 37, 1-64.
- McManus, J. F., R. François, J.-M. Gherardi, L. D. Keigwin, et S. Brown-Leger (2004), Collapse and rapid resumption of Atlantic meridional circulation linked to deglacial climate changes, *Nature*, 428, 834-837.
- Not, C., K. Brown, B. Ghaleb, et C. Hillaire-Marcel (2012), Conservative behavior of uranium vs. salinity in Arctic sea ice and brine, *Marine Chemistry*, 130-131, 33-39.
- Simon, Q. (2013), Propriétés magnétiques, minéralogiques et sédimentologiques des sédiments profonds de la baie de Baffin: Chronologie et dynamique des glaciers ouest groenlandais, innuitiens et laurentidiens au cours de la dernière glaciation, 163 pp, Université du Québec à Montréal (QC), Canada.
- Simon, Q., G. St-Onge, et C. Hillaire-Marcel (2012), Late Quaternary chronostratigraphic framework of deep Baffin Bay glaciomarine sediments from

high-resolution paleomagnetic data, *Geochemistry, Geophysics, Geosystems*, 13, 1-24.

Simon, Q., C. Hillaire-Marcel, G. St-Onge., et J. T. Andrews (2014), North-eastern Laurentide, western Greenland and southern Innuitian ice stream dynamics during the last glacial cycle, *Journal of Quaternary Science*, 29, 14-26.

Tang, C. C. L., C. K. Ross, T. Yao, B. Petrie, B. M. DeTracey, et E. Dunlap (2004), The circulation, water masses and sea-ice of Baffin Bay, *Progress in Oceanography*, 63, 183-228.

Veiga-Pires, C. C., et C. Hillaire-Marcel (1999), U and Th isotope constraints on the duration of Heinrich events H0-H4 in the southeastern Labrador Sea, *Paleoceanography*, 14(2), 187-199.

Yu, E. F., R. Francois, et M. P. Bacon (1996), Similar rates of modern and last-glacial ocean thermohaline circulation inferred from radiochemical data, *Nature*, 379, 689-694.

Yu, E. F., R. Francois, M. P. Bacon, et A. P. Fleer (2001), Fluxes of ^{230}Th and ^{231}Pa to the deep sea: implications for the interpretation of excess ^{230}Th and $^{231}\text{Pa}/^{230}\text{Th}$ profiles in sediments, *Earth and Planetary Science Letters*, 191, 219-230.